TV White Space and Broadband Power Line Communications for Indoor High Speed Networks

Thesis submitted in accordance with the requirements of
the University of Liverpool for the degree of Doctor in Philosophy
by

Mohammad Heggo

April 2017

Declaration

The work in this thesis is based on research carried out at the University of Liverpool and the Institute for Infocomm Research (I^2R) at the Agency for Science, Technology and Research (A*STAR) in Singapore. No part of this thesis has been submitted elsewhere for any other degree or qualification and it is all my own work unless referenced to the contrary in the text.

Mohammad Heggo

University of Liverpool

Abstract

Current indoor networks have growing data rate demands to satisfy high speed applications. Broadband power line communications (BPLC) and TV white space (TVWS) communications are considered as effective solutions for indoor networks. However, they encounter several challenges concerning coexistence with wireless services. In this thesis, cooperative BPLC and TVWS is investigated in the very high frequency (VHF) band, for the aim of complementing each other to deliver enhanced performance.

The main contributions of the thesis are multi-folds. In the first contribution, a general statistical based path loss mapping (GSBPL) approach is proposed for modelling the path loss of indoor low voltage (*i.e.* 220 v) BPLC. Also, a simplification method is proposed for computing the channel transfer function, which is proved to be more general and computationally more efficient than the previous method in literature. The feasibility of the cooperation between BPLC and wireless communications is thus concluded, through comparing their corresponding path losses.

In the second contribution, a general model is proposed to map the TVWS interference with the BPLC in the VHF band, through exciting antenna mode currents along low voltage BPLC cables. A new model is presented for current

conversion from antenna to differential mode, which includes a general formula for the antenna mode characteristic impedance and two solutions to the formulated problem: a) a numerical solution referred to as the antenna theory numerical (ATN) approach; b) an analytical solution referred to as the enhanced TL approximation (ETLA) approach. This is the first reported work to obtain the antenna mode characteristic impedance by the antenna theory. The ETLA approach outperforms the previous frequency-independent solution and requires a reduced complexity over the ATN approach.

In the third contribution, new hybrid systems utilising BPLC and TVWS are proposed in the VHF band referred to as white BPLC (WBPLC). Two cases are considered in the proposed system: a) point-to-point WBPLC multiple-input multiple-output (MIMO) system, where a power allocation algorithm and an iterative precoding technique are proposed to maximise the ergodic capacity, subject to the constraints of total power and interference limit at the TV primary user (PU) receiver (Rx); b) point-to-multipoint WBPLC MIMO system. The overall network downlink capacity maximisation problem is investigated, using an efficient algorithm for power and subcarrier allocation among different users.

Acknowledgements

It is a great pleasure to thank everyone who helped me write my dissertation successfully. I am sincerely and heartily grateful to my enthusiastic supervisor Dr. Xu Zhu. Not only did she support me with her tremendous academic experience, but also she encouraged me and provided me with a lot of facilities to present a creative idea. Actually, Dr. Zhu continued her support to me and followed up my progress even when she was sick. I believe that without her continuous support, this work would not have come to light. Also, I would like to show my gratitude to Prof. Yi Huang, who guided me on utilising the lab equipment during my research and supported me with his invaluable research experience.

Similar, profound gratitude goes to Dr. Sumei Sun at Institute for Infocomm Research (I^2R) at the Agency for Science, Technology and Research (A*STAR), Singapore for the continuous support and guidance for two years of my attachment in Singapore. Dr. Sun's support helped me to benefit from the new research environment in Singapore.

Sincere and earnest thankful to my colleagues in the Wireless Communication and Smart Grid group in Liverpool: Mr. Kainan Zhu, Mr. Jun Yin, Dr. Linhao Dong, Mr. Zhongxiang Wei, Mr. Teng Ma, Mr. Yanghao Wang and Dr. Chao Zhang for continuous support and wonderful team work. Also, similar mentions

to my colleagues in A*STAR in Singapore: Dr. Zhang, Peng, Dr. Johann Leithon, Mr. David Martin and Miss Doris Benda for creating such productive and progressive research environment.

Completing this work would have been more difficult were it not for the support and friendship provided by the other members of the Electrical Engineering and Electronics Department in Liverpool, and I^2R in Singapore. I am indebted to them for their help.

Last, but by no means the least, thanks to my parents, my brother and his little family who always believe in me. They are the most important people in my life and this work is the result of their encouragement and support.

Dedications

This piece of work is dedicated to moon of north Africa. To my country Egypt, from the far Islands of Tiran and Sanafir to every city within the land of peace, and to the martyrs, who defended justice, peace and unity of its people and land.

Contents

List of Figures

List of Tables

Abbreviations and Acronyms

AGC automatic gain control

APGF antenna potential Green's function

ATN antenna theory numerical

AWGN additive white Gaussian noise

BCU basic channel unit

BPLC broadband power line communication

CCDF complementary cumulative distribution function

CDGF charge density Green's function

CENELEC comité European de normalisation électrotechnique

CIFS contention interframe space

CISPR comité international spécial des perturbations radioélectriques

CSI channel state information

CSMA carrier sense multiple access

DTMC discrete time Markov chain model

ECMA European computer manufacturers association

EFIE electric field integral equation

EIRP effective isotropic radiated power

EMC electromagnetic compatibility

EMI electromagnetic interference

ETLA enhanced transmission line approximation

FAF floor attenuation factor

FC frame control

FCC Federal Communication Commission

FM frequency modulation

FWTL full wave transmission line

GI guard interval

GRB gain roll back

GSBPLM general statistics based path loss mapping

GUPL general urban path loss model

HF high frequency

HT-WBPLC high throughput WBPLC

IEEE Institute of Electrical and Electronics Engineers

KKT Karush-Kuhn-Tucker

LR-WPAN low rate wireless personal area network

MAC medium access control

MIMO multiple-input multiple-output

MISO multiple-input single-output

ML maximum likelihood

MOM method of moments

MVGF magnetic vector potential Green's function

NA network analyser

NMSE normalised mean square error

Non HT Non-high throughput

OBS obstructed

OFDM orthogonal division multiplexing

P-SVD projected singular value decomposition

PHY physical

PLC power line communication

PSD power spectral density

PU primary user

p.u.l. per unit length

QAM quadrature amplitude modulation

RF radio frequency

RIFS response interframe space

rms root mean square

Rx receiver

SACK selective acknowledge

SE spectral efficiency

SG signal generator

SISO single-input single-output

SM spatial multiplexing

SNR Signal to Noise Ratio

STBC space time block coding

SU secondary user

SVD singular value decomposition

TEM transverse electromagnetic field

TL transmission line

TVBD TV band device

TVHT TV very high throughput

TVWS TV white space

Tx transmitter

UHF ultra-high frequency

VHF very high frequency

VHT very high throughput

WBPLC white BPLC

WLAN wireless local area network

WRAN wireless regional area network

WSAN wireless sensor and actuator network

Chapter 1

Introduction

1.1 Background and Motivation

In smart grid, wireless sensor and actuator networks (WSANs) are used to monitor and control the energy consumption of home users. In WSANs, cameras and acoustic sensors are connected to improve the reliability and efficiency of the smart grid systems, which increases the demand for multimedia smart grid communication infrastructure [1]. In order to fulfill the high data rate services in future smart grid networks, the demand for radio spectrum grows rapidly. On the other hand, vast measurement data have shown that the scarcity problem in the radio spectrum is mainly caused by inefficient spectrum utilisation. For example, the results of spectrum occupancy measurements in [2–6], which were held in different countries show that the radio spectrum occupancy level does not exceed 25%. This yields more attention towards cognitive radio solution in high speed applications such as TV video streaming [7], which allows the unlicensed users to access licensed spectrum without causing harmful interference to the incumbent

licensed users.

In May 2004, the federal communications commission (FCC) recommended the cognitive access of the temporally or geographically underutilised channels in the television (TV) spectrum known as TV white space (TVWS) [8]. In November 2008, the FCC released the regulatory rules which allow the unlicensed users (known as secondary users (SUs)) to utilise the very high frequency (VHF) band (30 MHz - 300 MHz) and the ultra-high frequency (UHF) band (300 MHz - 3 GHz) in the TVWS [9]. The regulations guarantee maximum protection for the primary users (PUs), which can be translated to more spectrum access restrictions on the TV band devices (TVBDs). The TVBDs should acquire a detailed map for the free TVWS spectrum within a certain geographic area and time slot through geolocation database access and/or spectrum sensing techniques. Following the FCC regulation, other international organisations such as the Institute of Electrical and Electronics Engineers (IEEE) [10] and the European Computer Manufacturers Association (ECMA) [11] began the journey to define the physical (PHY) and the medium access control (MAC) layers standards for the TVWS communications.

Another technology that spans the VHF band is broadband power line communication (BPLC) [12]. The BPLC technology relies mainly on transmitting the data over the existing low voltage (*i.e.* 220 V) power line cables, hence offers a cost-effective solution. However, low voltage power line cables are not designed for high speed communications. The broadband signal therefore suffers radiation especially in the VHF band. This can yield an electromagnetic interference (EMI) with the existing wireless services [13–15]. To prevent from severe EMI, the transmission power spectral density (PSD) of the BPLC in the frequency band below 30

MHz is restricted to -55 dBm/Hz, and above 30 MHz to -85 dBm/Hz, respectively according to both the IEEE 1901 [16] and the HomeplugAV2 [17] standards. The strict restriction over the PSD of the BPLC in the VHF band limits the maximum achievable throughput in that band. In other words, the achievable throughput in the permissible VHF band in BPLC (30 MHz 100 MHz) is limited compared to the HF band (2 MHz 30 MHz), which implies bandwidth efficiency loss. This represents a crucial problem in BPLC, which requires an innovative solution for better exploitation of the BPLC VHF band.

1.2 Thesis Contributions

The research conducted during this PhD study is aimed to investigate the cooperation between BPLC and TVWS in the VHF band. Both the TVWS and the BPLC channels are studied in the indoor environment in the VHF band. Hence, a novel statistical approach is proposed for mapping the path loss of the BPLC against distance in the VHF band. Also, a general model is proposed for representing the interference between TVWS and BPLC channels. A new hybrid point to multi-point TVWS BPLC system, referred to as white BPLC (WBPLC) is proposed. The WBPLC exploits the VHF band in the indoor environment by offering a multiple-input multiple-output (MIMO) solution using both the TVWS wireless channel and the BPLC channel.

The main contributions can be summarised as follows.

- A general statistics based path loss mapping (GSBPLM) approach for BPLC is proposed. The work is different in the following aspects. First, to the best

of our knowledge, this is the first work to map the path loss and the coverage distance of each class of the PLC channels using a statistical approach. A new methodology has been followed in mapping and measuring the power line signal coverage distance. The new methodology depends upon introducing the electric coverage distance concept rather than the geometric one which was previously used. Second, novel comparison is provided between the general BPLC path loss mapping and the wireless path loss model in the indoor environment, which can be considered as a preliminary feasibility study of the BPLC and TVWS indoor cooperation.

- A general model is proposed to map the wireless signal interference with the BPLC signal in the VHF band. The general model is constructed for the VHF current conversion from antenna to differential mode across transmission line terminals of the low voltage BPLC cables. The antenna mode currents, also known as common mode currents, are defined for two- or multiconductor transmission line as the currents flowing in the same direction, which implies that the sum of the currents in the multiconductor transmission line is not equal to zero. The antenna mode currents are excited by the electromagnetic interference of the wireless signals. The proposed model includes the derivation of a general formula for the characteristic impedance of the antenna mode current. Two approaches are proposed to the formulated problem: 1) Antenna theory numerical (ATN) approach; 2) Enhanced transmission line approximation (ETLA) analytical approach. The model is important in predicting the amount of antenna mode power transmitted

or reflected at the terminals of the transmission line (TL) and hence, the amount of antenna mode interference to the differential mode signals.

- A new cooperative system between the BPLC and the TVWS named as WBPLC is proposed. WBPLC can get the benefit of TVWS and BPLC without adding up- or down-converters components since both technologies can access the VHF band. Hence, the WBPLC has twofold benefits for TVWS and BPLC communication systems, which can be summarised as follows. 1) WBPLC supports the TVWS with MIMO capability in the VHF band, which improves significantly the achievable throughput, and overcomes the footprint design challenges, 2) WBPLC supports the SU in the TVWS channels with a backup free channel in the high frequency (HF) band (1.8 MHz - 30 MHz). This facility can be utilised in the streaming services, where the delay time of transmission is limited, 3) WBPLC supports the BPLC communication in the VHF band with higher PSD under the umbrella of the FCC regulations. Hence, the power is efficiently distributed between the HF and VHF band, which yields a higher capacity. It is worth mentioning that, to the best of our knowledge, this is the first work to propose a cognitive BPLC solution that complies with the TVWS standard. The addition of wireless antenna to cognitive BPLC is essential to enable the TVWS BPLC transmitter (Tx) to sense the TV primary user (PU) at very low power level of -114 dBm, which satisfies the requirement of the TVWS standard [9], 4) WBPLC supports the BPLC with higher input power due to the increase in the PSD of the VHF band. Hence, using this power, the coverage area and

the number of accommodated users can increase. It is worth mentioning that the maximum allowed input power for the BPLC is 282 mW, which is mostly concentrated in the HF band. Hence, using higher power (which is feasible in the WBPLC) can significantly improve the coverage area for point to multi-point communications in indoor networks, 5) Compared to the hybrid BPLC WiFi system [18], the proposed system does not require up- or down-converters, since BPLC and TVWS share the VHF band. However, the BPLC WiFi has an advantage of utilising complete free band that does not require the government license.

1.3 Thesis Organisation

The rest of this thesis is organised as follows. In Chapter 2, an overview of the TVWS and BPLC standards, channel characteristics and challenges is presented. In Chapter 3, the GSBPLM approach is presented for mapping the BPLC channel path loss. A comparison is presented between the path loss of the BPLC and TVWS channels in the VHF band indoors. Also, the crosstalk between TVWS and BPLC is presented based on the measurement results. In Chapter 4, a general model is presented to represent the interference of the wireless VHF signal to the BPLC signal. The model includes both analytical and numerical approaches to represent the interference. In Chapter 5, the ergodic capacity is investigated for a hybrid TVWS BPLC point-to-point system. In Chapter 6, WBPLC point-to-multipoint system is proposed, where the MAC and the PHY layers are developed

for the new system in order to be TVWS standard compliant. Conclusions and Future work are presented in the final Chapter.

1.4 Publications

Journal Papers

1. M. Heggo, X. Zhu, Y. Huang, and S. Sun, Modeling of VHF Current Conversion from Excited Antenna Mode to Differential Mode at Transmission Line Terminals, *IEEE Transactions on Electromagnetic Compatibility*, vol. 58, no. 4, pp. 1184-1193, August 2016.

2. M. Heggo, X. Zhu, S. Sun, and Y. Huang, "White Broadband Power Line Communication: Exploiting the TVWS for Indoor Multimedia Smart Grid Applications," *submitted to International Journal of Communication Systems.* (under the second round of review)

3. M. Heggo, X. Zhu, S. Sun, and Y. Huang, "TV White Space assisted Broadband Power Line Communication for Indoor MIMO Systems," *submitted to IEEE Transactions on Communications.*

4. M. Heggo, X. Zhu, S. Sun, and Y. Huang, "Point-to-Multi-Point Hybrid TV White Space-Power Line Communication for Indoor Broadband Networks," *submitted to IEEE Transactions on Wireless Communications.*

Conference Papers

1. M. Heggo, X. Zhu, S. Sun and Y. Huang, "A Hybrid Power Line and TV White Space MIMO System for Indoor Broadband Communications," *in Proc. IEEE 84th Vehicular Technology Conference (VTC)*, September 2016, Montreal Canada.

2. M. Heggo, X. Zhu, Y. Huang, and S. Sun, "TVWS Power Line Communication System for Indoor Networks," *in Proc. 12th IEEE Asia Pacific Wireless Communications Symposium (IEEE VTS APWCS 2015)*, August 2015, Singapore.

3. M. Heggo, X. Zhu, Y. Huang, and S. Sun, "Study of High Frequency Conversion from Excited Antenna Mode to Differential Mode Current at the Transmission Line Terminals," *in Proc. 12th IEEE Asia Pacific Wireless Communications Symposium (IEEE VTS APWCS 2015)*, August 2015, Singapore.

4. M. Heggo, X. Zhu, Y. Huang, and S. Sumei, "A Novel Statistical Approach of Path Loss Mapping for Indoor Broadband Power Line Communications," *in Proc. IEEE International Conference on Smart Grid Communication*, November 2014, Venice, Italy.

Chapter 2

Overview of TVWS and BPLC

2.1 Introduction

In this Chapter, an overview of the main regulations and standards of both TVWS and BPLC technologies is presented. Also, the channel characteristics of the wireless TVWS and the BPLC in the VHF band are shown, along with the crosstalk between the two channels. The aim of the presentation is to highlight the advantages and the limitations of each technology, and at the same time highlight the fact that the advantages of one technology may be used to overcome the limitations in the other one. Also, previous work in enhancing the capacity of the BPLC channel in the VHF band is presented. Consequently, this drives the motivation to discuss the expected advantages of the cooperation between the TVWS and the BPLC communications in the indoor environment, which exploits the VHF band in TVWS by offering an MIMO solution using both the TVWS wireless channel and the BPLC channel.

2.2 TVWS Regulations and Standards

2.2.1 Governing Regulations

According to the FCC rules issued in 2008 [9], TVBDs are divided into two categories: 1) fixed devices, and 2) portable/personal devices. For the fixed devices, they are allowed to access a free TV channel with total transmission power of 4 W as effective isotropic radiated power (EIRP). However, for the portable/personal devices, the maximum permissible EIRP is 100 mW and 40 mW for a free non-adjacent and adjacent channel next to an occupied TV channel, respectively. The fixed devices category should have an access over a geolocation database to obtain a list of the free channels and also should have a high sensing capability to detect PU presence even if the PU received signal power is as low as -114 dBm. However, the portable/personal devices category is further subdivided into two subcategories: 1) mode I, which should have an access over a geolocation database, and 2) mode II, which is unnecessary to have a connection with a geolocation database but must have a high sensing capability.

2.2.2 Standards

The TVWS standards are developed mainly by two organisations: IEEE [10] and ECMA [11]. IEEE developed five standards to utilise the TVWS spectrum in different applications, which can be summarised as: 1) IEEE 802.11af for wireless local area network (WLAN), 2) IEEE 802.22 for wireless regional area network (WRAN), 3) IEEE 802.15.4m for low rate wireless personal area network (LR-WPAN), 4) IEEE 802.19.1 for enabling the family of IEEE 802 wireless standards

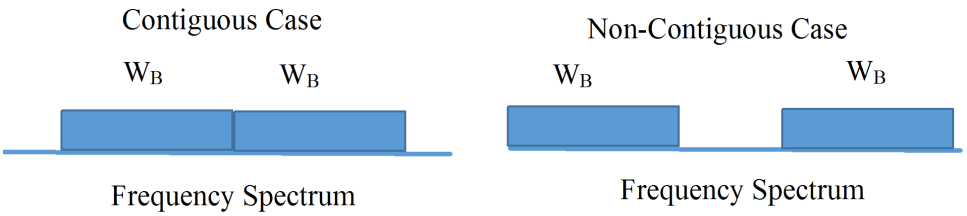

FIGURE 2.1: Contiguous and Non-Contiguous TV channels in IEEE 802.11af.

to effectively utilise the TVWS spectrum by providing coexistence methods among independent TVBD networks, 5) IEEE 1900.7 for radio interface working in the TVWS spectrum. ECMA also released the standard ECMA-392 first edition in 2009 and second edition in 2012 for supporting TVWS access. In this Chapter, the WLAN applications are the main interesting topic; hence the IEEE 802.11af and ECMA-392 standards will be discussed in details.

IEEE 802.11af

In December 2013, IEEE 802.11af standard was released to provide the PHY and MAC regulations to organise spectrum sharing among licensed and unlicensed users in the TVWS. The IEEE 802.11af is considered as an amended version of the main standard IEEE 802.11 and its very high throughput (VHT) version of IEEE 802.11ac operating in bands below 6 GHz band. In IEEE 802.11af, two modes are presented: 1) Non-high throughput (Non HT); 2) TV very high throughput (TVHT). The channel bandwidth for non-HT mode is the basic channel unit (BCU) W_B. The BCU is defined as the original bandwidth of the TV channel according to the regulatory domain i.e. 6 MHz, 7 MHz and 8 MHz. However, the TVHT support two modes for the channel bandwidth: 1) Contiguous mode (i.e. $2W_B$, $4W_B$), where the channel bandwidth spans two or more adjacent BCUs. 2)

Non-contiguous mode (W_B+W_B, $2W_B$+$2W_B$, where the channel bandwidth spans two or more non-adjacent BCUs. Also, the TVHT supports two or more spatial streams, which enhances significantly the achieved throughput. For each orthogonal division multiplexed (OFDM) symbol, 144 subcarriers are used in 6 MHz or 8 MHz channel. However, for 7 MHz, 168 subcarriers are used to maintain the same sub-channel bandwidth of the 6 MHz channel. This yields a subcarrier frequency spacing of 41.66 kHz for the 6 and 7 MHz channels, while for the 8 MHz channel, the subcarrier frequency spacing is 55.55 kHz. The duration of the OFDM symbol is 24 μs for the 6 and 7 MHz channels, while it is 18 μs for 8 MHz channel. Also the guard interval (GI) period is defined as quarter of the OFDM symbol duration.

The general frame format for the PHY protocol data unit (PPDU) consists of 8 fields: non-TVHT short training field (L-STF = 8 μs), non-TVHT long training field (L-LTF = 8 μs), non-TVHT signal field (L-SIG = 4 μs), TVHT signal A field (TVHT-SIG-A = 4 μs), TVHT short training field (TVHT-STF = 8 μs), TVHT long training field (TVHT-LTF = 8 μs), TVHT signal B field (TVHT-SIG-B = 4 μs) and data field. The TVHT fields of the general frame exist only in the TVHT mode. The non-TVHT STF is used to improve the automatic gain control (AGC) of the single-input single output (SISO) channel, diversity selection, time acquisition and coarse frequency estimation at the Rx side. Also, the non-TVHT LTF is used for the channel estimation and frequency acquisition at the receiver (Rx). However, TVHT-STF and TVHT-LTF aim to improve the AGC and channel estimation for the MIMO Rx. The non-TVHT signal field contains the frame header, which holds information about the frame length, rate, parity bits and tail bits. The TVHT-SIG-A field contains information related to interpreting the TVHT

frame such as: channel bandwidth, space time block coding (STBC) and beamforming. The TVHT-SIG-B field contains information about the padding and tail bits in the TVHT frame.

ECMA-392

In December 2009, ECMA released its first edition of the ECMA-392 standard to provide the PHY and MAC layers for the TVWS communications. The ECMA-392 standard [11] adopts a channel bandwidth equivalent to the BCU bandwidth (*i.e.* 6 MHz, 7 MHz and 8 MHz). Unlike the IEEE 802.11af, the ECMA 392 standard does not support the contiguous or the non-contiguous modes of operation, which means that the channel bandwidth is limited only to one BCU channel. Also, the standard supports using multiple spatial data streams like the TVHT in the IEEE 802.11af. Each TV channel is spanned by 128 subcarriers, with subcarrier frequency spacing of 53.5 kHz, 62.5 kHz and 71.42 kHz for channel bandwidths of 6 MHz, 7 MHz and 8 MHz, respectively. The OFDM symbol duration is taken as 18.667 μs, 16 μs and 13.8 μs for the previously mentioned channel bandwidths. The GI period can be taken as the symbol time duration divided by 8, 16 or 32.

The PHY frame in ECMA-392 is divided into three main fields: 1) preamble, 2) header, and 3) data. The preamble field consists of two sub-fields: a) short preamble, which has the duration of one OFDM symbol, and is used for automatic gain control (AGC) at the receiver (Rx) side, b) long preamble, which has the duration of two OFDM symbols and is used for channel estimation. The header field consists of PHY header, MAC header, parity bits and tail bits. The PHY header holds the information of data rate, length, scrambler initialisation seed, interleaver

option, multiple antenna mode, and transmission power. The MAC header incorporates the information directly from the MAC layer without change. The overall duration of the header is 2 OFDM symbols. The data field consists of the data bytes requested to be sent (maximum 4095 bytes), the tail bits and padding bits.

2.2.3 MIMO TVWS

MIMO techniques can significantly enhance the spectral efficiency of wireless communication systems in communication channels, which are characterised by multi-path propagation due to scattering on different obstacles. Different MIMO techniques, e.g., space time block coding (STBC), spatial multiplexing (SM) are allowed in both IEEE 802.11af [10] and ECMA-392 [11]. However, in [19] and [20] two main challenges were presented to using multiple antennas in the TVWS. The first one is due to the long wavelengths in the UHF and VHF bands. The typical wavelength in UHF ranges from 0.1 m to 1 m, which makes it not practical to design small footprints for MIMO TVBDs. In the VHF, the case is even worse as the wavelength ranges from 1 m to 10 m. The second challenge is the mutual coupling between multiple antennas which increases in the low frequencies. Hence, most of the MIMO solutions were proposed in the UHF band as in [21], which limits the exploitation of the VHF band of the TVWS.

2.2.4 TVWS Channel and its Path Loss

The TVWS channel differs according to the frequency band of operation. However, the VHF channel characteristics are better than the UHF in terms of path loss and penetration through the concrete walls. More focus will be on the VHF

TVWS channel, since it is the shared channel between TVWS and BPLC. According to [22], the path loss of the TVWS is dependent on several factors such as: number of walls, number of floors between the Tx and the Rx, in addition to the frequency and separation distance. For example, the average path loss at 100 MHz ranges between 51 dB and 81 dB for a coverage distance between 15 m and 50 m, respectively. Also, the root mean square (rms) delay of the TVWS channel is 100 ns, which resembles to 90% coherence bandwidth of 200 kHz [23].

The TVWS channel operating in the VHF band in the indoor environment is modeled in [24] using the general urban path loss model (GUPL). The path loss as a function of the coverage distance can be expressed as [24]:

$$\begin{aligned} GUPL(dB) = &- 10\log_{10}([\frac{\lambda}{4\pi d_0}]^{\beta}) \\ &+ 10n\log_{10}(\frac{d}{d_0}) + \alpha d + FAF \end{aligned} \tag{2.1}$$

where d is the Tx-Rx geometrical separation, d_0 is the close-in reference distance and it must be chosen to lie in the far field region, which is defined as the region where the radiation pattern does not change shape with distance (although the fields still die off as $1/d$, the power density dies off as $1/d^2$). Also, this region is dominated by radiated fields, with the E- and H-fields orthogonal to each other and the direction of propagation as with plane waves (*i.e.* $d_0 >> \frac{2D^2}{\lambda}$). λ is the wavelength, D is the maximum linear dimension of the antenna, β is the power exponent, n is the path loss exponent, α is the attenuation constant (dB/m), and FAF is the floor attenuation factor.

2.3 BPLC Regulations and Standards

2.3.1 Governing EMC Regulations

The EMC of the BPLC with the existing wireless devices is a crucial problem for the BPLC and gives rise to EMC broadband regulations [17]. The EMC regulations differ according to each country. For example, in Europe, the standard of comité European de normalisation électrotechnique (CENELEC) organises the emission measurement of each power line device. In addition, the CENELEC standard limits the PSD of the frequency spectrum below 30 MHz to -55 dBm/Hz and -85 dBm/Hz for the frequency band above 30 MHz. In US, the limits of the emission for a given frequency is determined by the maximum radiated electric field which is measured at specific separation distance from the power line cable. In Japan, the standard of comité international spécial des perturbations radioélectriques (CISPR) referred to as CISPR22 limits the PSD for the band below 15 MHz to -71 dBm/Hz and -81 dBm/Hz for the band above 15 MHz.

2.3.2 Standards

IEEE 1901

In 2010, IEEE 1901 standard was released to organise the high speed communication over the electric power lines. The standard spans the frequency band 1.8 MHz - 50 MHz with 1974 subcarriers, where the subcarrier frequency spacing is 24.414 kHz. The OFDM symbol duration is taken as 40.96 μs with guard interval duration of 4.96 μs. The standard supports multiple spatial streams for both

single and three phase power line cables.

HomeplugAV2

As mentioned in [17], the HomePlug Alliance, an industry-led organisation, was formed in 2000 with the scope of promoting power line networking through the adoption of HomePlug specifications. In 2001, the HomePlug Alliance released the HomePlug 1.0.1 specification and followed up in 2005 with a second release: HomePlug AV. (The letters AV stand for audio, video.) Following its release, HomePlug AV rapidly became the most widespread adopted solution for in-home PLC. In December 2011, the Homeplug alliance issued the HomeplugAV2 standard [17] to provide the PHY and MAC layer for high speed power line communications. HomeplugAV2 introduces two main enhancements compared to the IEEE 1901 standard [16]: 1) frequency band extension up to 86 MHz, and 2) MIMO capabilities with beamforming. This yields enhancing the achievable throughput in the HomeplugAV2 standard compared to the IEEE 1901 standard. The OFDM symbol uses 4096 subcarriers in the band 1.8 MHz - 100 MHz, where only 3455 subcarriers are supported for communication in the band 1.8 MHz - 86 MHz with subcarrier frequency spacing of 24.414 kHz. The OFDM symbol duration is 40.96 μs with GI duration of 4.96 μs. The HomeplugAV2 standard uses the same frame structure of IEEE 1901, which supports the carrier sense multiple access (CSMA) protocol. Each frame consists of four main fields: 1) preamble, 2) frame control (FC), 3) data or payload, 4) selective acknowledge (SACK). The preamble field is responsible for packet synchronisation functionality. The FC provides addressing and frame information. The FC and the preamble fields are called collectively the

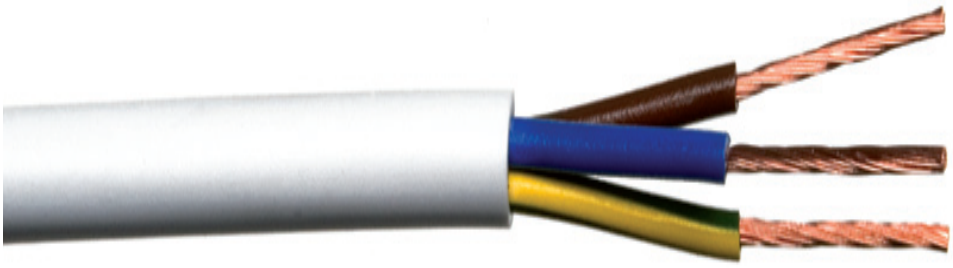

FIGURE 2.2: Typical model of 318-Y indoor low voltage power line cable.

delimiter, which has the duration of 55.5 μs. For the data field, the maximum number of data bytes is 4095 bytes. The data field is followed by a gap period of time according to the CSMA protocol called the response interframe space (RIFS), where the maximum duration of the data field and the RIFS is 2501.12 μs. The SACK field is sent by the Rx to the Tx to request the re-transmission of selected corrupted frames. The duration of the SACK is the same as the delimiter. The SACK field is followed by a gap period of time called the contention interframe space (CIFS). The CIFS and the RIFS periods are taken as 5 μs.

2.3.3 BPLC Channel and its Path Loss Mapping

In Fig. 2.2 a typical three conductors low voltage power line cable is shown. The typical voltage range of the cable is 220 V to 500 V. Also, the conductor is made up of the copper, while the insulator and the sheath are made up of Polyvinyl Chloride material. The cross-section diameter ranges between 0.75 mm^2 and 2.5 mm^2. The low voltage power line cables are not designed to carry the communication signal. Also, A typical power line channel in the UK low-voltage network is characterised as a star-shaped bus structure, exhibiting strong branching,

which considerably impairs the signal quality with a great number of reflection points. Due to such a network structure, a complex echo scenario arises, leading to a frequency-selective fading, represented as notches in the magnitude of the frequency response [25–29]. The frequency- selective behavior of the power line channel is measured by calculating the frequency correlation function, which computes the autocorrelation function for a wide sense stationary uncorrelated scattering channel. The coherence bandwidth is defined as the range of frequencies over which any two frequency components are highly correlated and the frequency correlation factor can be considered flat. According to [27], the 90% coherence bandwidth of the BPLC ranges between 65.5 kHz and 691.5 kHz. On the other side, in order to evaluate the multipath effect of the BPLC channel, the rms delay spread should be calculated. The rms delay can give an indication of the nature of the inter-symbol interference. According to [27], the average rms delay can be taken as 413 ns.

Several approaches have been used to map the path loss and the coverage distance of the PLC signal. They can be categorised into two types: a) the top-down approach [30, 31], where the PLC channel is considered as a black box and the path loss is described using exhaustive channel measurements in the real environment; b) the bottom-up approach [25, 32], where the path loss is deduced by exploiting the transmission line theory to describe the PLC channel under the transverse electromagnetic field (TEM) or quasi-TEM assumption. The bottom-up approaches require a complete knowledge of the power line topology and the terminal loads a priori to the path loss representation and the results need to be further verified using the lab measurements on power line test beds.

The main drawback of the above approaches is the obvious variations of their output path loss curves due to changing the measurement environment or test bed. In [30], the deduced path loss using the top-down approach is 37 dB at 10 MHz for a separation of 100 m point-to-point between the Tx and the Rx. While the path loss obtained in [25] is 57 dB at the same frequency for the same distance using the bottom-up approach and lab measurements.

Another disadvantage of the previous measurement setups is their inability to simulate all the real power line network variations. In [32], a path loss was mapped using a measurement test bed in which the authors tried to vary its parameters to simulate the PLC variations by using different types of loads and doing measurements at different voltages. However, there are still some neglected parameters like the variation of the branches number or the cable types which have a high influence on the path loss of the power line channel.

Two common drawbacks can be observed in the aforementioned path loss representations. First, they do not cover the whole BPLC band of 2-100 MHz. In [30] and [25], the frequency range investigated is up to 20 MHz and 50 MHz, respectively. In [31], the fitting path loss curve is the same for the whole frequency band, neglecting the effect of the frequency variation on the path loss and the coverage distance. Second, the path loss mapping curves obtained in the above work are not deduced for the indoor coverage distance range. In [30], the coverage distance presented exceeds 100 m, and in [25], the coverage distance is beyond 60 m. Hence, a general path loss mapping methodology is required to represent the path loss for different power line topologies.

2.4 TVWS communications interference to BPLC

For the cross talk between the two channels in the VHF band, the near field coupling between broadband power line and high frequency communication systems has been addressed in [33]. It depends on several factors like the cable properties, the coupling circuit and the network asymmetric loads. Also, it has been proposed in [12] to extend the BPLC bandwidth to cover the whole VHF band of 30-300 MHz. However, BPLC in the VHF band suffers interference from surrounding wireless services such as TV and radio channels [14][13]. The current induced by incident electric field has been investigated thoroughly in many EMC applications [34–49].

From the measurement perspective, several measurements based studies in [50–54] suggested enhancing the reception of the BPLC signal by adding an antenna to the receiver and hence, can compromise the radiated electric field. In other words, the authors in [50–54] suggested the addition of wireless antenna at the BPLC Rx, which can receive the radiated electric field during the BPLC transmission, then adding the received wireless signal to the received BPLC signal, the signal to noise ratio of the received BPLC signal could be enhanced.

From the theoretical perspective, the electromagnetic field can interfere with the VHF BPLC by exciting the antenna mode current [45], also known as the common mode current [43]. In this case, the excited current has the same magnitude and phase which implies that the sum of the TL currents is not equal to zero [45]. The excited antenna mode current can convert to differential one by mode conversion mechanisms [55]. Those mechanisms depend mainly on the imbalance

between TLs, which means that the impedance seen by each TL terminal to the ground is not the same [55]. This mode conversion is a significant source of interference to all the differential mode communication signals such as VHF BPLC. In order to evaluate the power converted from the antenna mode to the differential mode at the TL terminals, the amount of the antenna mode power reflected or transmitted at the terminals have to be evaluated, due to the mismatch between the terminal impedance and the antenna mode characteristic impedance. This yields the importance of studying the antenna mode characteristic impedance.

The main approach to describe the antenna mode and the differential mode characteristic impedance is the TL theory, which assumes the existence of three conditions: 1) The cross section area of the wire is very small compared to the wavelength of the incident electric field; 2) The propagating field along the wire is either TEM or quasi-TEM; c) The sum of the currents propagating along the wire must be equal to zero. If any of those conditions is violated, then the TL theory approach becomes inadequate for modeling the characteristic impedance. In [44–49], an approximate TL theory solution was adopted to model the characteristic impedance of transmission lines.

When the first condition above is violated, several studies such as [46] and [47] have considered the dependence of the per unit length (p.u.l.) parameters on frequency. However, those studies did not consider the effect of TL length, which makes the solutions presented in [46] and [47] inadequate for the case of thin wire TLs excited by VHF electric field, *e.g.*, the case of electromagnetic interference which is induced across overhead lines or indoor power line cables. Also, the studies presented in [46] and [47] focused only on the differential mode excitation and

neglected the antenna mode excitation which is the main source of interference. In [48], an iterative method was proposed to solve the classical TL differential equations based on the perturbation theory. It was proved to have higher accuracy than the classical TL method in [49]. However, the iterative method could diverge at some frequencies. In [45], the authors provided a TL approximated solution for antenna mode characteristic impedance. However, they did not take into consideration the effect of the frequency of operation or the angle of incidence of the electric field. In [56], a full wave transmission line (FWTL) solution was proposed based on Maxwell's theory. The transmission line parameters were expressed using a parameter matrix. Iteration and perturbation methods were used to derive the exact solution for the differential mode current case. The parameter matrix of the transmission line is updated for every iteration, which increases the complexity of the solution when being applied to the antenna mode current case, since the integration formula of the parameter matrix gets more complicated for each iteration.

2.5 Enhancing the BPLC Capacity

Enhancing the BPLC capacity and satisfying the interference limit with wireless devices had been approached in the previous literature using three methods: 1) MIMO BPLC as in [17] and [57], 2) cognitive BPLC as in [58–62], and 3) hybrid wireless BPLC as in [18]. Although the MIMO BPLC can offer some enhancement to the system capacity, it still cannot offer high ergodic capacity in the VHF band due to the transmitter PSD mask forced by [16]. For cognitive BPLC, the BPLC

Tx uses its coupling circuit to sense the spectrum before transmission to avoid interference with existing wireless services, and hence improve the overall ergodic capacity of the system. The coupling circuit is the circuit used to connect the BPLC transceiver to the power line network, it protects the transceiver from the mains voltage and filters the communication signal in the desired band. The main drawback in the cognitive BPLC is the weak reception capability of the BPLC coupling circuit to VHF wireless signals, due to the near field coupling loss between the BPLC and the VHF wireless channels as previously addressed in [33]. Besides, even for the MIMO cognitive BPLC, the coupling circuit itself is considered as a passive circuit device that can increase the coupling loss of the wireless signal. Also, weak coupling between the power line signals and the wireless VHF band can lead to a long sensing time that yields a capacity loss. In [50–54] preliminary studies were presented for sensing the wireless signal through an antenna, which can be added to the BPLC Rx. The measurement results in [51–53] prove that the wireless signal received by the antenna can be used in spectrum sensing for the BPLC communication. Also, in [54] further measurement results prove that the antenna can be used in the VHF band to exploit the radiation of the BPLC signal to enhance the reception diversity of the BPLC Rx.

As for hybrid wireless BPLC, WiFi was proposed in [18] to enhance the capacity of BPLC by building up a hybrid BPLC WiFi transceiver. The solution relies on the cooperation between the BPLC transceiver in the frequency band below 30 MHz with a transmitter PSD of -55 dBm/Hz [16] and the WiFi transceiver in the 2.45 GHz band with transmission power limit of 23 dBm [63], which is equivalent to -50 dBm/Hz for 20 MHz bandwidth. However, when the BPLC transceiver is

used in the frequency band beyond 30 MHz, it suffers a lower transmission PSD limit of -85 dBm/Hz [16] while the WiFi transceiver in the 2.45 GHz band still has the same transmission power limit of 23 dBm. This limit difference results in allocation of most transmission power to the WiFi channel which suffers a higher path loss compared to the BPLC channel [64]. This leads to an overall capacity degradation, compared to the BPLC WiFi capacity in the frequency band below 30 MHz.

2.6 BPLC Deployment into TVWS

2.6.1 Cooperation between BPLC and TVWS: Is it practical?

In table 2.1, a summary is presented for the comparison between the TVWS and the BPLC in terms of the regulations, standards and channel characteristics. The comparison shows the convergence between TVWS and BPLC in the following aspects: 1) the two technologies span common part of the VHF band, which enables cooperation between them to exploit that band, 2) the BPLC channel has the minimum coherence bandwidth of 65.5 kHz. Hence, utilising the TVWS standard in the BPLC communication is applicable as the subcarrier frequency spacing is 53.5 kHz, which is less than the coherence bandwidth of the BPLC; 3) the TVWS standard introduces the minimum symbol duration of 13.8 μs. Hence, utilising the TVWS as a standard in the BPLC channel is also applicable as the OFDM symbol duration is greater than the rms delay of the BPLC channel, 4)

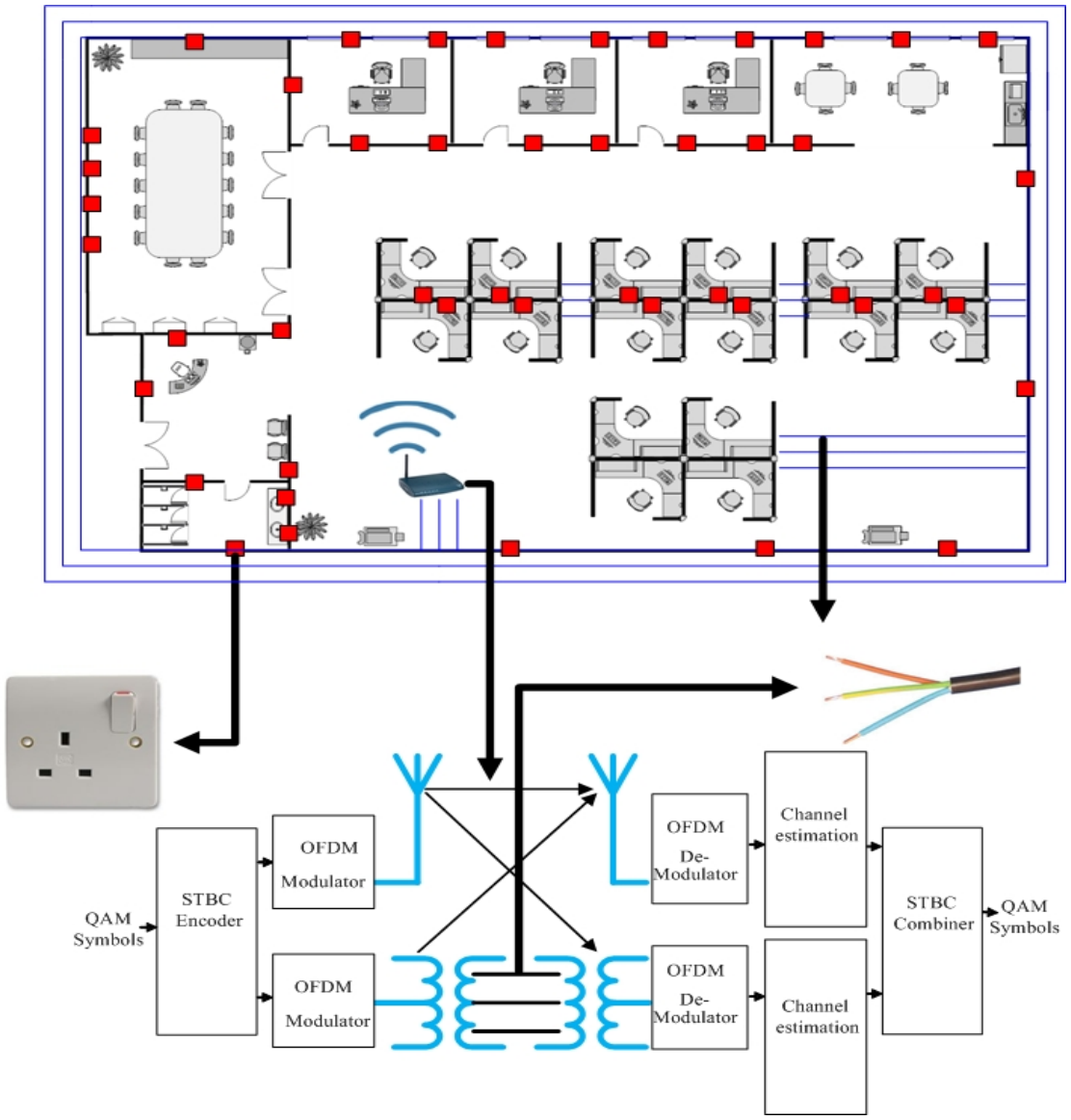

FIGURE 2.3: System model of cooperative BPLC TVWS system in office environment

the path loss introduced by the TVWS and BPLC channels lies approximately in the same range. Hence, the MIMO techniques such as STBC or SM may be used to enhance the achievable throughput.

A cooperative BPLC TVWS system is illustrated in Fig. 2.3. At the Tx side, each quadrature amplitude modulated (QAM) symbol is coded using space time block code (STBC). The output of the STBC is then split into two paths: 1) Wireless TVWS, and 2) BPLC, where each path adopts OFDM to allocate specific

Table 2.1: Comparison between TVWS and BPLC

	TVWS	BPLC
PSD (dBm/Hz)	-47.7 (non-adjacent channel) / -51.7 (adjacent channel)	-55 (< 30 MHz) / -85 (> 30 MHz)
Developed Standards	IEEE 802.11af, IEEE 802.22 IEEE 802.15.4m, IEEE 802.19.1, IEEE 1900.7, ECMA-392	IEEE 1901, HomeplugAV1, HomeplugAV2
Frequency band (MHz)	54 - 806	1.8 - 100
Number of subcarriers	128 for each 6 MHz channel (ECMA-392)	3455 (HomeplugAV2)
Subcarrier frequency spacing (kHz)	53.5, 62.5 and 71.42	24.414
OFDM symbol duration (μs)	18.667, 16 and 13.8	40.96
GI duration (μs)	2.33, 2 and 1.725	4.96
Frame preamble and header duration (μs)	74.668, 64 and 55.2	55.5
Frame payload maximum number of bytes (byte)	4095	4095
Channel Path loss at 100 MHz for coverage distance 15 m - 50 m (dB)	51 - 81	38 - 81
Channel coherence bandwidth (kHz)	200	65.5 - 691.5
Channel rms delay (ns)	100	413

frequency channels to each user. At the Rx, the received signals from the BPLC coupling circuit and the TVWS wireless antenna are combined using an STBC combiner. The combined symbols are passed through a maximum likelihood (ML) detector to allow estimation of the transmitted symbols. As illustrated in Fig. 2.3, the system is within office environment, where the sink can be connected to the main distribution box of the office and the other transceivers can be connected

to any outlet in the office. This creates point-to-multi-point communication case, which is further discussed in Chapter 6.

2.6.2 Potential Advantages of BPLC and TVWS Cooperation

Cooperation between TVWS and BPLC can be achieved without adding up- or down-converter components (compared to other hybrid systems like the BPLC WiFi), since both technologies can access the VHF band. Hence, this cooperation has twofold benefits for TVWS and BPLC communication systems, which can be summarised as:

- For TVWS, BPLC supports the TVWS with MIMO capability in the VHF band, which improves significantly the achievable throughput, and overcomes the aforementioned footprint design challenges in [19] and [20].

- BPLC supports the SU in the TVWS channels with a backup free channel in the high frequency (HF) band (1.8 MHz - 30 MHz). This facility can be utilised in the streaming services, to minimise the total delay time.

- TVWS supports the BPLC communication in the VHF band with higher PSD under the umbrella of the FCC regulations. Hence, the power is efficiently distributed between the HF and VHF band, which yields a higher capacity.

- TVWS supports the BPLC with higher input power due to the increase in the PSD of the VHF band. Hence, using this power, the coverage area and

the number of accommodated users can increase. It is worth mentioning that the maximum allowed input power for the BPLC is 282 mW, which is mostly concentrated in the HF band. Hence, using higher power (which is feasible in a TVWS standard compliant system) can significantly improve the coverage area for point to multi-point communications in smart grid multimedia applications.

2.7 Summary

In this Chapter, two indoor emerging technologies (*i.e.* BPLC and TVWS) have been investigated. The regulations, standards and the channel characteristics of each technology have been presented. A brief comparison between TVWS and BPLC is then made, which shows the feasibility of cooperation between these two technologies. TVWS has challenges in using MIMO techniques in the VHF band, while the BPLC suffers a high restriction on its PSD in the VHF band for EMC issues. Also, previous work done to enhance the BPLC capacity has been shown. Insufficiency has been pointed in the previous VHF BPLC capacity enhancement schemes. For the BPLC channel, a general path loss mapping is required to represent different BPLC topologies and deeper investigation is needed to model the interference of the wireless signal to the BPLC signal. In Chapter 3, the BPLC and TVWS channels are deeply investigated. A general path loss mapping approach for the BPLC channel is proposed. Also, a comparison is held between the BPLC channel path loss and the TVWS path loss to find out the feasibility of their cooperation.

Chapter 3

BPLC and TVWS Channel Modelling

3.1 Introduction

In Chapter 2, previous approaches to map the path loss of the BPLC channel were discussed. The lack of general BPLC path loss model was discussed, which could represent the path loss of most of the BPLC indoor topologies. In this Chapter, the BPLC and the TVWS channels are modelled along with the crosstalk channel, and a General Statistics Based Path Loss Mapping approach is proposed for BPLC referred to as (GSBPLM).

The Chapter is organised as follows. Section 3.2 presents the proposed GSBPLM criteria to map the path loss for each PLC channel class. Also, the section presents a proposed simplification method adopted in GSBPLM for BPLC channel transfer function computation referred to as gain roll back (GRB) method. Furthermore, the simulated GSBPLM path loss is compared to the measured one,

and a comparison between the PLC channel path loss and the wireless channel path loss is presented as well. In Section 3.3, the TVWS BPLC crosstalk channel model and measurements are shown. In Section 3.4, the summary of the Chapter is presented.

3.2 GSBPLM PLC Path Loss Mapping

The power line channel is divided into nine classes [26] based on achievable channel capacity (more specifically Shannons Capacity), where channel 1 is the channel with the least capacity and channel 9 is the channel with the highest capacity. In other words, channel 1 represents the worst BPLC channel gain conditions while channel 9 represents the best BPLC channel conditions. The main target of the work is to map the path loss of the PLC channel with all its different scenarios. The work is different from [30] and [31] in the following aspects. First, a novel method is proposed to map the path loss and the coverage distance of each class of the PLC channels in [26] using a statistical approach. A new methodology has been followed in mapping and measuring the power line signal coverage distance. The new methodology depends upon introducing the *electric* coverage distance concept rather than the *geometric* one which was previously used in [31]. This new concept increases the accuracy of the simulated path loss map and decreases the difference between the simulations and measurements. The proposed path loss map is more general than the previous work in [30] and [31] and is applicable for different topologies and environments within each channel class. Since the nine PLC channel classes [26] represent most of the existing power line topologies based

upon practical measurements, the topology which represents each PLC class channel needs to be modeled clearly. Building up nine corresponding random topology generators is proposed, which include all the possible scenarios of the PLC channel environments, leading to more general and practical path loss mapping. Second, a new gain roll back (GRB) approach is used to reduce the computational complexity of the channel transfer function between two arbitrary nodes in a complex power line network. The proposed GRB method is more general and less complex than that in [29], by deriving one general expression for every branch gain. The method takes all the complex situations of the power line network into consideration, leading to more practical results. Another essential advantage of the GRB method is the effect of the adjacent nodes being taken into consideration, which yields more accurate results than the other bottom-up methods [25, 32].

Simulation and measurement results show that the proposed topology generators are able to simulate the nine PLC channel classes effectively. The average channel gain curve of every class of topology generator matches the fitting curve of the corresponding PLC channel class in [26]. The path loss curves of the nine PLC channel classes are generated at different frequencies in the VHF band, and are compared to their counterparts of wireless communications to show the feasibility of the cooperation between the BPLC and the wireless communications in the indoor environments.

Hence, in order to achieve our target, the PLC channel response has to be simulated for every class of the PLC channels presented in [26]. In [28], a statistical model was presented for building up a power line topology. However, this model did not identify the class of the generated topology, and therefore is inadequate

to represent all the different measurement environments of the PLC channels. In this section, the aim is to statistically model the power line topology representing each PLC channel class. Different topology parameters are presented, which are adjustable to build up nine classes of the power line topology generators. Each topology class generator has an average channel gain that represents the gain of the corresponding PLC channel class presented in [26]. The adjustable parameters can be summarised into three categories described below.

3.2.1 Topology Layout

The number of branches has a great impact on the overall channel gain degradation. Hence, controlling the number of branches in each power line topology will define the overall topology class. This is achieved by controlling the area of the small clusters building up the whole topology and the number of the electric outlets within each cluster. In the proposed approach for simplicity, the topology area A_f is assumed to be divided into square-shape clusters of identical area A_{cn} where n denotes the index of the topology class. A_{cn} is assumed to be uniformly distributed over $[A_m, A_M]$, where A_m and A_M represent the minimum and maximum values for each topology class.

3.2.2 Load Distribution

Controlling the model of the load distribution in each topology will determine the class of this topology. The adopted model for the load distribution in the proposed approach classifies the load impedance connected to every outlet into three groups: frequency dependent, frequency independent and open circuit (*i.e.*,

no load connected). Let $Z(\omega)$ denotes the impedance of the frequency dependent loads at frequency ω. It can be expressed as [65]:

$$Z(\omega) = \frac{R_L}{1 + jQ(\frac{\omega}{\omega_0} - \frac{\omega_0}{\omega})} \tag{3.1}$$

where R_L is the load impedance value at resonance frequency, Q is the quality factor and ω_0 is the angular resonance frequency. For the frequency independent loads $Z(\omega) = R_L$ for the whole band, where each load has different R_L value.

3.2.3 Cable Modeling

The power line cable model is essential in determining the class of the topology since it determines the cable attenuation factor and hence determines the overall channel attenuation. In this work, the cable is represented using the empirical relation of [25]: $\alpha(f) = p_{1n} + p_{2n}f + p_{3n}f^2 + p_{4n}f^3$, where $\alpha(f)$ is the cable attenuation factor at frequency f Hz, p_{1n}, p_{2n}, p_{3n} and p_{4n} are the cable constants for the n^{th} topology class.

3.2.4 GRB Method for Channel Transfer Function Computation

The adjacent nodes to the Tx and the Rx influence the overall channel transfer function. However, due to the complexity of power line network, it was difficult to take the effect of adjacent nodes accurately into consideration in the previous work, such as in the impedance carryback method of [28].

In this part, a GRB method is presented for computing the channel transfer function between two arbitrary nodes in a complex power line network. The GRB method has an advantage of reduced computational complexity by breaking down the overall channel gain computation into smaller computation operations for each branch in the power line network, using the time domain approach. The GRB method is also more general than [29], and the calculation of the adjacent nodes effect leads to more practical results.

The time domain approach was previously addressed in [29] to compute the PLC channel transfer function taking the adjacent node effect into consideration. However, the most significant drawback of this approach is the assumption that the obstructed (OBS) branches are terminated with terminal loads only. On the contrary in the real power line networks the OBS branches can be terminated by either another branching node or terminal impedance. Hence, through this part a general formula will be derived for the OBS branch gain taking into consideration the practical case. Finally, a simplification method will be addressed to compute the overall channel transfer function between any two arbitrary nodes in the network using the new general formula derived for the OBS branch gain.

In Fig.3.1, the overall transfer function between the Tx and the Rx can be expressed using the following formula [29]:

$$H(f) = LOS \prod_{i=1}^{n} (OBS_i + 1)(A_L + 1)(A_R + 1) \tag{3.2}$$

where LOS denotes the line-of-sight path gain, OBS_i is the obstructed path gain of the i-th branch, A_L and A_R are the sums of the multipath signal propagating on

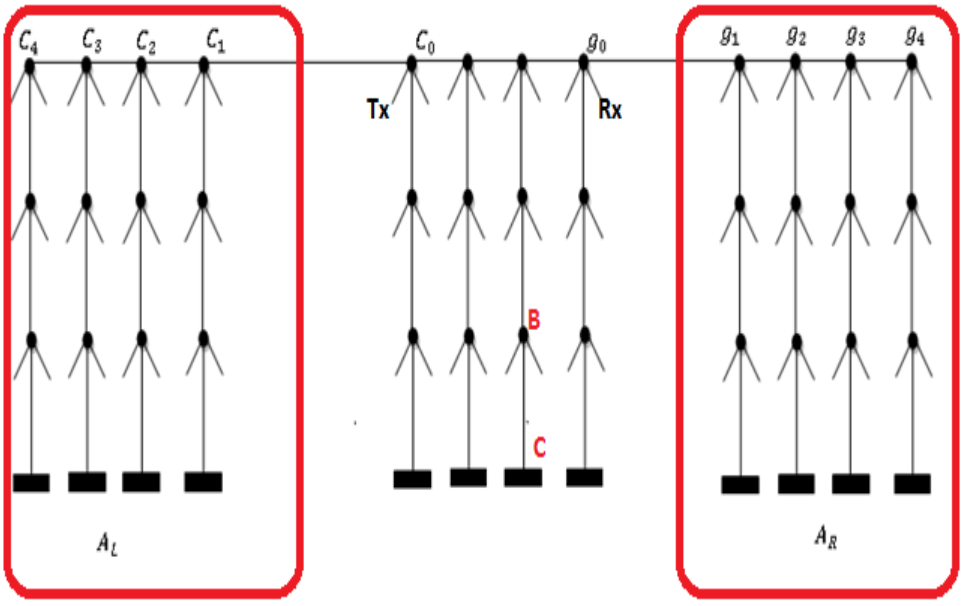

FIGURE 3.1: Power line real network with multiple branches, multiple adjacent nodes

the left hand side of the Tx and the right hand side of the Rx, respectively, and n is the total number of the obstructed branches and paths coming out of the LOS direction. The LOS is given by the product of the transmission coefficients and the line attenuation factor as $\prod_{i=1}^{n}(T_i e^{-\gamma l})$, where T_i represents the transmission coefficient of the i-th branch, γ is the propagation constant and l is the branch length. The $OBS_{q,s}$ for the q-th node and the s-th branch can be expressed as:

$$OBS_{q,s} = \begin{cases} \frac{a_s}{1-r_s} & \text{if } (q+1) \text{ is a terminal node} \\ N_{q+1} + & \text{if } (q+1) \text{ is a branching node} \\ M_{q+1}[\prod_{s=1}^{n}(OBS_{q+1,s}+1)-1] & \end{cases} \tag{3.3}$$

The derivation of (3.3) is shown in Appendix A. It can be deduced that the values of A_L and A_R in (3.2) can be considered as the overall equivalent OBS

TABLE 3.1: The Topology Generator Parameters

Channel Class	A_{mn} (m^2)	A_{Mn} (m^2)	Outlet Density $(\frac{outlet}{m^2})$	ρ_{v1n}	ρ_{v2n}
1	15	45	0.05	0.4	0.1
2	26	45	0.035	0.4	0.1
3	35	47	0.03	0.5	0.05
4	45	55	0.025	0.6	0.08
5	60	70	0.025	0.8	0.08
6	90	100	0.01	0.8	0.08
7	190	200	0.015	0.8	0.2
8	450	480	0.02	0.8	0
9	450	480	0.0125	0.8	0.08

values for the two adjacent branches on the left hand side of Tx and the right hand side of the Rx respectively and hence (3.2) can be rewritten as:

$$H(f) = LOS \prod_{i=1}^{n+2} (OBS_i + 1) \tag{3.4}$$

Consequently, the GRB method can be simplified in the following steps:

1) Determine the line of sight channel gain between the Tx and the Rx.

2) Evaluate the OBS gain of each branch diverting from the LOS path using the general formula (3).

3) Evaluate the overall channel transfer function using (4) taking the adjacent nodes into account.

TABLE 3.2: The Cable Parameters

Channel Class	p_{1n}	p_{2n}	p_{3n}	p_{4n}	Z_{cn} (Ω)
1	1.233e-03	-7.04e-10	1.05e-17	1.12e-26	120
2	5.2e-03	-1.77e-10	1.04e-17	-5.50e-26	122
3	5.2e-03	1.34e-10	3.66e-18	-1.63e-26	80
4	2.7e-03	1.23e-11	5.53e-18	-2.21e-26	80
5	1.8e-03	-7.58e-11	5.74e-18	-1.72e-26	80
6	8.7e-03	-5.32e-10	1.47e-17	-5.94e-26	80
7	4.1e-03	-3.67e-10	1.21e-17	-4.45e-26	80
8	3.2e-03	-1.64e-10	4.83e-18	-1.12e-26	20
9	2.7e-03	-9.65e-11	5.16e-19	7.76e-27	20

3.2.5 Simulations vs. Measurements

Simulation Setup

The adjustable parameters for building up each class of the PLC topology generators are addressed in Table 3.1 and 3.2. The parameters are deduced using iterative procedure that minimises the difference between the simulated model and the fitting curve in [26]. The simulations are held to generate 400 PLC random topologies per each class topology generator. For every class topology, two arbitrary outlets are selected at random and separated by random distance to represent the Tx and the Rx, then the channel transfer function is computed between the two outlets using the GRB approach in subsection 3.3.4. Consequently, the average transfer function is calculated for each class and the average channel gain is computed at different distances for each class topology generator at different frequencies.

In Table 3.1, the maximum cluster area A_M, the minimum cluster area A_m,

the outlet density, the no load ratio ρ_{v1n} and the frequency dependent load ratio ρ_{v2n} are addressed for the nine classes of the random topology generators. The overall topology area A_f is fixed to 500 m^2.

Table 3.2 shows the characteristic impedance Z_{cn} and the coefficients p_{1n}, p_{2n}, p_{3n} and p_{4n} of the empirical relation representing the power line cable for each class.

For the frequency dependent loads, the R, Q and ω_0 are uniformly distributed in the ranges [200, 1800] Ω, [5, 20] and [2,100] MHz respectively. For the simulations, β, α and n in wireless channel model in (2.1) are assumed to be 2.63, 0.65 and 1.5, respectively for the indoor environment as in [24]. FAF in (2.1) is assumed to be zero for simplicity, as the simulated area is assumed to be on the same floor.

Measurement Setup

To validate the simulation results, measurements are held for the power line channel path loss. The measurements were different from the previous ones by introducing the concept of the *electric* distance between the outlets. The electric distance can be defined as the distance along the power line cable connecting the Tx and the Rx. However, the *geometric* distance can be defined as the Euclidean norm between the coordinates of the Tx and the Rx as in [31] regardless of the power line cable length. Hence, the new concept increases the accuracy of the path loss map measured as the electric distance is the effective factor in the signal attenuation not the geometric one. The measurements were held in the Electrical Engineering building of Liverpool University. The building is divided into six floors. Each floor is subdivided into several rooms where each group of rooms

are connected to a dedicated distribution box. The outlets inside each room are connected together via a single phase 3-conductor power line cable.

The measurements have been carried out using both the signal generator (SG) and the network analyser (NA). For the small distances (*i.e.,* $<$ 15 m.) and the calibration process, the network analyser was used for measuring the channel response by knowing the S-parameters. However, for the long distances (*i.e.,* $>$ 15 m.) it was more convenient (due to safety issues regarding extending cables between different rooms) to use the signal generator as a Tx and the network analyser (in the spectrum analyser mode) as a Rx. Two broadband coupling circuits were used in the Tx and the Rx. The loss has been measured in the coupling circuits and the connection cables by measuring their S-parameters using the network analyser for calibration purpose. As the connection cables are short, the loss inside those cables was nearly 0 dB. For the coupling circuits, the loss inside each one was almost constant value of 5 dB in the frequency range 2 MHz-100 MHz. The measurements were carried out between the outlets belonging to the same phase and the same distribution box. The electric distance between each two outlets was calculated knowing the building topology. The measurements were done in different rooms to have an average path loss representation. The channel transfer function was calculated according to the measurement setup:

(a) NA setup:

$$H(f)(dB) = NA(dB) + CouplingCircuitLoss(dB).$$

(b) SG-NA setup:

$$H(f)(dB) = NA(dB) - SG(dB) + CouplingCircuitLoss(dB).$$

FIGURE 3.2: BPLC Coupling Circuit

The distance between each two outlets is measured according to the outlet location:

(a) If the outlets are inside the same room, so the distance is measured along the power line cable connecting those two outlets.

(b) If the outlets are in two different rooms, so the distance is measured along the power line cable between each outlet and the distribution box.

In Figs. 3.2 and 3.3, the coupling circuit and its electronic component structure are shown. The main role of the coupling circuit is to isolate the mains voltage and to couple the communication signal to/from he power line network. The isolation is completely achieved through the 100 pF capacitor and also the inductive transformer. The inductive transformer physically isolates the mains voltage from any measurement device, which guarantees maximum protection. In Figs. 3.4 and 3.5, the practical measurement setup for evaluating the BPLC channel gain

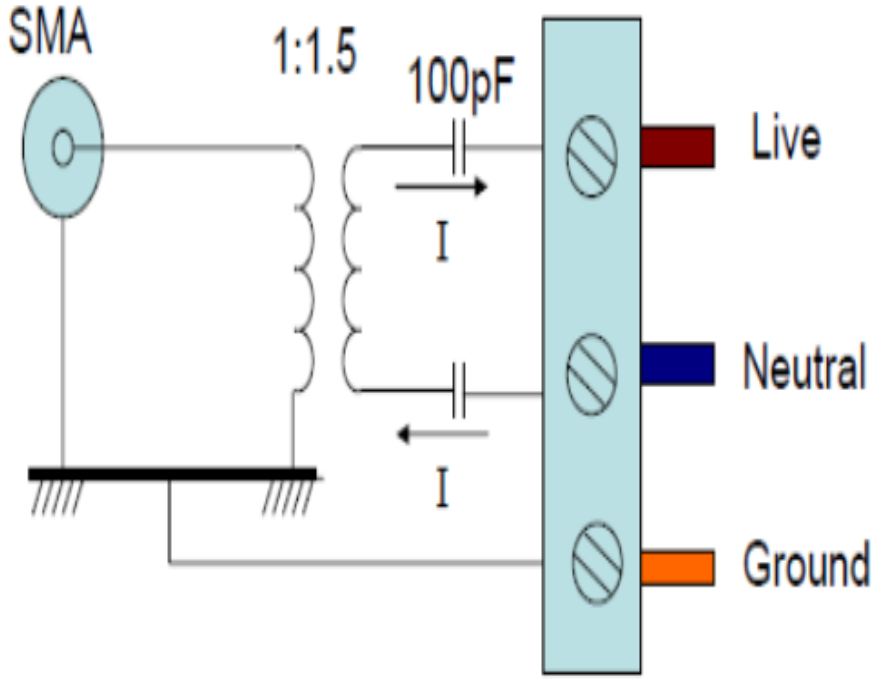

FIGURE 3.3: Schematic diagram of the BPLC coupling circuit [66]

is shown. In Fig. 3.4, the RF signal generator sends the BPLC signal to the power line network via the coupling circuit, while in Fig. 3.5, the network analyser receives the signal through another coupling circuit. The network analyser is adjusted to be in the spectrum analyser mode to calculate the BPLC channel gain. Mapping the measured channel gain versus the distance between the Tx and Rx electric outlets, the path loss curve can be deduced. The measurements are held in rooms 221, 202 and 207 in the second floor of the Electrical Engineering building at the University of Liverpool. Since, the distances between the outlets represent important parameter in our measurements, the room maps are presented in the Figs. 3.6, 3.7 and 3.8.

FIGURE 3.4: RF signal generator sends single tone frequency to the power line network

Simulated vs. Measured PLC Channel Path Loss

Figs. 3.9-3.10 show the path loss measured at frequencies 30 MHz and 100 MHz respectively. Also in the figures the linear fitted curve deduced from the measured data is compared with the corresponding simulated curve of class (1) channel using GSBPLM. The normalised mean square errors (NMSE) are calculated for both fitted curves. The NMSE is calculated according to the following equation:

$$NMSE = \frac{\| x_{meas} - x_{fit} \|^2}{\| x_{meas} - mean(x_{meas}) \|^2} \tag{3.5}$$

where x_{meas} and x_{fit} represent the measured and fitted data respectively. It is found that the difference in the NMSE between both fitted curves is: 0.05 and 0.04 at frequencies 30 MHz and 100 MHz respectively. Also, computing the correlation

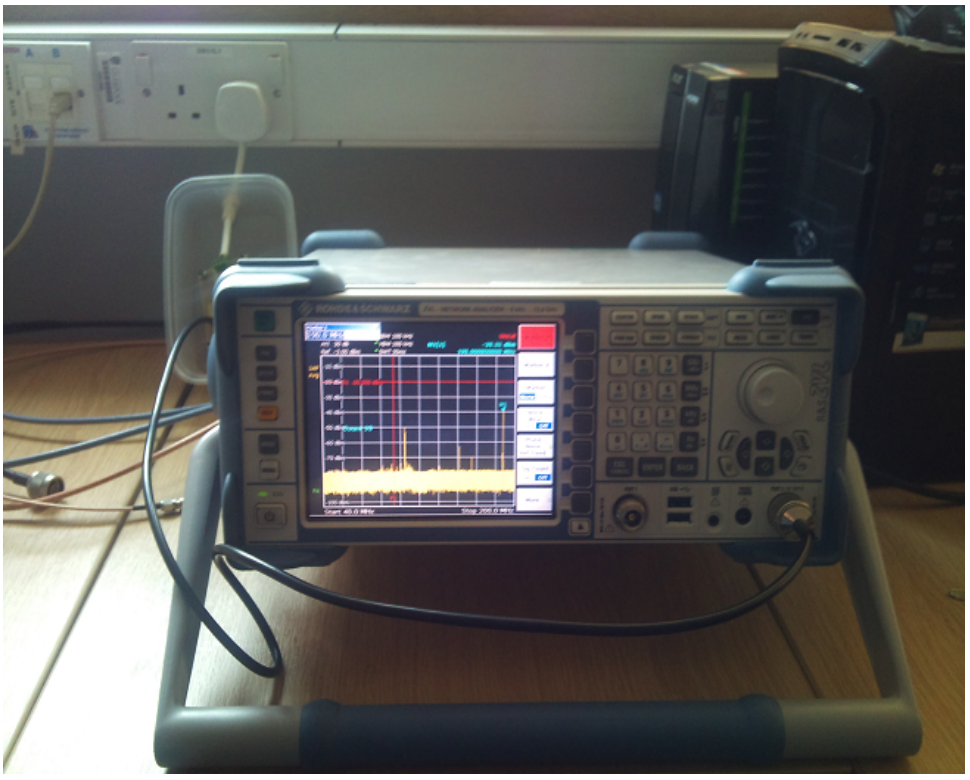

FIGURE 3.5: Network analyser receives the power line signal

coefficient between the measured and fitted data, the result is 0.857. This result proves that the simulated path loss agrees with the real measurement data that further proves the feasibility of the proposed path loss mapping approach.

Simulated Average PLC Channel Gain

In Fig. 3.11, the channel transfer functions in the frequency range 2 MHz-100 MHz are plotted for the class (1) random topology generator. It is worth mentioning that class 1 power line channel has been mostly measured and addressed in previous literature [18][67][68][31], hence, its average channel path loss can be deduced as

$$PL_{\text{BPLC}}(dB) = (a_1 f^2 + a_2 f + a_3)d + (b_1 f^2 + b_2 f + b_3) \tag{3.6}$$

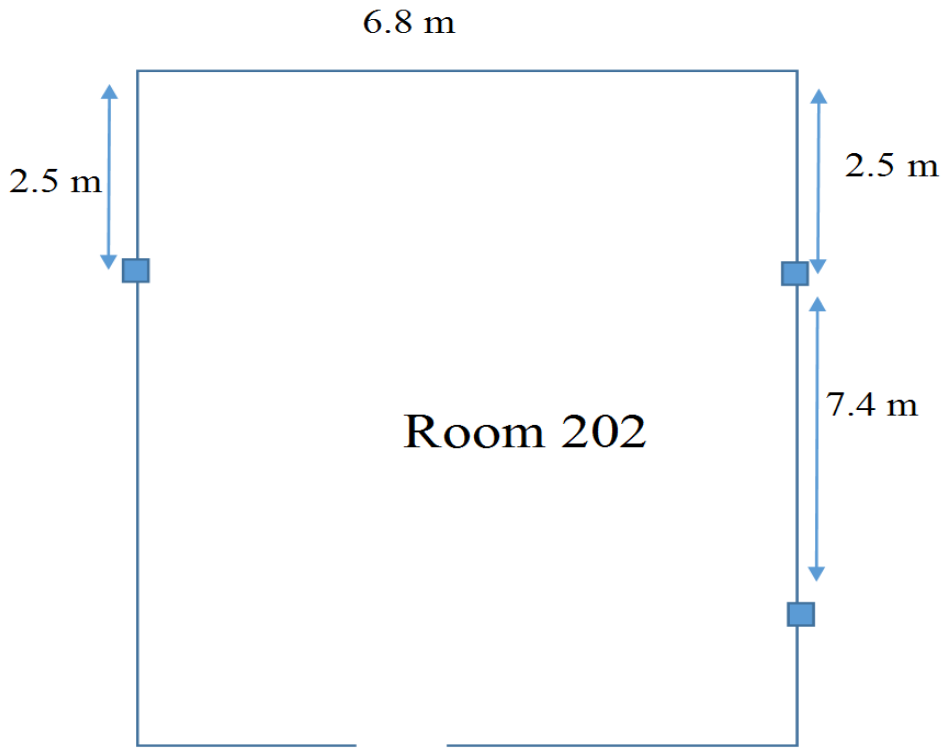

FIGURE 3.6: Outlet distribution map in room 202 in the Electrical Engineering building of Liverpool University, the blue squares represent the electric outlets locations

where f is the frequency of operation in MHz, d is the electric separation distance in meters (*i.e.*, the length of the separating power line cable), $a_1 = -1.14 \times 10^{-4}$, $a_2 = 6.8 \times 10^{-3}$, $a_3 = -0.91$ and $b_1 = 2.97 \times 10^{-4}$, $b_2 = -0.061$, $b_3 = -15.0$. In Fig. 3.12, the overall average transfer functions of the nine classes are plotted together with the corresponding fitting curves. The matching can be observed between the average transfer function generated and the fitting curve representing each class according to [26], which further proves the validity of the proposed topology generator in representing the corresponding class of the power line channels.

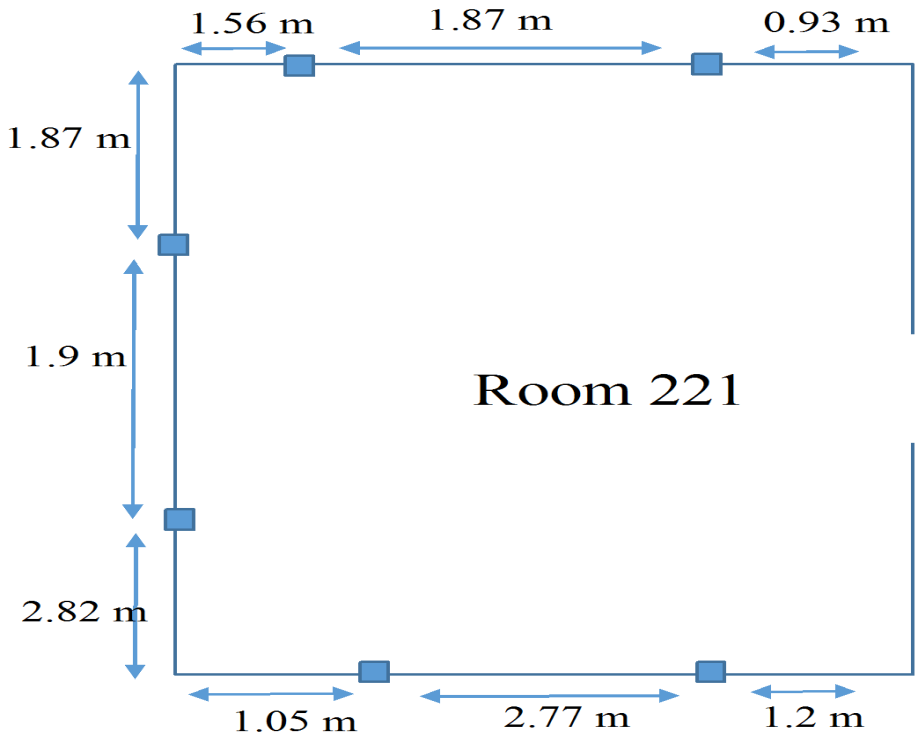

FIGURE 3.7: Outlet distribution map in room 221 in the Electrical Engineering building of Liverpool University, the blue squares represent the electric outlets locations

Simulated Path Loss of PLC vs. Wireless Channel

In Figs. 3.13-3.14, the path loss curves for the nine PLC classes are deduced from the nine topology generators within a coverage distance below 60 m. The fitting curve for each class is drawn at frequencies 30 and 100 MHz. Also the GUPL model is drawn to represent the path loss for the wireless channel in the indoor environment at the same frequencies and within the same coverage distance range. It is worth mentioning that the distance considered in the GUPL model is the geometric distance. However, the distance for PLC path loss is the electrical one. It can be easily concluded that the electrical distance is greater than or equal to the geometrical one. In Figs. 3.13-3.14, it can be observed that for a coverage distance below 60 m, the path losses of the PLC classes 1-5 together with the

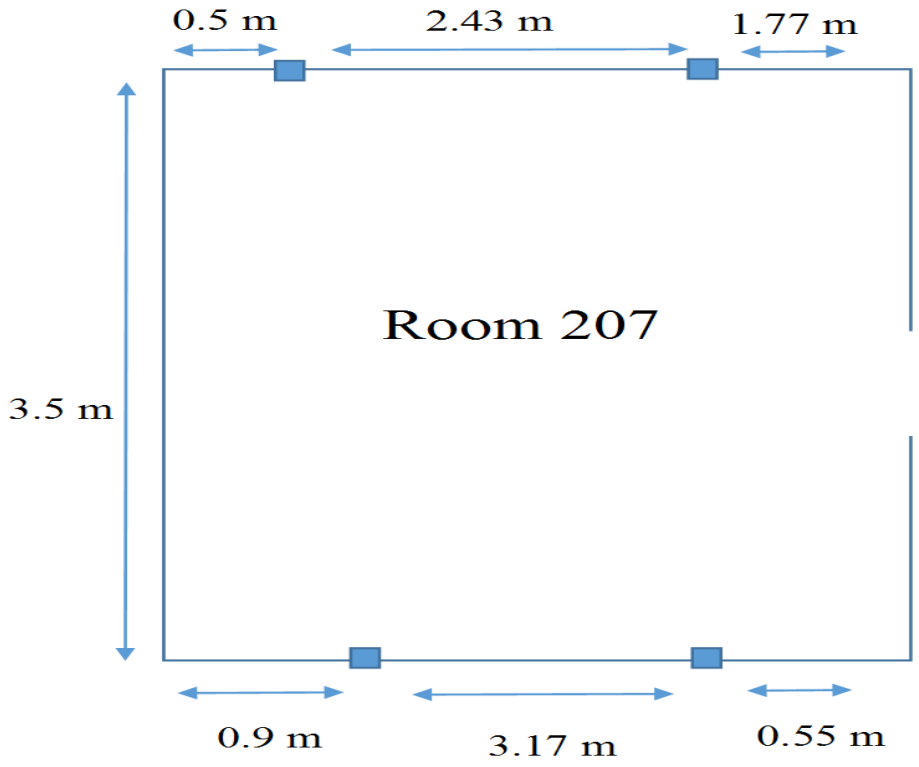

FIGURE 3.8: Outlet distribution map in room 207 in the Electrical Engineering building of Liverpool University, the blue squares represent the electric outlets locations

path loss of the wireless channel exceed 40 dB at different distances. Hence, the cooperation between the PLC and the wireless communication becomes feasible in the indoor environment, taking into consideration the difference between the electric and the geometric coverage distances. However, further study should be considered for the other parameters affecting the cooperation between the BPLC and the wireless communications.

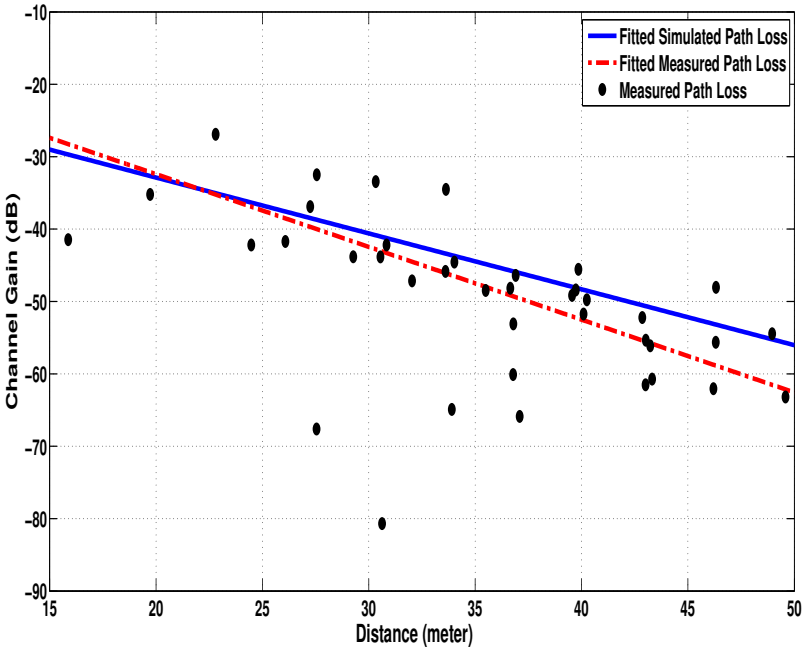

FIGURE 3.9: The measured, fitted and simulated path loss curves of class 1 PLC channel at 30 MHz.

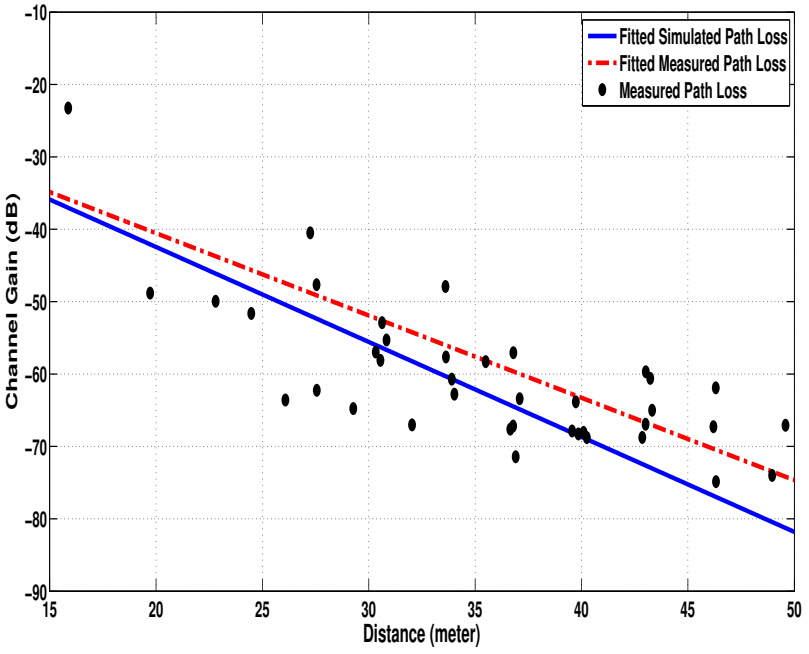

FIGURE 3.10: The measured, fitted and simulated path loss curves of class 1 PLC channel at 100 MHz.

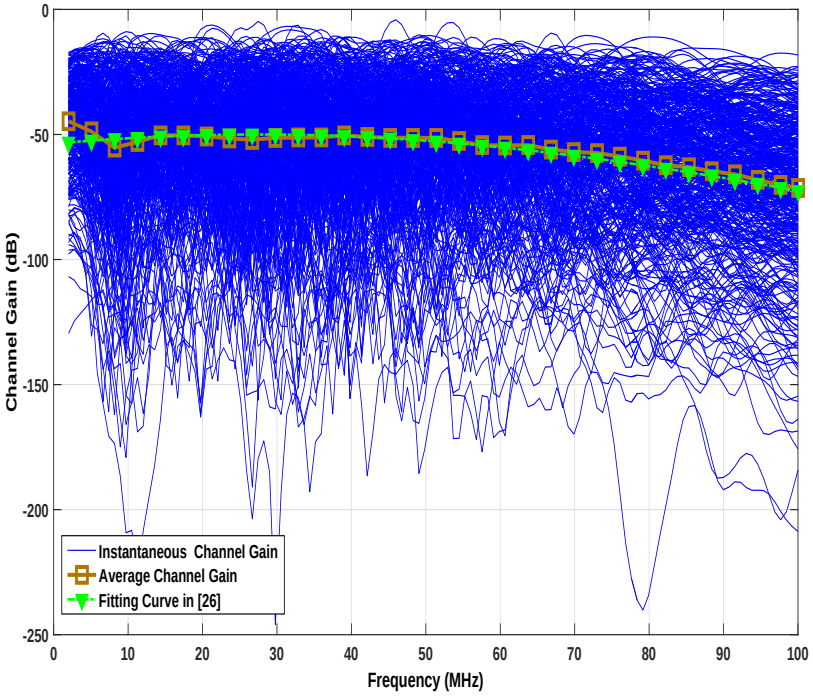

FIGURE 3.11: The transfer functions generated from class 1 topology generator.

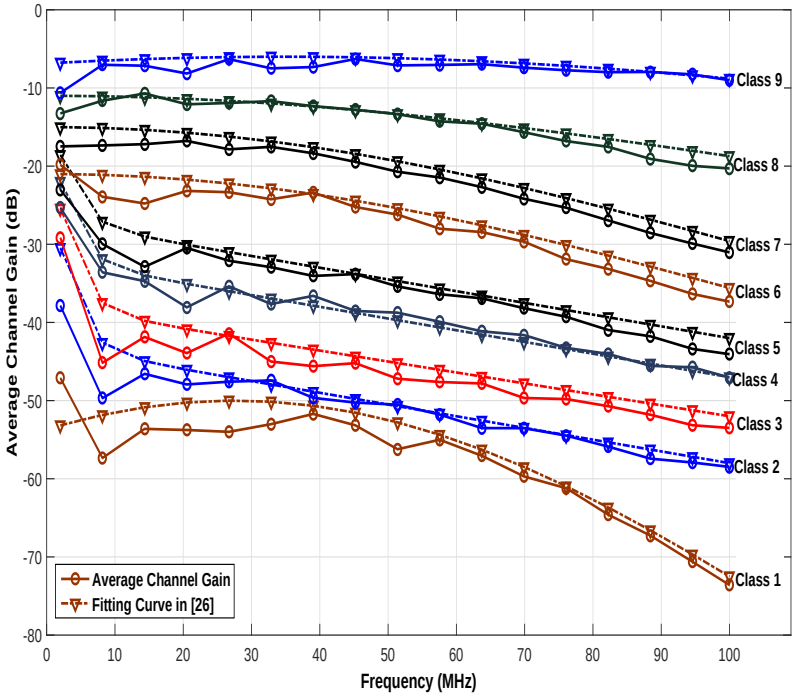

FIGURE 3.12: The average transfer functions of the nine classes generated by the nine topology generators and the fitting curves representing the nine classes.

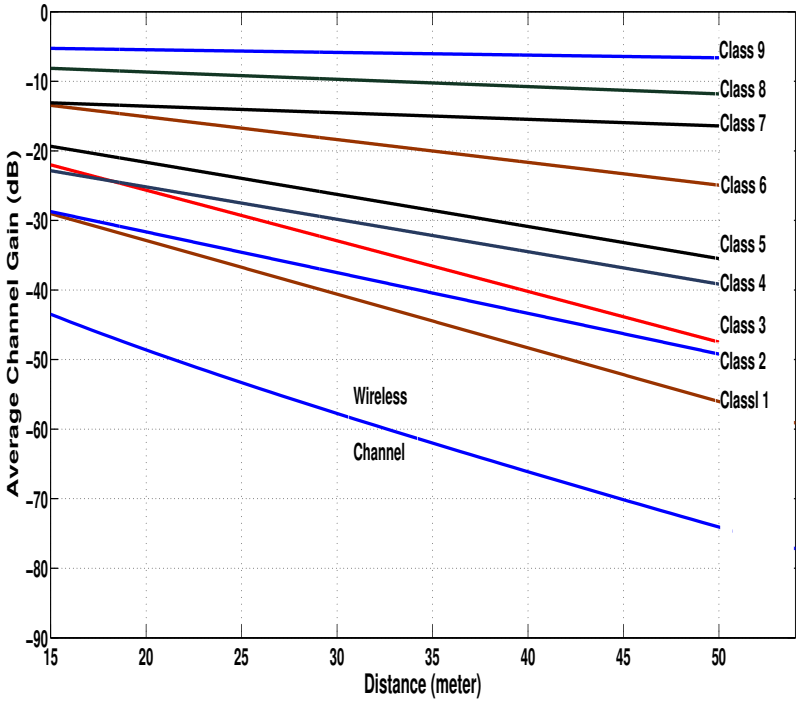

FIGURE 3.13: The deduced path loss curves of the nine classes of the power line channel and the path loss curve of the wireless channel at frequency 30 MHz.

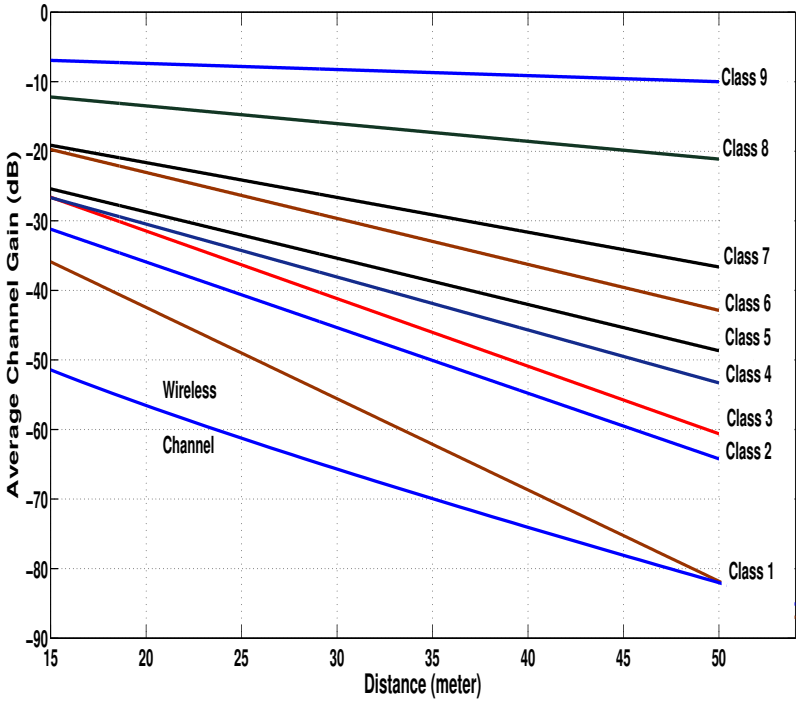

FIGURE 3.14: The deduced path loss curves of the nine classes of the power line channel and the path loss curve of the wireless channel at frequency 100 MHz.

3.3 Modelling the Crosstalk between TVWS and BPLC Channels

As aforementioned, the TVWS wireless channel path loss is represented using the GUPL model in [22]. In this work, the indoor wireless channel is represented using 3-level model, which considers three superimposed effects: 1) Two path Rayleigh fading channel for the multipath effect [69], with rms delay spread of 6 μs, 2) Shadowing effect, and 3) Path loss effect. Both shadowing and path loss effects are modeled using the GUPL model in (2.1).

For the cross talk between the TVWS and BPLC channels, the near field coupling between broadband power line and high frequency communication systems has been addressed in [33]. It depends on several factors like the cable properties, the coupling circuit and the network asymmetric loads.

In this section, the measurements done in the previous sections for the BPLC channel are continued to include the crosstalk between the BPLC and the wireless channel. The aim of the measurements is to model the path loss of the crosstalk channel and compare it with the path loss of the corresponding BPLC and TVWS channels. The measurements are held inside the labs of the electrical engineering and electronics department of Liverpool University. The Tx and the Rx are located at the same floor. The channel between any two power line couplers is represented by the network of the power line cables, while the channel between any two wireless antennas is the radio propagation channel. The path loss is measured using a RF signal generator at the Tx and spectrum analyser at the Rx. The frequency band of operation is 84 MHz - 200 MHz, but the frequency modulation

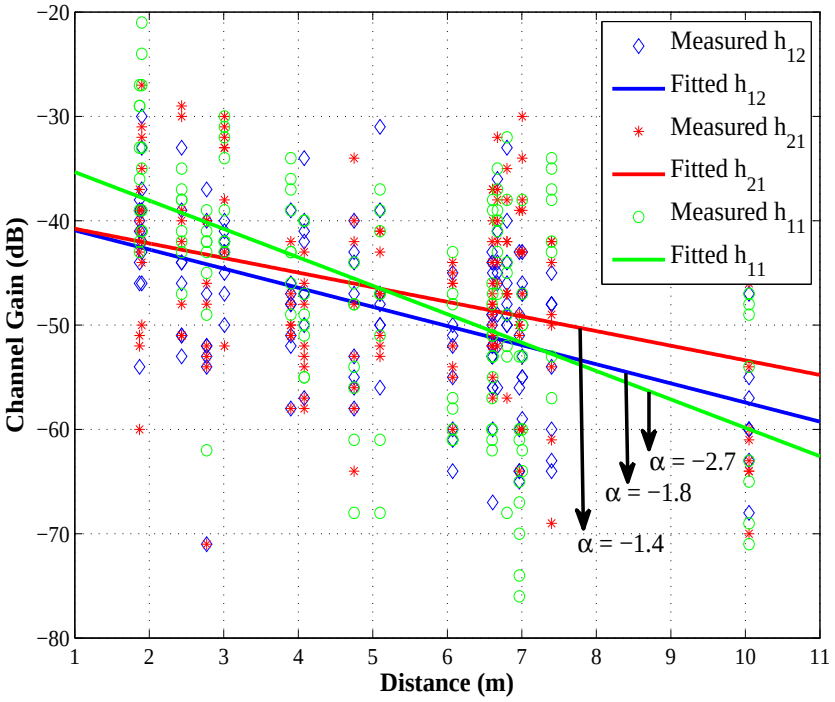

FIGURE 3.15: Crosstalk channel compared to the BPLC channel

(FM) band from 88 MHz - 110 MHz is avoided, due to the interference from the FM radio station. The path loss is measured for three different channels: 1) the channel between two power line coupling circuits, referred to as h_{11}; 2) the channel between a coupling circuit at the Tx and wireless antenna at the Rx, referred to as h_{12}; 3) the channel between wireless antenna at the Tx and power line coupling circuit at the Rx, referred to as h_{21}.

In Fig. 3.15, the gain of the crosstalk channel is shown versus the gain of the BPLC channel. The channel gain is measured at four frequencies in the band 84 MHz - 200 MHz, which are 84 MHz, 110 MHz, 140 MHz and 190 MHz. The gain is measured for each frequency at different coverage distances to model the path loss of the channel. The measurement results show convergence between the gain of the BPLC channel and the crosstalk channel, since the slope α of the fitted channel

gain takes the values of -2.7, -1.8 and -1.4 for the h_{11}, h_{12} and h_{21}, respectively. Also the results show that the crosstalk channel gain is below the BPLC channel gain for small coverage distance; however, for long coverage distances the crosstalk channel gain outperforms the corresponding BPLC channel gain. This is due to the dependence of the crosstalk channel gain mainly on the geometric separation distance between the Tx and the Rx. However, BPLC channel gain is mainly dependent on the electric separation distance, which is the length of the power line cable connecting the Tx to the Rx. It is known that the electric distance is longer than the geometric distance as reported in [67]. Consequently, the average gain of the crosstalk channel can be concluded to be comparable to the average gain of the main BPLC or wireless TVWS channels. This agrees with the results addressed in [50–54], where the crosstalk between the BPLC and the wireless channel was exploited to enhance the reception of the BPLC signal. Hence, to simplify the analysis, the BPLC (Tx)-TVWS (Rx) channel can be represented as the sum of the BPLC-BPLC loss ($PL_{\mathrm{B-B}}$) and the TVWS BPLC (PL_{c}) coupling loss (The average value of the coupling loss considered in this Chapter is taken from the results of the carried out measurements which is 2 dB). Also the TVWS (Tx)-BPLC (Rx) channel is represented as the sum of the TVWS-TVWS ($PL_{\mathrm{T-T}}$) loss and the TVWS-BPLC coupling loss. This is illustrated in the following equation

$$\begin{aligned} PL_{\mathrm{BPLC-TVWS}}(dB) &= PL_{\mathrm{B-B}}(dB) + PL_{\mathrm{c}}(dB) \\ PL_{\mathrm{TVWS-BPLC}}(dB) &= PL_{\mathrm{T-T}}(dB) + PL_{\mathrm{c}}(dB) \end{aligned} \tag{3.7}$$

The noise model adopted in this work has two components: 1) the background

noise, which is assumed to be zero mean additive white Gaussian noise (AWGN) with variance σ_z^2, and 2) the impulsive noise, which is represented using the model in [70]. Also, the narrow band interference is considered as a cognitive system in the form of PU interference with variance σ_p^2.

3.4 Summary

In this Chapter, a general statistical based path loss mapping (GSBPLM) approach has been proposed, which represents the path loss of individual PLC channel classes. For this purpose, the corresponding nine classes of random topology generators have been built up, each class generator having an average attenuation profile similar to the corresponding PLC channel class. The GSBPLM is applicable to different scenarios and removes the contradiction between previous mapping approaches. The generated path loss curves for the BPLC are comparable to their counterparts for wireless communication in the VHF band, proving the feasibility of cooperation between the two communication technologies indoors. Also, the adopted VHF wireless complex indoor channel gain has been presented together with the measurements of the crosstalk channel between the BPLC and TVWS channels. The measurements have shown convergence between the path loss of the crosstalk channel and the path loss of both the TVWS and BPLC channels. In Chapter 4, theoretical analysis will be presented for the crosstalk between TVWS and BPLC channels, through modelling the excited antenna current by the TVWS signal along the BPLC cables. Also, the Chapter will investigate the conversion

of this antenna mode current to differential mode, which is the dominant mode in the BPLC communications.

Chapter 4

TVWS Excited Antenna Currents across BPLC Cables

4.1 Introduction

Wireless signals in the VHF band interferes with the BPLC signal through antenna mode current excitation. In Chapter 3, the BPLC and TVWS channels were investigated and their path losses were mapped. Also, measurements had shown the crosstalk between both channels. However, theoretical analysis for the TVWS signal interference to the BPLC signal can give a better understanding for the crosstalk between the two channels. Hence, in this Chapter, a general model is constructed for the VHF current conversion from antenna to differential mode across TLs terminals. The proposed model includes the derivation of a general formula for the characteristic impedance of the antenna mode current. Two approaches are proposed to the formulated problem: 1) ATN approach; 2) ETLA analytical approach. The model is important in predicting the amount of antenna

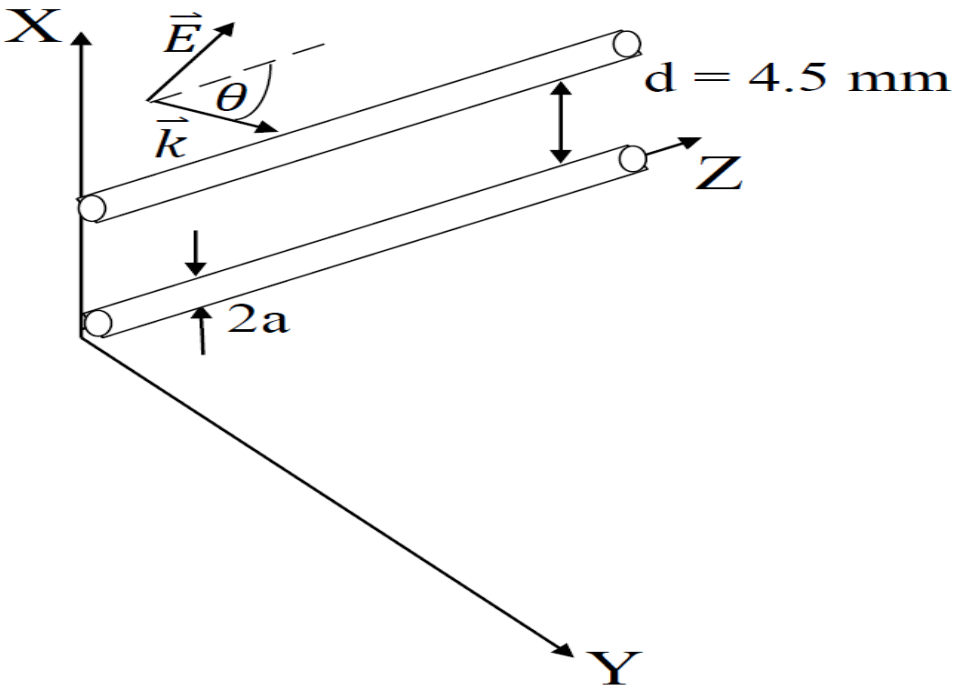

FIGURE 4.1: TL model of straight wires

mode power transmitted or reflected at the terminals of the TL and hence, the amount of antenna mode interference to the differential mode signals. This work is different in the following aspects. *First*, the high frequency (more specifically the VHF) excitation of the antenna mode current is investigated. A comprehensive analysis is provided on the antenna mode current characteristic impedance since this is critical for determining the amount of the antenna mode power that converts to the differential mode and causes interference to the differential signal.

Second, this is the first work to adopt the antenna theory to construct a general ATN solution for representing the antenna mode characteristic impedance. While in [44–48], the antenna theory approach was limited to current derivation. *Third*, the ETLA analytical approach is proposed to represent the mean value of the antenna mode current characteristic impedance. Unlike [45], where the characteristic

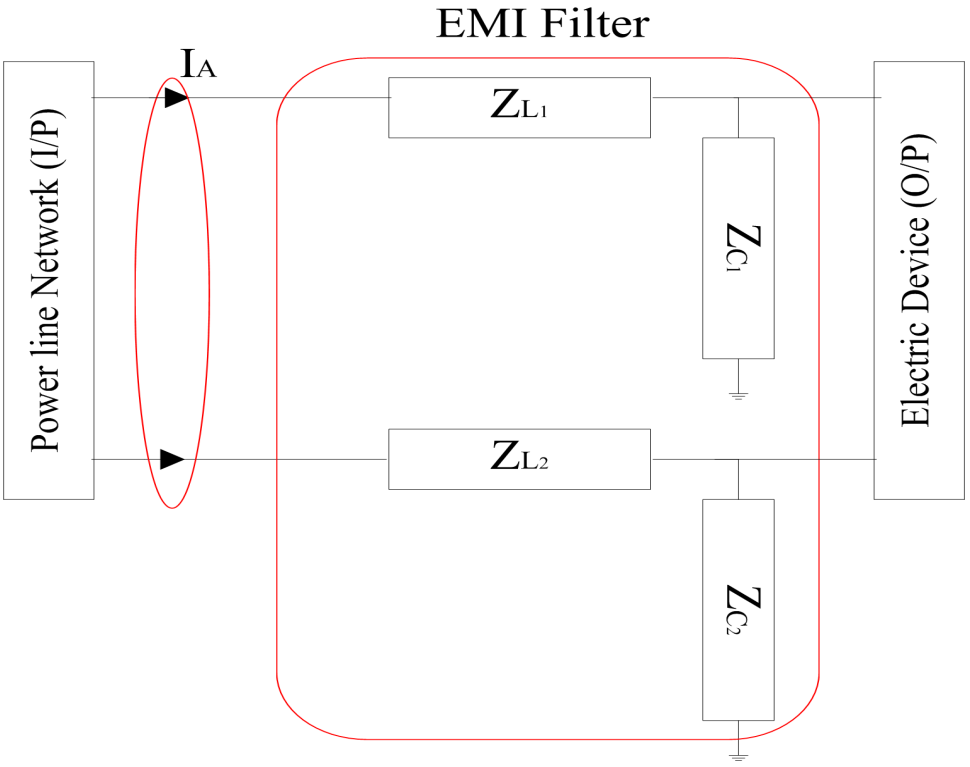

FIGURE 4.2: Two-wire TL terminated with EMI filter

impedance is independent of the exciting frequency effect, the analytical ETLA solution is applicable to the whole VHF band. The proposed solution emphasises the impact of the exciting frequency and incident angle on the mean value of the antenna mode characteristic impedance.

Section 4.2 presents the system model. Section 4.3 introduces the antenna theory approach and the construction of the Green's functions for the excited current, volt and magnetic vector potential. Section 4.4 presents the construction of both the ATN and ETLA solutions for representing the antenna mode characteristic impedance. Section 4.5 shows the simulation results from the two proposed solutions. Furthermore, the simulation for the mode conversion from antenna to differential mode is presented. Section 4.6 summarises the Chapter.

4.2 System Model

In this Chapter, the case of two parallel straight wires in the free space is investigated, as illustrated in Fig. 4.1. Each wire has a length of 40 m and a radius of 1.5 mm. The distance between the two wires is assumed to be 4.5 mm and the maximum operating frequency is 300 MHz. This means that the transverse dimensions of the wires are electrically small, which satisfies the first two conditions in the TL theory and supports the thin wire approximation. The wires are assumed to be along z-axis. The electric field is assumed to be vertically polarised in the XZ plane where θ represents its angle of incidence on the two wires. Here, a plane wave approximation is assumed, which means that the wires are in the far field region of the wireless signal source, which implies that the electric field has the same incidence angle along the wire length. This can be applied in the case of TV signals incident on indoor power line cables.

The EMI filter is a passive device that is used to suppress conducted interference and, is used to protect a device from outside interference or protect the outside environment from unwanted signals generated by the device. However, the asymmetry in the EMI filter with respect to the ground can cause mode conversion between antenna and differential mode signals [55].

In Fig. 4.2, a two-wire TL terminated by EMI filter is shown. The equivalent circuit is the same as that presented in [71]. $Z_{L1,2}$ represents the equivalent impedance of the EMI filter coil which can be modeled by parallel R-L-C circuit with values $14.42k\Omega$, $3.09mH$ and $8.14pF$. Also, $Z_{C1,2}$ represents the equivalent impedance of the EMI filter capacitance towards the ground. This capacitance can

be modeled by a series R-L-C circuit with values $74m\Omega$, $9.96nH$ and $6.9nF$. All the values of R-L-C are the same as those in [71]. It is assumed that the asymmetry ratio between the transmission line components is 0.3, *i.e.*, the components of the two transmission lines differ from each other by 30% in value. This asymmetry value is assumed for industrial errors. A 100 mA antenna mode current is assumed to be excited by the plane wave along the TL. Since each TL is terminated with different impedance, each line shows different transmission coefficient. Hence, differential signals will occur across the line terminals leading to the generation of harmful interference. The interference power P_{t_i} can be defined as the power of the differential signal induced by the antenna mode current at the TL terminals, by any of the mode conversion mechanisms. The calculation of P_{t_i} and the model of mode conversion are discussed in detail in Appendix B.

4.3 Characteristic Green's Functions Construction

In this section, the aim is to construct an antenna potential Green's function (APGF) that represents the potential induced along the TL when applying a delta external electric field to a perfect conducting TL in free space. In the same sense, the aim is to construct the rest of the characteristic Green's functions like the magnetic vector potential Green's function (MVGF) and the charge density Green's function (CDGF). Using the Green's functions of the antenna potential, the magnetic vector potential, the charge density and the antenna current, the general solution can be derived for the antenna mode characteristic impedance in

Section 4.4. The construction of the aforementioned Green's functions is mainly based on the derivation of the antenna current Green's function in Appendix C.

Charge Density Green's function

The charge density $\rho(\mathbf{r})$ can be expressed using the continuity equation as

$$\rho(\mathbf{r}) = \frac{-1}{j\omega}\frac{\partial \mathbf{J}(\mathbf{r})}{\partial \mathbf{r}} \tag{4.1}$$

Applying (C.11) in (4.1), it can be deduced

$$\rho(\mathbf{r}) = \frac{-1}{j\omega}\frac{\partial}{\partial \mathbf{r}}\int_l \mathcal{L}_{\mathbf{r}}^{-1}\delta(\mathbf{r}-\mathbf{r}')\mathbf{E}_t^{ex}(\mathbf{r}')d\mathbf{r}' \tag{4.2}$$

The charge density Green's function can be concluded G_{CD} as

$$G_{\mathrm{CD}}(\mathbf{r},\mathbf{r}') = \frac{-1}{j\omega}\frac{\partial}{\partial \mathbf{r}}G_{\mathrm{AC}}(\mathbf{r},\mathbf{r}') \tag{4.3}$$

Antenna Potential Green's function

Let $\phi(\mathbf{r})$ be the retarded scalar potential. Also, let $\mathbf{r}''$ be the position vector of the impressed excitation electric field, $\mathbf{r}'$ be the position vector for the excited current and $\mathbf{r}$ be the position vector for the observation point of induced potential. An expression can be found for the antenna potential Green's function as

$$\phi(\mathbf{r}) = \frac{1}{4\pi\epsilon_0}\int_l G_{\mathrm{fs}}(\mathbf{r},\mathbf{r}')\rho(\mathbf{r}')d\mathbf{r}' \tag{4.4}$$

where $G_{\text{fs}}(\mathbf{r}, \mathbf{r}')$ is free space Green's function described by

$$G_{\text{fs}}(\mathbf{r}, \mathbf{r}') = \frac{e^{-jk_0|\mathbf{r}-\mathbf{r}'|}}{|\mathbf{r}-\mathbf{r}'|} \tag{4.5}$$

Substituting (C.11) and (4.1) into (4.4), It can be deduced

$$\begin{aligned} &\phi(\mathbf{r}) = \\ &\quad \frac{-1}{4\pi\epsilon_0 j\omega} \int_l \int_l G_{\text{fs}}(\mathbf{r}, \mathbf{r}') \frac{\partial}{\partial \mathbf{r}'} \mathcal{L}_{r'}^{-1} \delta(\mathbf{r}' - \mathbf{r}'') \mathbf{E}_t^{ex}(\mathbf{r}'') d\mathbf{r}'' d\mathbf{r}' \end{aligned} \tag{4.6}$$

Using (C.12) and (4.6), the final expression can be concluded for the antenna potential Green's function G_{AV} as

$$G_{\text{AV}}(\mathbf{r}, \mathbf{r}'') = \frac{-1}{4\pi\epsilon_0 j\omega} \int_l G_{\text{fs}}(\mathbf{r}, \mathbf{r}') \frac{\partial}{\partial \mathbf{r}'} G_{\text{AC}}(\mathbf{r}', \mathbf{r}'') d\mathbf{r}' \tag{4.7}$$

Magnetic Vector Potential Green's function

Using an approach similar to the above, the magnetic vector potential Green's function can be derived. Let $\mathbf{A}(\mathbf{r})$ be the magnetic vector potential which can be expressed as

$$\mathbf{A}(\mathbf{r}) = \frac{\mu_0}{4\pi} \int_l G_{\text{fs}}(\mathbf{r}, \mathbf{r}') \mathbf{J}(\mathbf{r}') d\mathbf{r}' \tag{4.8}$$

Substituting (C.11) into (4.8) yields

$$\mathbf{A}(\mathbf{r}) = \frac{\mu_0}{4\pi} \int_l \int_l G_{\text{fs}}(\mathbf{r}, \mathbf{r}') \mathcal{L}_{r'}^{-1} \delta(\mathbf{r}' - \mathbf{r}'') \mathbf{E}_t^{ex}(\mathbf{r}'') d\mathbf{r}'' d\mathbf{r}' \tag{4.9}$$

Also substituting (C.12) into (4.9), the final expression for the magnetic vector potential Green's function G_{MV} can be stated as

$$G_{\mathrm{MV}}(\mathbf{r}, \mathbf{r}'') = \frac{\mu_0}{4\pi} \int_l G_{\mathrm{fs}}(\mathbf{r}, \mathbf{r}') G_{\mathrm{AC}}(\mathbf{r}', \mathbf{r}'') d\mathbf{r}' \tag{4.10}$$

4.4 Antenna Mode Characteristic Impedance Construction

In this section, the ATN and ETLA approaches are proposed for representing the characteristic impedance of the antenna mode current. The direct relations are derived between the characteristic impedance and the exciting field incident over two perfect conducting wires in free space.

4.4.1 The ATN Approach for Characteristic Impedance

In this part, the general ATN solution is proposed for the characteristic impedance. The Green's functions used throughout this derivation have been derived in Section 4.3 for the antenna potential, the magnetic vector potential and antenna current. The capacitance p.u.l. $C_{\mathrm{d/a}}$ can be defined as [72]

$$C_{\mathrm{d/a}}(\mathbf{r}) = \frac{\rho_{\mathrm{d/a}}(\mathbf{r})}{\phi_{\mathrm{d/a}}(\mathbf{r})} \tag{4.11}$$

where the subscript d/a indicates the differential or antenna mode of excitation. Using (4.2), (4.3), (4.6) and (4.7), (4.11) can be written as

$$C_{\mathrm{d/a}}(\mathbf{r}) = \frac{\int_l G_{\mathrm{CD-d/a}}(\mathbf{r},\mathbf{r}')\mathbf{E}_t^{ex}(\mathbf{r}')d\mathbf{r}'}{\int_l G_{\mathrm{AV-d/a}}(\mathbf{r},\mathbf{r}'')\mathbf{E}_t^{ex}(\mathbf{r}'')d\mathbf{r}''} \tag{4.12}$$

Also, the inductance p.u.l. $L_{\mathrm{d/a}}$ can be defined as [72]

$$L_{\mathrm{d/a}}(\mathbf{r}) = \frac{\mathbf{A}_{\mathrm{d/a}}(\mathbf{r})}{\mathbf{J}_{\mathrm{d/a}}(\mathbf{r})} \tag{4.13}$$

Using (4.9), (4.10), (C.11) and (C.12), (4.13) can be written as

$$L_{\mathrm{d/a}}(\mathbf{r}) = \frac{\int_l G_{\mathrm{MV-d/a}}(\mathbf{r},\mathbf{r}'')\mathbf{E}_t^{ex}(\mathbf{r}'')d\mathbf{r}''}{\int_l G_{\mathrm{AC-d/a}}(\mathbf{r},\mathbf{r}')\mathbf{E}_t^{ex}(\mathbf{r}')d\mathbf{r}'} \tag{4.14}$$

where $G_{\mathrm{CD-d/a}}$, $G_{\mathrm{AV-d/a}}$, $G_{\mathrm{MV-d/a}}$ and $G_{\mathrm{AC-d/a}}$ are precisely defined in Appendix C.

It is worth mentioning that the numerical ATN solution uses the approximated method of moments (MOM) numerical form of equations (4.12) and (4.14), where the boundary condition matrix is represented. The boundary condition matrix is forcing the boundary conditions at the TL terminals. Using matrix operations, the boundary condition matrix is eliminated from the numerator and denominator so that the p.u.l. parameters are independent of the boundary conditions at the TL terminals. The complete proof of the boundary condition matrix elimination is shown in Appendix D.

Equations (4.12) and (4.14) provide a general integral form for the capacitance

and inductance p.u.l., respectively. Since the behavior of the antenna mode characteristic impedance for lossless conductors in free space is the main concern of this work, the characteristic impedance can be defined $Z(\mathbf{r})$ as

$$Z(\mathbf{r}) = \sqrt{\frac{L_{\mathrm{d/a}}(\mathbf{r})}{C_{\mathrm{d/a}}(\mathbf{r})}} \tag{4.15}$$

4.4.2 The ETLA Approach for the Mean Value of the Antenna Mode Characteristic Impedance

Due to the complexity of the ATN approach using the antenna theory, an ETLA approach based on a modified TL approach is presented. Although the first two conditions of the TL theory are still satisfied in the antenna mode current case under consideration, the third condition is not satisfied (*i.e.*, the sum of the currents is not equal to zero). Hence, the ETLA approach adopts an approximation for the TL theory to represent the mean value of the antenna mode characteristic impedance, taking into consideration the frequency of operation and angle of incidence. The ETLA approach evaluates the characteristic impedance using the p.u.l. parameters, which are further expressed in terms of new value $\Psi(\mathbf{r})$, which is defined in Appendix E. $\Psi(\mathbf{r})$ can be defined as

$$\begin{aligned}
&\Psi(\mathbf{r}) = \\
&-0.9.\{j\pi H_0^{(2)}(a\sqrt{k_0^2 - k_1^2}) + j\pi H_0^{(2)}(d\sqrt{k_0^2 - k_1^2})\} \\
&-2\{E_1(j(l - r + a)(k_0 - k_1)) + E_1(j(r + a)(k_0 + k_1))\}
\end{aligned} \tag{4.16}$$

where $H_0^{(2)}(x)$ denotes the Hankel function of the zero-th order and second kind, $E_1(z)$ is the exponential integral function, d is the distance between the two wires of the TL. a is the radius of each wire in the TL and $k_1 = k_0 \cos(\theta)$, where θ is the incidence angle. Hence, the inductance and the capacitance p.u.l. can be expressed as

$$L_a(\mathbf{r}) = \frac{\mu_0 \Psi(\mathbf{r})}{4\pi} \tag{4.17}$$

$$C_a(\mathbf{r}) = \frac{4\pi\epsilon_0}{\Psi(\mathbf{r})} \tag{4.18}$$

where the subscript a refers to the antenna mode of excitation. Substituting (4.17) and (4.18) into (4.15) yields

$$Z(\mathbf{r}) = \frac{\Psi(\mathbf{r})}{4\pi}\sqrt{\frac{\mu_0}{\epsilon_0}} \tag{4.19}$$

The full derivation of the ETLA solution can be found in Appendix E. It can be easily concluded that the characteristic impedance depends mainly on the value of $\Psi(\mathbf{r})$. Here, two important parameters should be referred to that affect $Z(\mathbf{r})$: 1) Frequency; 2) Incidence angle and discuss their relationships in the following:

$Z(\mathbf{r})$ vs. Frequency

As mentioned before, $\Psi(\mathbf{r})$ has been derived on the basis that the wire length is much more than the operating wavelength. Hence, an intuitive conclusion can be deduced from (4.16), that $\Psi(\mathbf{r})$ decreases as the frequency increases. This is due to the fact that when the frequency increases, the wavelength decreases and

both k_0 and k_1 increase, and hence, both the Hankel functions and the exponential integral functions decrease.

$Z(\mathbf{r})$ vs. Incidence Angle

Incidence angle has inverse relationship with the value of k_1. Consequently, as the incidence angle increases, $k_0 - k_1$ increases while $k_0 + k_1$ decreases. This leads to the decrease of $H_0^{(2)}(a\sqrt{k_0^2 - k_1^2})$, $H_0^{(2)}(d\sqrt{k_0^2 - k_1^2})$ and $E_1(j(l-r+a)(k_0-k_1))$ and the increase of $E_1(j(r+a)(k_0+k_1))$. Hence, the variation of the incident angle does not yield a significant variation of the characteristic impedance mean value.

4.5 Simulation Results

In (4.15) and (4.19), the ATN and ETLA solutions have been proposed for the antenna mode characteristic impedance. In this section, their performance is presented by simulation, in comparison to the classical TL solution in [45]. The formulae presented in [45] is used for the inductance and the capacitance p.u.l. of the antenna mode current to derive the TL antenna mode characteristic impedance. Also, a performance comparison is presented between the proposed solutions and the FWTL solution, which was proposed in [56] to derive the differential mode current and its characteristic parameter matrix. However, in the simulations the FWTL solution is used in order to derive the antenna mode characteristic impedance, where the relation between the characteristic impedance and the characteristic parameter matrix is defined according to [73].

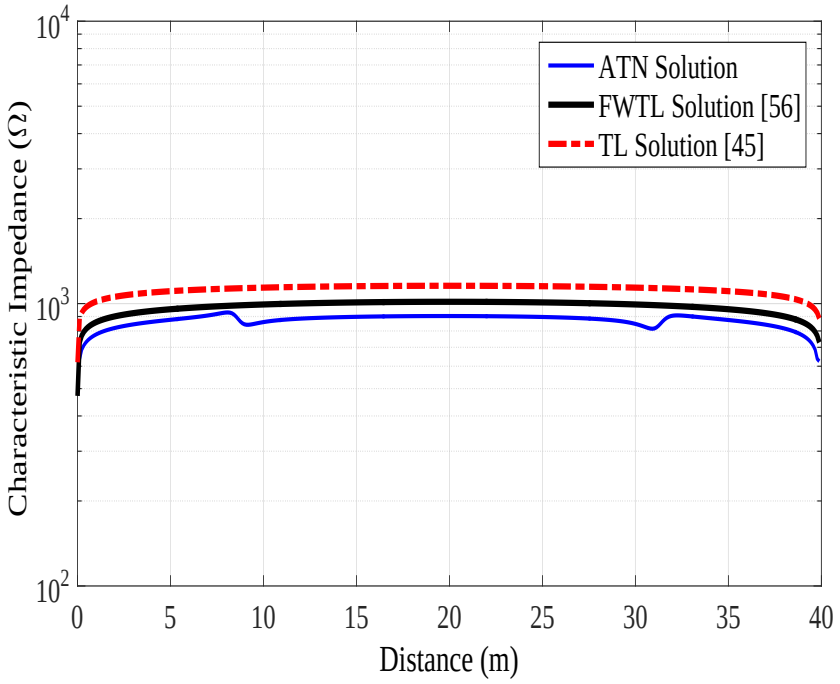

FIGURE 4.3: Characteristic impedance at frequency 2 MHz and $\theta = 30°$.

4.5.1 Characteristic Impedance vs. Frequency

In Fig. 4.3, the characteristic impedance is shown using the ATN solution for the antenna mode of excitation at frequency of 2 MHz and angle of incidence $\theta = 30°$. The wavelength of operation is 150 m which is much more than the wire length. It can be observed that both the ATN solution and the FWTL solution converge to the TL solution in [45] at low frequency of 2 MHz, proving the validity of the proposed solution. Also, it can be easily observed that the difference between the ATN and the TL solutions approaches 157 Ω. This is due to the difference between the ATN procedure and the TL approximation adopted in [45], where the ATN numerical approach gives the exact solution for the characteristic impedance and the TL approach gives an approximated value. A notable remark, which should be taken into consideration that the antenna mode Green's function in equation (C.13) is not fast decaying as the differential mode one, which increases

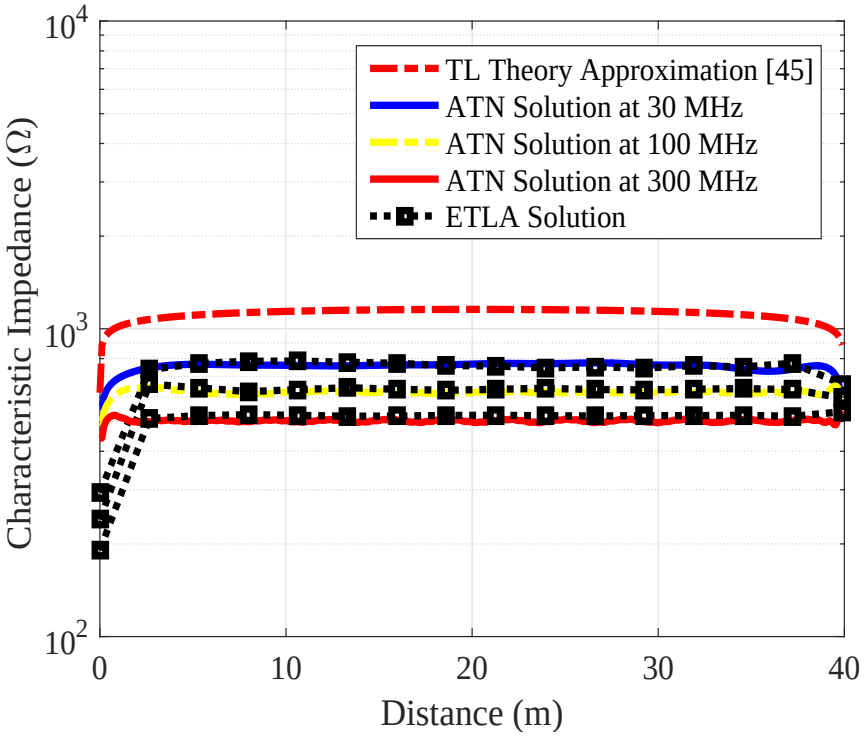

FIGURE 4.4: Characteristic impedance vs. distance along the wire length at incident angle $\theta = 45°$.

the approximation error in the TL approach. This makes the difference between the proposed solution and that in [45] easily justified.

In Fig. 4.4, the characteristic impedance is shown versus the distance along the wire. The performance of the ATN solution is compared at different frequencies of 30, 100 and 300 MHz (the corresponding wavelengths are all shorter than the wire length) to the performance of the TL solution in [45]. It can be observed the effect of the frequency on changing the mean value of the characteristic impedance.

In Fig. 4.5, the characteristic impedance versus frequency is shown at a fixed position of 30 meters from the origin and at an angle of incidence of $\theta = 45°$. The characteristic impedance obtained from ATN, FWTL and ETLA solutions decreases with the increase in the frequency, while the TL solution [45] presents a frequency-independent characteristic impedance. This verifies the analysis in

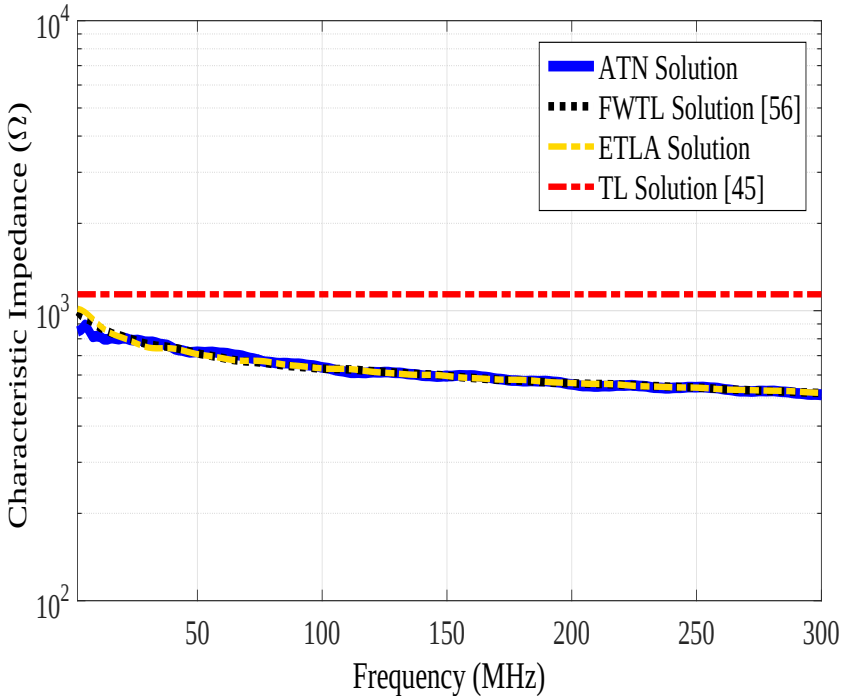

FIGURE 4.5: Characteristic impedance vs. frequency at a distance 30 m from the origin and $\theta = 45°$.

Subsection 4.4.2.

In Fig. 4.6, the characteristic impedance of the antenna mode current is shown versus the frequency of different geometric structures for the two straight wires in free space. In the simulations, three geometric structures with different values of wire length (l), radius (a) and separation distance (d) have been considered. The three geometric structures 1, 2 and 3 have the geometric parameter combination (l, a, d) as: (40, 1.5×10^{-3}, 4.5×10^{-3}) m, (60, 2×10^{-3}, 1.8×10^{-3}) m and (80, 3×10^{-2}, 8.1×10^{-2}) m. It can be observed that for different geometric structures, the antenna mode characteristic impedance still decreases with the frequency increase. This proves that in the VHF band (more specifically when the $\lambda < l$, where λ is the exciting wavelength) the antenna mode characteristic impedance decreases with the increase in the frequency regardless of the geometric

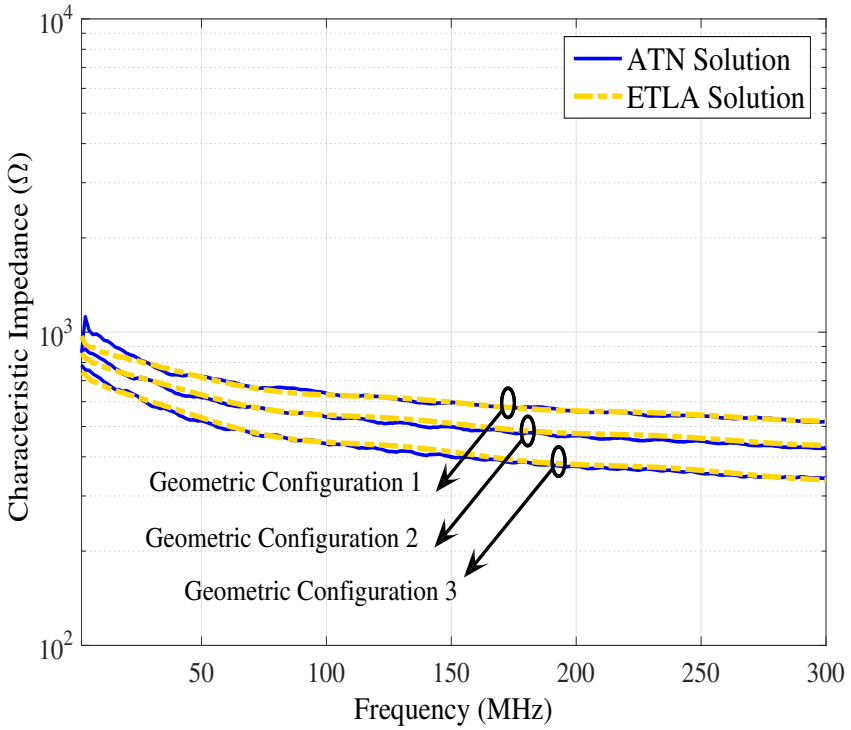

FIGURE 4.6: Characteristic impedance vs. frequency for different geometric structures.

structure.

4.5.2 Characteristic Impedance vs. Incidence Angle

The effect of the incident angle on the mean value of the characteristic impedance is smaller than that of the frequency. This is demonstrated in Fig. 4.7. The simulation results show that the angle of incidence has a smaller effect on the mean value of the characteristic impedance compared to the effect of the exciting frequency. This agrees with the analysis in Section 4.4.2. In Fig. 4.7, the difference between the simulation results obtained using the proposed solutions and the TL solution [45] is due to the fact that the simulation is done at 100 MHz. As mentioned before, the TL solution is not applicable to high frequency.

In Fig. 4.8, the characteristic impedance of the antenna mode current is shown

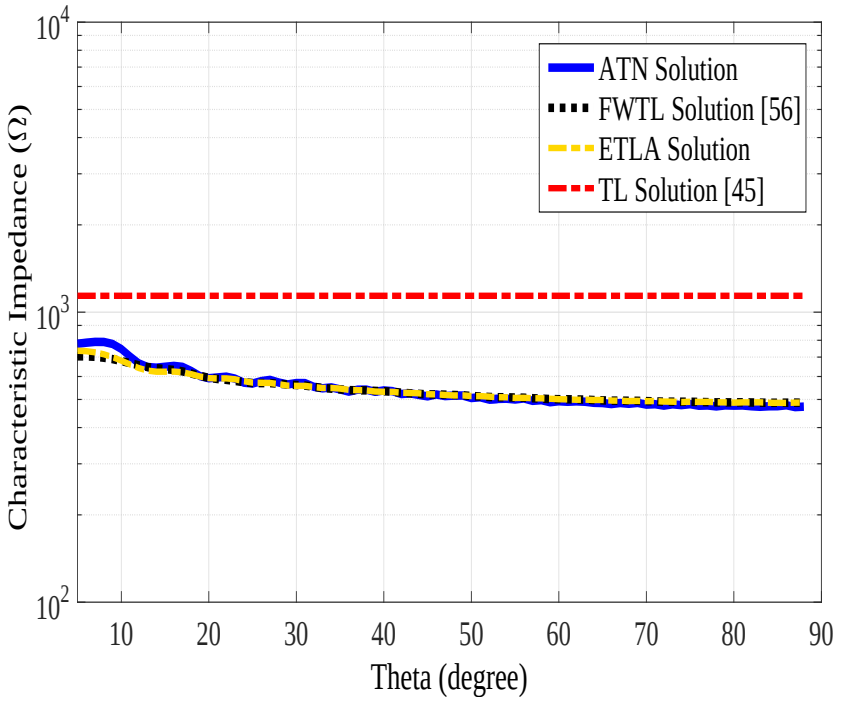

FIGURE 4.7: Characteristic impedance vs. angle of incidence θ at a distance 30 m from the origin and frequency 100 MHz.

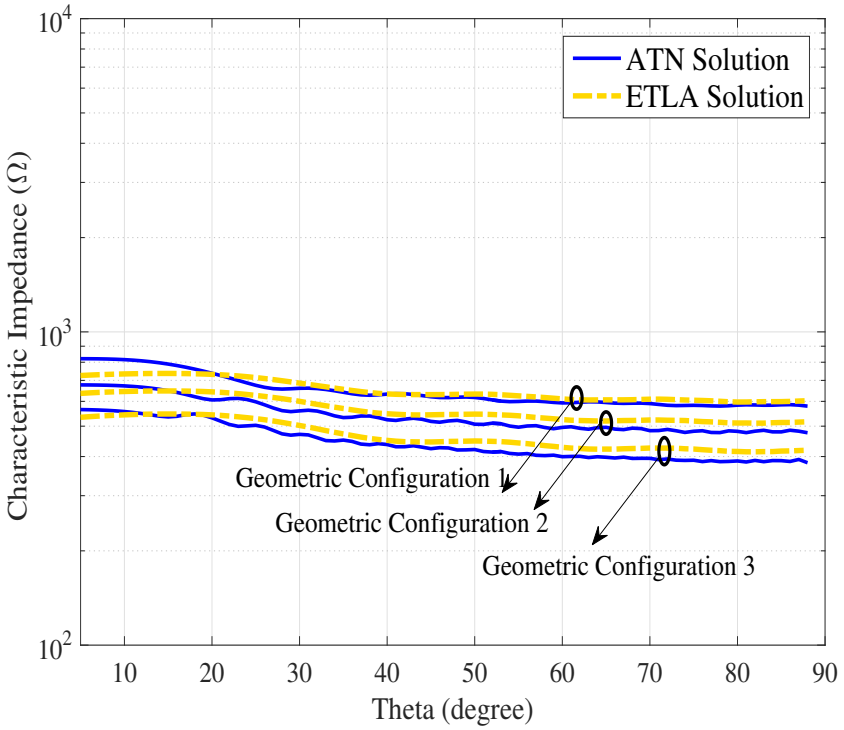

FIGURE 4.8: Characteristic impedance vs. angle of incidence θ for different geometric structures.

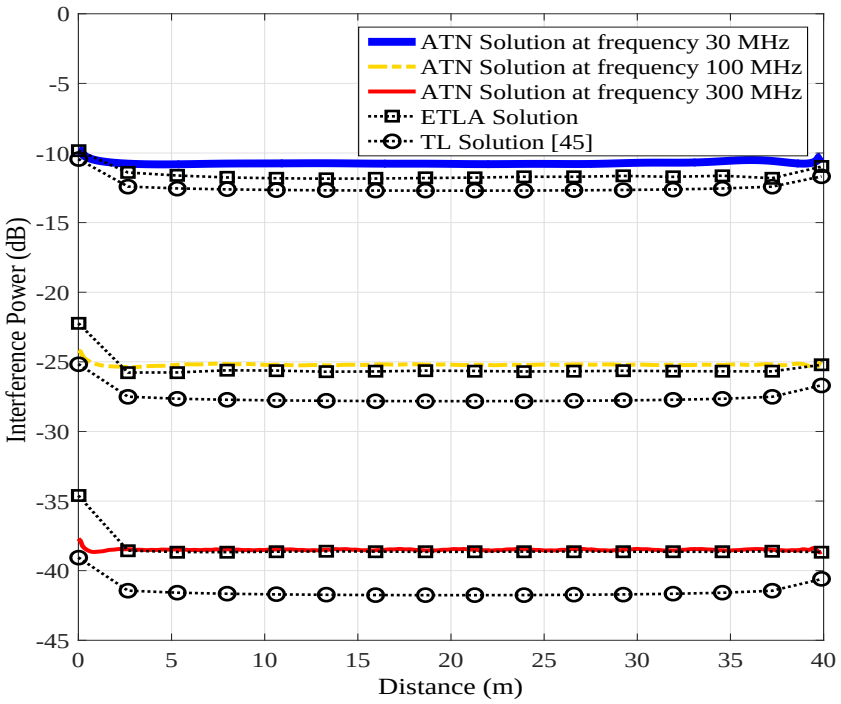

FIGURE 4.9: Interference power vs. distance at different frequencies for incidence angle $\theta = 45°$.

versus the incident angle for different geometric structures. The simulation results show that the geometric structure does not affect the performance of the antenna mode characteristic impedance towards the change in the incident angle.

4.5.3 Antenna Mode Interference to Differential Mode Signal

The antenna mode current can convert to differential mode by mode conversion mechanisms [55][74][75]. The adopted mode conversion mechanism is discussed in Appendix B. In Figs. 4.9 and 4.10, the calculation of the converted interference signal from antenna mode to differential mode is presented at different frequencies. In Fig. 4.9, the interference power is calculated for different EMI filter locations

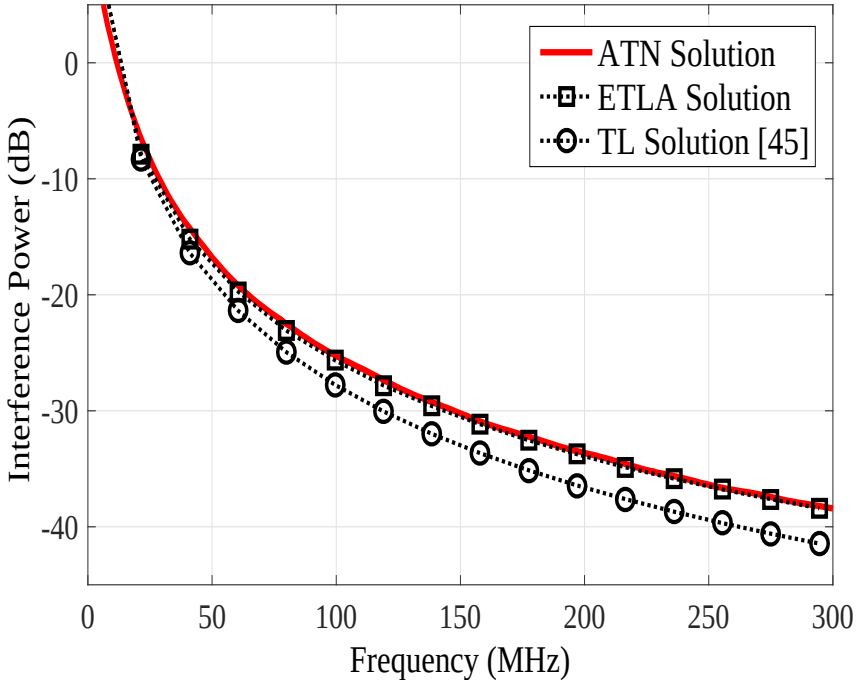

FIGURE 4.10: Interference power vs. frequency at incident angle $\theta = 45°$.

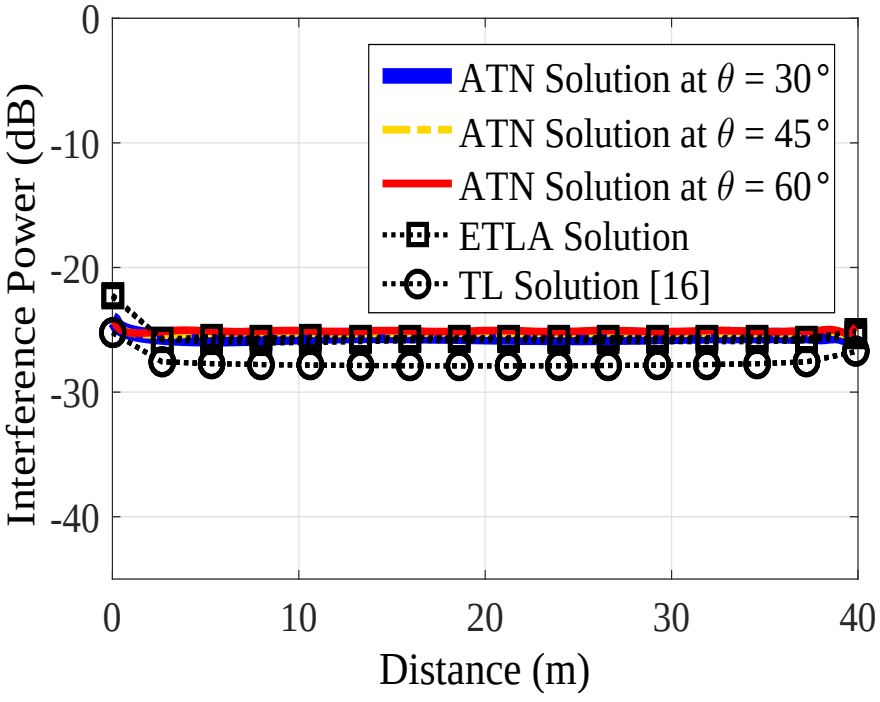

FIGURE 4.11: Interference power vs. distance at different incident angles for frequency of 100 MHz.

across the TL, where the distance is measured from the origin to the location of the EMI filter. The interference power reduces with the increase of frequency, but is relatively stable at different distances. It can be observed that the proposed solutions yield a higher calculated interference power at different frequencies than that in [45]. The difference between the ETLA approach and the TL approach in [45] reaches more than 4 dB at 300 MHz, which means more than double the interference power. This is because the proposed solution has lower antenna mode characteristic impedance than that proposed in [45].

In Fig. 4.11, the interference power at different incident angles for the same frequency of operation is shown. It can be observed that the interference mean value is not much affected by the incident angle.

Discussion on the ETLA approximation

The assumption of the antenna mode current in (E.4) does not consider two other components of the current which represent the travelling and reflected currents at the TL terminals as discussed in [48]. This is due to the small effect of those current components on the value of the antenna mode characteristic impedance in the VHF band. This small effect can be concluded from the small difference of the ETLA solution compared to both the ATN and FWTL solutions in the simulation results shown in Figs. 4.3-4.8.

4.6 Summary

The antenna mode interference to the differential mode signal has a great influence on the wireless interference to BPLC in the VHF band. In this Chapter, two solutions (ATN and ETLA) for representing the characteristic impedance of the excited antenna mode current in the VHF band have been proposed. The ATN solution has been shown to be dependent on the exciting frequency and incidence angle, unlike the TL solution in [45] which is independent of the two parameters. Also, the ATN solution matches the FWTL solution in [56], while directly deriving the impedance without the need to derive the current as the FWTL solution. Furthermore, the ETLA solution shows a negligible difference from the ATN and FWTL solutions, while requiring a lower computational complexity. The proposed solutions show a higher interference power across a TL terminated by EMI filter than the TL solution in [45]. This will help in providing a more accurate estimation of the power of the antenna mode interference to the differential mode signal. In Chapter 5, the hybrid TVWS BPLC point-to-point system will be proposed based on the channel investigations, which had been done in Chapters 3 and 4. The problem of maximising the ergodic capacity, while avoiding the interference with other TV services will be investigated.

Chapter 5

MIMO White BPLC Point-to-Point System

5.1 Introduction

In the previous two Chapters, both the BPLC and TVWS channels were studied thoroughly. A comparison was held in Chapter 3 between the path losses of both channels, and the convergence between them was shown. This proved the feasibility of having cooperative system between the TVWS and BPLC. Also, measurements carried out in Chapter 3 and the theoretical analysis presented in Chapter 4 had investigated the crosstalk between both channels, which could be exploited in enhancing the received signal in an MIMO cooperative system. In this Chapter, a new cooperative system is proposed between BPLC and TVWS in the VHF band 54 MHz - 88 MHz referred to as white BPLC (WPLC). The proposed system is different from the previous MIMO cognitive BPLC system in [17] since the WBPLC Tx can access the VHF band with lower Tx PSD constraints using

the TVWS standard [9], which enhances significantly the overall system capacity. It is worth mentioning that, to the best of our knowledge, this is the first work to propose a cognitive BPLC solution that complies with the TVWS standard. The addition of wireless antenna to cognitive BPLC is essential to enable the WBPLC Tx to sense the TV PU at very low power level of -114 dBm, which satisfies the requirement of the TVWS standard [9]. This addition of the TVWS antenna solves the problem of coupling loss that exists in the aforementioned cognitive BPLC solutions in Chapter 2. Second, the interference to other wireless services is mitigated using a proposed iterative precoding technique at the Tx. The proposed algorithm takes the advantage of the multiple-input single-output (MISO) channel between the WBPLC Tx and the TV wireless Rx. Third, an efficient power allocation algorithm is derived for the MIMO system in order to achieve maximum ergodic capacity for each subcarrier. Fourth, compared to the hybrid BPLC WiFi system [18], the proposed system offers a more cost-effective hybrid solution. This is due to the elimination of the RF up- and down-converters needed for the WiFi transceiver.

The Chapter is organised as follows. In Section 5.2, the proposed system model is presented. In Section 5.3, cognitive spectrum access is addressed, including an iterative precoding technique and MIMO spectrum sensing. In Section 5.4, the power allocation for the MIMO channel is presented. In Section 5.5, the capacity simulation results of the proposed system are compared with BPLC WiFi and MIMO BPLC. Finally, in Section 5.6 the Chapter is summarised.

Notations: $\mathbb{E}\{.\}$ denotes the expectation operator, $\lceil x \rceil^+$ denotes $\max(0, x)$, vectors are represented by boldface letters and the Hermitian of a matrix $\mathbf{A}$ is $\mathbf{A}^\dagger$,

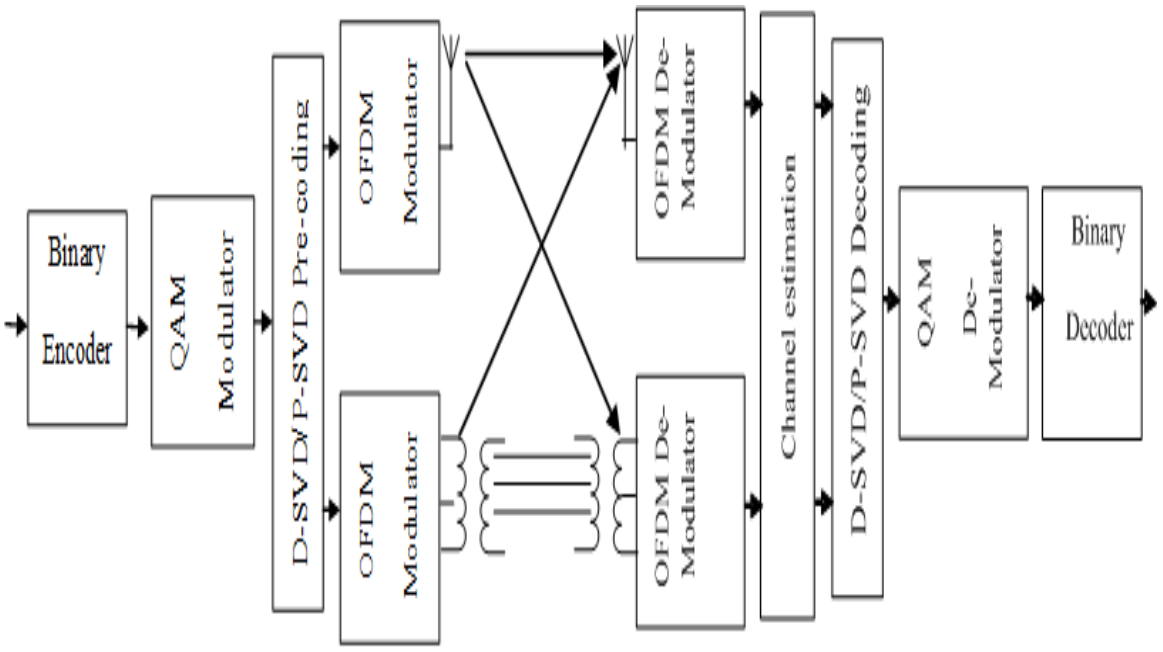

FIGURE 5.1: System Model of WBPLC transceiver, using both BPLC and wireless TVWS channels

and the conjugate transpose of a vector $\mathbf{v}$ is $\mathbf{v}^{\dagger}$. $\mathbf{I}$ denotes the identity matrix.

5.2 System Model

The proposed WBPLC system model is illustrated in Fig. 5.1. The TV PU activity (*i.e.*, presence or absence) in the TVWS band is assumed to be known at the WBPLC Tx due to access to a geolocation database as stated in [9]. In this Chapter, two modes of operation are proposed for the TVWS BPLC system according to the available channel state information (CSI). The CSI of the PU Rx in this work is defined as the interference complex channel gain vector $\mathbf{g}$ between the WBPLC Tx and the PU Rx. The two proposed modes are: 1) Opportunistic Mode: The CSI of the PU Rx is available to the WBPLC transceiver; 2) Non Opportunistic Mode: The CSI of the PU Rx is unavailable to the WBPLC

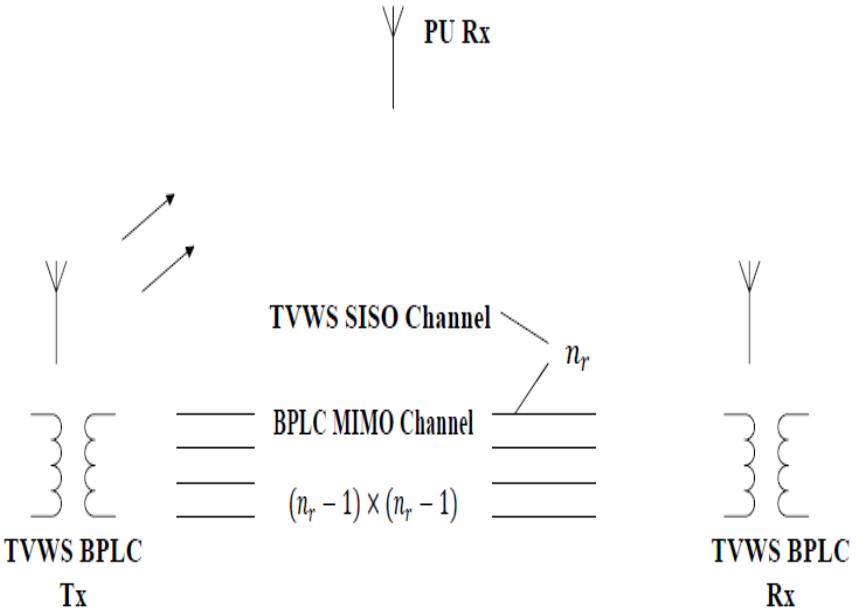

FIGURE 5.2: $n_r \times n_r$ WBPLC Tx-Rx channel model and $n_r \times 1$ WBPLC Tx-TV PU Rx channel model

transceiver. The CSI in the opportunistic mode can be obtained using the sensing method in [76]. The method simply assumes that the SU joins the PU network in the first time slot, and does not send any signal. Let x_i and η_i represent the transmitted signal and the channel gain between the PU Tx and Rx at i-th time slot, respectively. Hence, the received message by the PU Rx is:

$$y_i = \eta_i x_i + z_i \tag{5.1}$$

The PU Rx broadcasts a message containing the estimation of the channel gain $\hat{\eta}_i \approx \eta_i$, which is received by the SU Rx. In the second time slot, the PU message is received and decoded by the SU and forwarded again with power α. Let g represents the channel gain between the SU Tx and the PU Rx. Hence, the

received message by the PU is

$$y_i = (\eta_{i+1} + g_{i+1}\alpha)x_{i+1} + z_{i+1} \tag{5.2}$$

The PU again broadcasts the estimation of the new channel gain $\hat{\eta}_{i+1} \approx \eta_{i+1} + g_{i+1}\alpha$, which is received by the SU. Now, the SU can estimate the channel gain g_{i+1} using $\hat{\eta}_i$ and $\hat{\eta}_{i+1}$. Obtaining the CSI between the WBPLC Tx and the PU Rx using the method in [76] relies on the permission of the PU network given to the SU in order to listen and add small interference noise power (α) to the PU communication. The advantage of this method is that it does not add any overhead communication to the PU (*i.e.*, signaling between the PU and the SU). However, if this method is not allowed by the PU, then a switch to the non-opportunistic mode of operation can be done, which does not need obtaining the CSI between the WBPLC Tx and the PU Rx.

As illustrated in Fig. 5.1, the binary encoded data is modulated using quadrature amplitude modulation (QAM) modulator. Each QAM symbol is precoded using either singular value decomposition (SVD) algorithm or projected singular value decomposition (P-SVD) algorithm. The precoding algorithm is discussed in detail in Section 5.3. The frame structure follows the IEEE 1901 [16], which contains two parts: the frame control part and the payload part. The former is sent over a separate control channel in the non-cognitive frequency band below 30 MHz, while the latter is sent over the WBPLC cognitive channel with variable length according to the available time slots. The received signal is decoded using a decoding matrix according to the precoding type. The decoded symbols are

passed through a maximum likelihood (ML) detector to allow estimation of the transmitted symbols.

Since the proposed system accesses the TVWS, a cognitive spectrum access algorithm is proposed. In the algorithm the channel between a single WBPLC Tx and Rx is considered to be $n_r \times n_r$ MIMO channel where n_r is the number of WBPLC MIMO sub-channels as illustrated in Fig. 5.2. The n_r MIMO sub-channels are divided into two groups: 1) $(n_r-1)\times(n_r-1)$ MIMO BPLC sub-channels as in the case of 2×2 single phase MIMO BPLC and 3×3 three phase MIMO BPLC; 2) single-input single-output (SISO) TVWS wireless sub-channel. However, the channel between a WBPLC Tx and a single TV PU Rx can be considered as $n_r \times 1$ MISO channel. This advantage is used by the proposed system for better WBPLC to TV PU interference mitigation. The signal received at the WBPLC Rx on subcarrier n can be represented as [77]

$$\mathbf{y}(n) = \tilde{\mathbf{H}}^{(n)}\mathbf{U}^{(n)}\mathbf{x}(n) + \mathbf{E}^{(n)}\mathbf{U}^{(n)}\mathbf{x}(n) + \mathbf{z}(n) \tag{5.3}$$

where $\tilde{\mathbf{H}}^{(n)}$ is the estimated $n_r \times n_r$ MIMO channel matrix for subcarrier n, which can be expressed as $\tilde{\mathbf{H}}^{(n)} = \mathbf{Q}^{(n)}(\mathbf{\Lambda}^{(n)})^{1/2}\mathbf{U}^{\dagger(n)}$. $\mathbf{E}^{(n)} = \mathbf{Q}^{(n)}\tilde{\mathbf{E}}^{(n)}\mathbf{U}^{\dagger(n)}$ is a zero mean Gaussian distributed error matrix with the variance σ_E^2, which represents the error introduced in the channel estimation as previously addressed in [78][79][80], it is assumed that the channel transfer matrix $\mathbf{H}^{(n)} = \tilde{\mathbf{H}}^{(n)} + \mathbf{E}^{(n)}$. $\mathbf{U}^{(n)}$ is the precoding matrix for subcarrier n and $\mathbf{z}(n)$ is AGWN vector whose elements have zero mean and variance σ_z^2.

Without loss of generality, the antenna is assumed to be omnidirectional with

unity gain [81], the directional antenna can further improve the performance by introducing more antenna gain. In order to have more compact VHF antennas for practical applications, several researches had been done in [82] and [83] to design small VHF antennas (*i.e.*, ≤ 0.65 m. length). This can be exploited in the WBPLC system for more practical design and implementation.

Multiplying the received signal by the decoding matrix $\mathbf{Q}^{\dagger(n)}$. It can be deduced

$$\hat{\mathbf{y}}(n) = (\mathbf{\Lambda}^{(n)})^{1/2}\mathbf{x}(n) + \tilde{\mathbf{E}}^{(n)}\mathbf{x}(n) + \hat{\mathbf{z}}(n) \tag{5.4}$$

where $\hat{\mathbf{z}}(n) = \mathbf{Q}^{(n)}\mathbf{z}(n)$ and $\mathbf{\Lambda}^{(n)}$ is the matrix of the singular values of the MIMO channel power gain matrix $\mathbf{S}$ which can be defined as $\mathbf{S} = \tilde{\mathbf{H}}^{(n)}\tilde{\mathbf{H}}^{\dagger(n)}$.

5.3 Cognitive Spectrum Access

In this section, the cognitive spectrum access for the hybrid WBPLC Tx is presented, including: 1) An iterative precoding technique; 2) Cognitive spectrum sensing.

5.3.1 Iterative Hybrid SVD/P-SVD Precoding Technique

In this work, a new precoding algorithm is proposed for cognitive spectrum access. The algorithm aims to achieve maximum capacity while maintaining the interference limit at the TV PUs Rxs by applying Lemma 1 that will be discussed later in this Section. The algorithm precodes the WBPLC Tx data according to the WBPLC-TV PU channel. Two precoding algorithms are used: 1) SVD; 2)

P-SVD [84]. The SVD is used in the idle channel case while a hybrid SVD/P-SVD is used in case of occupied channel. In case of SVD precoding, the channel matrix $\mathbf{H}^{(n)}$ is decomposed using SVD into $\mathbf{H}^{(n)} = \mathbf{Q}^{(n)}(\mathbf{\Lambda}^{(n)})^{1/2}\mathbf{U}^{\dagger(n)}$ where $\mathbf{Q}^{(n)}$ and $\mathbf{U}^{(n)}$ are $n_r \times n_r$ matrices with orthonormal columns. $\mathbf{\Lambda}^n$ is an $n_r \times n_r$ diagonal positive matrix with vector $\lambda^{(n)}$ as its diagonal. Hence, $\mathbf{V} = \mathbf{U}^{(n)}$ will be the precoding matrix as shown in (H.2). However, in the P-SVD precoding, the SU MIMO channel is first projected on to the null space of the interference channel vector with the PU. Then, the projected channel matrix is then decomposed using the SVD method. Let $\hat{\mathbf{g}_1}^{(n)} = \mathbf{g}_1^{(n)}/\|\mathbf{g}_1^{(n)}\|$ be the unit vector in the direction of $\mathbf{g}_1^{(n)}$ which represents the channel vector between the WBPLC and the TV PUs. The subscript 1/0 in $g_{1/0}^{(n)}$ indicates the TV PU presence/absence, respectively. The projection of the channel matrix $\mathbf{H}^{(n)}$ can be defined in the null space of $\mathbf{g}_1^{\dagger(n)}$ as [84]

$$\mathbf{H}_{\perp}^{(n)} = \mathbf{H}^{(n)}(\mathbf{I} - \hat{\mathbf{g}_1}^{(n)}\hat{\mathbf{g}_1}^{\dagger(n)}) \tag{5.5}$$

The vector multiplication of $\hat{\mathbf{g}_1}^{(n)}\hat{\mathbf{g}_1}^{\dagger(n)}$ results in a matrix such that $(\hat{\mathbf{g}_1}^{(n)}\hat{\mathbf{g}_1}^{\dagger(n)})\hat{\mathbf{g}_1}^{(n)} = \hat{\mathbf{g}_1}^{(n)}$. Hence, $(\mathbf{I} - \hat{\mathbf{g}_1}^{(n)}\hat{\mathbf{g}_1}^{\dagger(n)})\hat{\mathbf{g}_1}^{(n)}$ is equal to zero. Consequently, $\mathbf{H}_{\perp}^{(n)}$ represents the projection of $\mathbf{H}^{(n)}$ matrix into the null space of $\hat{\mathbf{g}_1}^{\dagger(n)}$). Then using the SVD of $\mathbf{H}_{\perp}^{(n)} = \mathbf{Q}_{\perp}^{(n)}(\mathbf{\Lambda}_{\perp}^{(n)})^{1/2}\mathbf{U}_{\perp}^{\dagger(n)}$ the precoding matrix can be concluded $\mathbf{V} = \mathbf{U}_{\perp}^{(n)}$ and decode the received signal by multiplying by $\mathbf{Q}_{\perp}^{\dagger(n)}$.

$$\hat{\mathbf{y}}(n) = (\mathbf{\Lambda}_{\perp}^{(n)})^{1/2}\mathbf{x}(n) + \hat{\mathbf{z}}(n) \tag{5.6}$$

In the proposed precoding algorithm, both SVD and P-SVD are used jointly according to the CSI of both the WBPLC and TV PU Rxs.

Idle Channel

In case of an idle channel, SVD is used as precoding scheme. Although the PU is absent, an interference limit is forced for false detection probability to avoid harmful interference. The WBPLC-TV PU channel $\mathbf{g}_{0,k}^{(n)}$ with maximum gain $\max_{n_t} \|\mathbf{g}_{0,k}^{(n)}\mathbf{U}_0^{(n)}\|^2$ can only be accessed with power level below the interference limit where $k = 1, 2, ..n_t$ and n_t is the number of PUs.

Occupied Channel

This case is only applied to the opportunistic mode of operation mentioned in Section 5.2. In this case, the PU is present, while the secondary user is allowed also to access the channel such that the received power at the TV PU Rx is below a certain interference limit Γ. In the proposed algorithm the SVD is also used as a default precoding scheme as in the case of the idle channel. However, the decision is taken to switch the precoding scheme to P-SVD according to the CSI of the TV PU Rx. The decision is taken to satisfy two conditions: 1) Achieve the interference limit at the TV PU Rx; 2) Achieve high signal to noise ratio (SNR) at the WBPLC Rx. Hence, the previous two conditions can be satisfied knowing the CSI as follows. Let's assume that the interference limit is the minimum threshold for the signal to be detected by the Rx. Hence, the interference to the PU should be below this threshold in order not to affect the PU reception, while the signal received at the WBPLC Rx should be above that threshold in order to be detected.

Lemma 1. Let γ be the SNR at the WBPLC Rx and Γ be the interference limit at the TV PU Rx. In order to achieve $\gamma \geq \Gamma$ while satisfying the interference limit at the TV PU Rx, the following condition should be satisfied

$$\det \begin{bmatrix} \frac{\lambda_1^{(n)}}{\rho} - \alpha_{1,k}^{(n)} & \dots & -\alpha_{n_r,k}^{(n)} \\ \vdots & & \vdots \\ -\alpha_{1,k}^{(n)} & \dots & \frac{\lambda_{nr}^{(n)}}{\rho} - \alpha_{n_r,k}^{(n)} \end{bmatrix} \geq 0 \tag{5.7}$$

where the matrix diagonal is positive such that $\frac{\lambda^{(n)}}{\rho} \geq {\alpha_{\mathbf{k}}}^{(n)}$, ρ is a constant that satisfies $\rho \geq 1$ and $\alpha_k = \|\mathbf{g}_{1,k}^{(n)}\mathbf{U}_1^{(n)}\|^2$ of the k-th PU. Lemma 1 implies that the WBPLC MIMO channel gain represented by its singular values $\lambda^{(n)}$ should be greater than gain of the interference channel with the PU represented by α_k. The ρ constant controls the gap between both channel gains.

Proof. See Appendix F. □

Lemma 1 should be satisfied for the use of SVD. If this condition is violated, then P-SVD is used to eliminate the interference at one TV PU Rx. The eliminated PU is selected to satisfy $\max_{n_t}\{\|{\alpha_{\mathbf{k}}}^{(n)}\|^2\}$. Hence, the algorithm proposed for cognitive access can be summarised as

Proposed iterative hybrid SVD/P-SVD algorithm

- Initialise the precoding algorithm as SVD and $i = n_r$.
- While $i > 0$

  Check the condition in Lemma 1.

  - If the condition is satisfied, end the loop, otherwise change the precoding to P-SVD.
  - Select the WBPLC-TV PU interference channel to be cancelled that satisfies $\max_{n_t}\{\|\alpha_{\mathbf{k}}{}^{(n)}\|\}$.
  - $i = i - 1$
- End.

5.3.2 Cognitive Spectrum Sensing

It is known that the sensing time is considered as a challenging issue for the cognitive systems. In the proposed system the optimum sensing time for an MIMO cognitive system is achieved through achieving the optimum detection probability for each MIMO sub-channel. This can be clarified in the following Lemma 2. Let $\hat{\mathcal{P}}_d$ represent the target detection probability of the MIMO cognitive Rx using the energy detection method. Also, let the OR rule (*i.e.*, the channel is detected occupied if the PU is detected using either the BPLC Rx or the TVWS Rx) be adopted for MIMO cognitive sensing. Hence, the relationship between the

detection probability of each sub-channel and the target detection probability of the MIMO channel can be expressed as

Lemma 2.

$$\begin{aligned}&\Pi_{i=1}^{n_r}\Big(1-Q\Big[\frac{\gamma_m-\gamma_i}{\gamma_m\sqrt{2\gamma_i+1}}Q^{-1}(\hat{\mathcal{P}}_{fa})\\&+Q^{-1}(\mathcal{P}_{d_m})\sqrt{\frac{2\gamma_m+1}{2\gamma_i+1}}\Big]\Big)=1-\hat{\mathcal{P}}_d\end{aligned}\tag{5.8}$$

where $\mathcal{P}_{d_m}$ is the detection probability of the m-th MIMO sub-channel, γ_m and γ_i are the SNR of the m-th and i-th sub-channels, respectively for $i, m = 1, ..n_r$, $\hat{\mathcal{P}}_{fa}$ is the target false alarm of each MIMO sub-channel and $Q(.)$ is the complementary error function.

Proof. See Appendix G. □

Using Lemma 2, $\mathcal{P}_{d_m}$ can be derived numerically for any MIMO sub-channel. Let $N_{min} = \tau_{min} f_s$ be the minimum number of samples requested to achieve the target detection probability $\hat{P}_d$, f_s is the sampling frequency and τ_{min} is the minimum sensing time. N_{min} can be expressed as [85]

$$N_{min} = \frac{1}{\gamma_m^2}\Big(Q^{-1}(\mathcal{P}_{fa_m}) - Q^{-1}(\mathcal{P}_{d_m})\sqrt{2\gamma_m+1}\Big)^2 \tag{5.9}$$

N_{min} and τ_{min} can be directly evaluated after obtaining $\mathcal{P}_{d_m}$ numerically using Lemma 2.

5.4 Capacity Maximisation based Power Allocation

In this section, the capacity model and the power allocation algorithm are presented, that have been adopted to represent the MIMO WBPLC channel.

5.4.1 Capacity Analysis

In [86], a system model was proposed for the cognitive spectrum access, where the secondary user could access the cognitive band with two power levels $P_0^{(n)}$ and $P_1^{(n)}$ in the TV PU absence and presence, respectively. In this work, the model proposed in [86] is developed to represent the MIMO channel between WBPLC Tx and Rx. Also, the model is modified to represent the MISO interference channel between WBPLC and TV PU. Hence, the spectral efficiencies (SEs) on the n-th subcarrier for the four scenarios are given as

$$r_{c,d}^{(n)} = \frac{1}{N}\Sigma_{i=1}^{n_r} \log_2 \left(1 + \frac{\lambda_{d,i}^{(n)} P_{d,i}^{(n)}}{\sigma_z^2 + \sigma_E^2 P_{av}^{(n)} + d\sigma_p^2}\right) \tag{5.10}$$

where c and d can take the values of 0 and 1 for the idle and occupied channel status, respectively. σ_z^2 and σ_p^2 are the noise power and the PU power, respectively. σ_E^2 is the variance of the channel estimation error $\mathbf{E}^{(n)}$ and $P_{av}^{(n)}$ is the maximum average power allowed for the WBPLC Tx for subcarrier n. $\lambda_{d,i}^{(n)}$ and $P_{d,i}^{(n)}$ are the singular value and the WBPLC Tx signal power of the i-th MIMO sub-channel and n-th subcarrier assigned to each detected channel status d.

Hence, the MIMO ergodic SE can be concluded as

$$R^{(n)} = \frac{\Pi_{I0}}{N}\Big(\frac{T-\tau}{T}\Big)\mathbb{E}_{\mathbf{H}^{(n)},\mathbf{g}^{(n)}}\Big\{\mathcal{P}(H_0)(1-\mathcal{P}_{fa})r_{00}^{(n)} + \mathcal{P}(H_0)\mathcal{P}_{fa}r_{01}^{(n)} + \mathcal{P}(H_1)(1-\mathcal{P}_d)r_{10}^{(n)} + \mathcal{P}(H_1)\mathcal{P}_d r_{11}^{(n)}\Big\} \tag{5.11}$$

Hence, the overall capacity in (bits per seconds) for all the subcarriers can be expressed as

$$C = \frac{B\Pi_{I0}}{N}\Big(\frac{T-\tau}{T}\Big)\Sigma_{n=1}^{N}\mathbb{E}_{\mathbf{H}^{(n)},\mathbf{g}^{(n)}}\Big\{\mathcal{P}(H_0)(1-\mathcal{P}_{fa})r_{00}^{(n)} + \mathcal{P}(\mathcal{H}_0)\mathcal{P}_{fa}r_{01}^{(n)} + \mathcal{P}(\mathcal{H}_1)(1-\mathcal{P}_d)r_{10}^{(n)} + \mathcal{P}(\mathcal{H}_1)\mathcal{P}_d r_{11}^{(n)}\Big\} \tag{5.12}$$

where $\mathcal{P}(\mathcal{H}_0)$ and $\mathcal{P}(\mathcal{H}_1)$ are the probabilities of TV PU absence and presence, respectively. $\mathcal{P}_d$ and $\mathcal{P}_{fa}$ are the TV PU detection probability and false alarm probability, respectively. T is the symbol time duration and τ is the TV PU detection time duration. Π_{I0} is the steady-state probability of the non-burst impulsive state $I0$ of the BPLC channel [70]. It is worth mentioning that due to low occurrence probability of impulsive bursts, Π_{I0} can take values which are close to one [70]. B is the total channel bandwidth of the OFDM symbol and N is the total number of subcarriers. For a constrained power communication system, the average MIMO power of the WBPLC per subcarrier should be less than a pre-defined value P_{av} as

$$\mathbb{E}_{\mathbf{H}^{(n)},\mathbf{g}^{(n)}}\{\mathcal{P}(\mathcal{H}_0)(1-\mathcal{P}_{fa})\Sigma_{i=1}^{n_r}P_{0,i}^{(n)} + \mathcal{P}(\mathcal{H}_0)\mathcal{P}_{fa}\Sigma_{i=1}^{n_r}P_{1,i}^{(n)} + \mathcal{P}(\mathcal{H}_1)(1-\mathcal{P}_d)\Sigma_{i=1}^{n_r}P_{0,i}^{(n)} + \mathcal{P}(\mathcal{H}_1)\mathcal{P}_d\Sigma_{i=1}^{n_r}P_{1,i}^{(n)}\} \leq P_{av} \tag{5.13}$$

Also, the MISO interference of each subcarrier to the TV PU is limited to a certain value Γ as

$$\begin{aligned}\mathbb{E}_{\mathbf{H}^{(n)},\mathbf{g}^{(n)}}\{\mathcal{P}(\mathcal{H}_1)(1-\mathcal{P}_d)\|\mathbf{g}_0^{(n)}\mathbf{U}_0^{(n)}\|^2\mathbf{P}_0^{(n)} \\ +\mathcal{P}(\mathcal{H}_1)\mathcal{P}_d\|\mathbf{g}_1^{(n)}\mathbf{U}_1^{(n)}\|^2\mathbf{P}_1^{(n)}\} \leq \Gamma\end{aligned} \tag{5.14}$$

$\mathbf{U}_0^{(n)}$ and $\mathbf{U}_1^{(n)}$ are the precoding matrices in case of TV PU absence and TV PU presence, respectively. Also $\mathbf{g}_0^{(n)}$ and $\mathbf{g}_1^{(n)}$ are the selected WBPLC-TV PU channel gain for the cases of TV PU absence and presence, respectively. The criterion of selection is according to the precoding scheme as mentioned in Section 5.3. $\mathbf{P}_0^{(n)}$ and $\mathbf{P}_1^{(n)}$ are the WBPLC signal power vectors in case of TV PU absence and presence, respectively where $P_{0,i}^{(n)}$ and $P_{1,i}^{(n)}$ are their i-th elements, respectively.

5.4.2 Power Allocation

In [86] a power allocation algorithm was proposed for SISO cognitive system. In this work the allocated power is derived for each cognitive radio MIMO sub-channel (TVWS and BPLC) taking into consideration the use of SVD/P-SVD as a precoding technique. The power is allocated to each sub-channel in both cases of TV PU presence and absence. The power allocation is done in a way to maximise the WBPLC MIMO capacity for each subcarrier and satisfy both WBPLC average power and TV PU Rx interference power limit. Hence, the problem of allocating

the power can be formulated as

$$\max_{P_{0,i}^{(n)},P_{1,i}^{(n)}}(R^{(n)}) = \Big(\frac{T-\tau}{T}\Big)\mathbb{E}_{\mathbf{H}^{(n)},\mathbf{g}^{(n)}}\{\mathcal{P}(\mathcal{H}_0)(1-\mathcal{P}_{fa})r_{00}^{(n)} + \mathcal{P}(\mathcal{H}_0)\mathcal{P}_{fa}r_{01}^{(n)} + \mathcal{P}(\mathcal{H}_1)(1-\mathcal{P}_d)r_{10}^{(n)} + \mathcal{P}(\mathcal{H}_1)\mathcal{P}_d r_{11}^{(n)}\} \tag{5.15}$$

Subject to (5.13), (5.14) and $P_{0,i}^{(n)}, P_{1,i}^{(n)} \geq 0$, where the $\frac{\Pi_{I0}}{N}$ is omitted to simplify the derivation. The dual Lagrangian function can be represented as

$$\begin{aligned} &L(P_{0,i}^{(n)}, P_{1,i}^{(n)}, u, v) = \\ &\Big(\frac{T-\tau}{T}\Big)\mathbb{E}_{\mathbf{H}^{(n)},\mathbf{g}^{(n)}}\{\mathcal{P}(\mathcal{H}_0)(1-\mathcal{P}_{fa})r_{00}^{(n)} + \mathcal{P}(\mathcal{H}_0)\mathcal{P}_{fa}r_{01}^{(n)} \\ &+ \mathcal{P}(\mathcal{H}_1)(1-\mathcal{P}_d)r_{10}^{(n)} + \mathcal{P}(\mathcal{H}_1)\mathcal{P}_d r_{11}^{(n)}\} - v\mathbb{E}_{\mathbf{H}^{(n)},\mathbf{g}^{(n)}}\{ \\ &\mathcal{P}(\mathcal{H}_0)(1-\mathcal{P}_{fa})\Sigma_{i=1}^{n_r}P_{0,i}^{(n)} + \mathcal{P}(\mathcal{H}_0)\mathcal{P}_{fa}\Sigma_{i=1}^{n_r}P_{1,i}^{(n)} \\ &+ \mathcal{P}(\mathcal{H}_1)(1-\mathcal{P}_d)\Sigma_{i=1}^{n_r}P_{0,i}^{(n)} + \mathcal{P}(\mathcal{H}_1)\mathcal{P}_d\Sigma_{i=1}^{n_r}P_{1,i}^{(n)}\} \\ &+ vP_{av} - u\mathbb{E}_{\mathbf{H}^{(n)},\mathbf{g}^{(n)}}\{\mathcal{P}(\mathcal{H}_1)(1-\mathcal{P}_d)\|\mathbf{g}_0^{(n)}\mathbf{U}_0^{(n)}\|^2\mathbf{P}_0^{(n)} \\ &+ \mathcal{P}(\mathcal{H}_1)\mathcal{P}_d\|\mathbf{g}_1^{(n)}\mathbf{U}_1^{(n)}\|^2\mathbf{P}_1^{(n)}\} + u\Gamma \end{aligned} \tag{5.16}$$

The dual problem can be represented as

$$d(v,u) = \sup_{P_{0,i}^{(n)},P_{1,i}^{(n)}} L(P_{0,i}^{(n)}, P_{1,i}^{(n)}, u, v) \tag{5.17}$$

In order to obtain the supremum of the Langrangian with respect to the transmission powers, the primal dual decomposition can be used. Let $i \in 1, 2, .., n_r$ be an index for the MIMO sub-channel and $j \in 0, 1$ be an index for the TV PU status (*i.e.*, 0 in case of absence and 1 in case of presence). Also, let $\eta_0 =$

$\mathcal{P}(\mathcal{H}_0)(1-\mathcal{P}_{fa})$, $\eta_1 = \mathcal{P}(\mathcal{H}_0)\mathcal{P}_{fa}$, $\beta_0 = \mathcal{P}(\mathcal{H}_1)(1-\mathcal{P}_d)$ and $\beta_1 = \mathcal{P}(\mathcal{H}_1)\mathcal{P}_d$. Using the primal dual decomposition, the joint variable optimisation problem can be subdivided into $n_r \times 2$ single variable convex optimisation problems as

$$\begin{aligned}\max_{P_{j,i}^{(n)} \geq 0} (f(P_{j,i}^{(n)})) &= \Big(\frac{T-\tau}{T}\Big)\mathbb{E}_{\mathbf{H}^{(n)},\mathbf{g}^{(n)}}\{\eta_j r_{0j,i}^{(n)} + \beta_j r_{1j,i}^{(n)}\} \\ &- v\mathbb{E}_{\mathbf{H}^{(n)},\mathbf{g}^{(n)}}\{(\eta_j+\beta_j)P_{j,i}^{(n)}\} - u\mathbb{E}_{\mathbf{H}^{(n)},\mathbf{g}^{(n)}}\{\beta_j \alpha_{j,i,k}^{(n)} P_{j,i}^{(n)}\}\end{aligned} \tag{5.18}$$

Using the subgradient method, the solution to each problem can be addressed as

$$P_{j,i}^{(n)} = \lceil A_{i,j} + \sqrt{B_{i,j}} \rceil^{+} \tag{5.19}$$

where

$$A_{i,j} = \frac{\Big(\frac{T-\tau}{T}\Big)\log_2(e)(\eta_j+\beta_j)}{v(\eta_j+\beta_j) + u\beta_j\alpha_{j,i,k}^{(n)}} + \frac{2(\sigma_z^2 + \sigma_E^2 P_{av}^{(n)}) + \sigma_p^2}{\lambda_{j,i}^{(n)}} \tag{5.20}$$

$$\begin{aligned}B_{i,j} = A_{i,j}^2 - \frac{4}{\lambda_{j,i}^{(n)}}\Big[&\frac{(\sigma_z^2 + \sigma_E^2 P_{av}^{(n)}) + \sigma_p^2}{\lambda_{j,i}^{(n)}\sigma_p^2} - \\ &\frac{\Big(\frac{T-\tau}{T}\Big)\log_2(e)(\eta_j((\sigma_z^2 + \sigma_E^2 P_{av}^{(n)}) + \sigma_p^2) + \beta_j(\sigma_z^2 + \sigma_E^2 P_{av}^{(n)}))}{v(\eta_j+\beta_j) + u\beta_j\alpha_{j,i,k}^{(n)}}\Big]\end{aligned} \tag{5.21}$$

5.5 Simulation Results

5.5.1 Simulation Setup

In this section, the simulation results are presented for the proposed system compared to the MIMO BPLC [17] and the BPLC WiFi [18]. The OFDM symbol duration T is taken to be 5 ms. It is assumed that the BPLC channel as well as its noise has cyclostationary behavior with a coherence time which is typically half of the mains period (*i.e.*, 10 ms) [87]. For the VHF wireless channel, a Rayleigh fading channel is assumed with average path loss as in (2.1), the l, α and d_0 are set to 1.5, 0.65 and 12 m, respectively [22]. The total bandwidth from 54 MHz to 88 MHz is divided into 5 channels. Each channel has 6 MHz bandwidth. The transmission PSDs for the WBPLC, MIMO BPLC and BPLC WiFi are set to -47 dBm/Hz, -85 dBm/Hz and -50 dBm/Hz, respectively. The received SNR (*i.e.*, the ratio of the received signal power to the power sum of the AWGN and the channel estimation error variance, regardless of the PU interference power) varies from 20 dB to 40 dB. The requested probability of false alarm and detection probability are 10^{-7} and 0.9999, respectively. Also, the probability of TV PU presence is 0.4. The received PU SNR is assumed to be -14 dB. n_r and n_t are assumed to be equal 2. Also, energy detection algorithm is adopted for cognitive sensing and the OR-rule technique is adopted for MIMO sensing.

For the simulation of the power line environment, the random class topology generator presented in Chapter 3 is used. Each iteration, a random power line topology is generated and 4 points are randomly selected to represent WBPLC Tx and Rx and two TV PU Rxs.

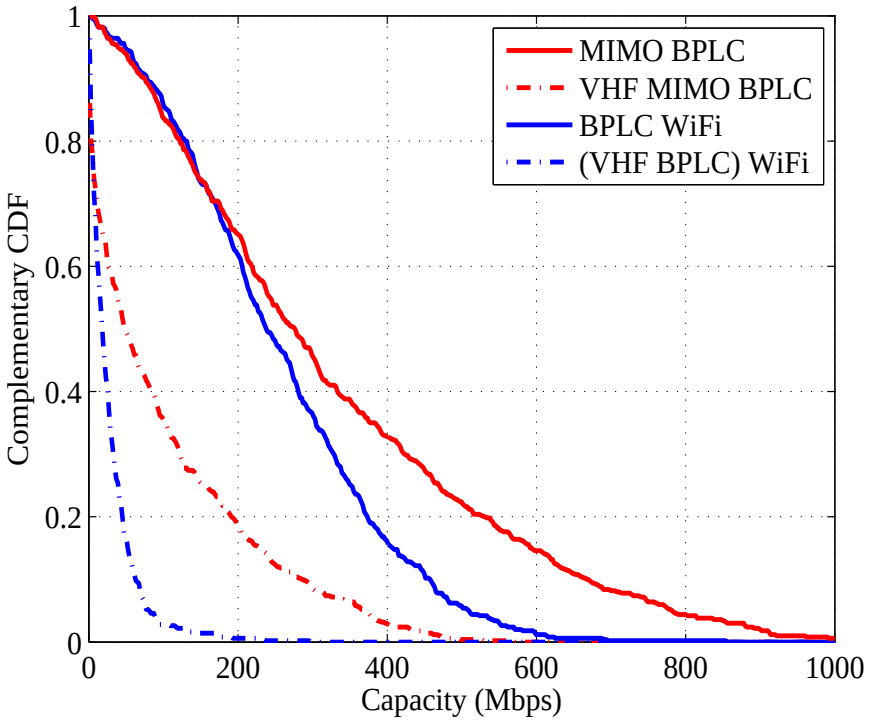

FIGURE 5.3: Complementary CDF vs. ergodic capacity at different frequency bands

5.5.2 Simulation Results

Capacity and spectral efficiency at different frequency bands coverage

In Fig. 5.3, the capacity complementary cumulative distribution function (CCDF) of the MIMO BPLC [17] and the BPLC WiFi [18] is compared for different frequency bands. The degradation in the performance is observed in the case of using VHF BPLC compared to the conventional BPLC. In the conventional BPLC, both the HF band below 30 MHz and the VHF band are allowed. Hence, more transmission power can be allocated to the HF band of the conventional BPLC leading to more capacity compared to the VHF BPLC.

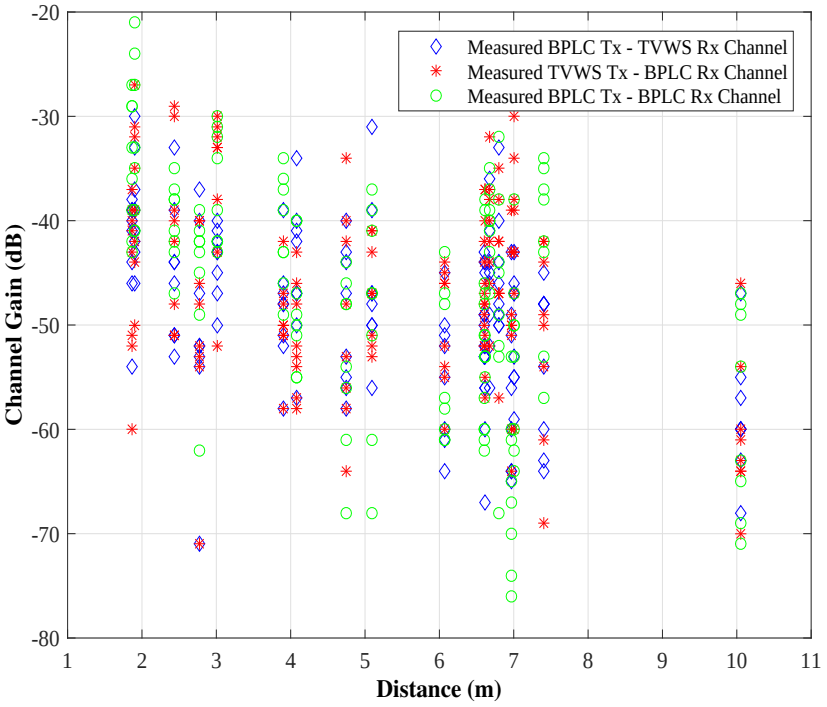

FIGURE 5.4: Measured Channel gain of the cross-talk channel between BPLC and wireless TVWS compared to BPLC channel gain

WBPLC spectral efficiency

In Fig. 5.4, the measured channel gain of the cross-talk channel between BPLC and wireless TVWS channel is shown for variable distances in the VHF band based on our previous measurements that were discussed in Chapter 3. In Fig. 5.5, the average SEs of the SISO BPLC and wireless TVWS channels are compared with their counterparts in case of the crosstalk channels. Also, the SE of the full MIMO WBPLC system is shown in Fig. 5.5. The comparison clarifies the benefit of combining both the TVWS and BPLC channels, by compromising the radiation accompanying the BPLC signal and further exploiting the crosstalk channels.

In Fig. 5.6, the average SE of the proposed system is compared to the MIMO BPLC [17] and the BPLC WiFi [18] in the VHF band. Two notable observations

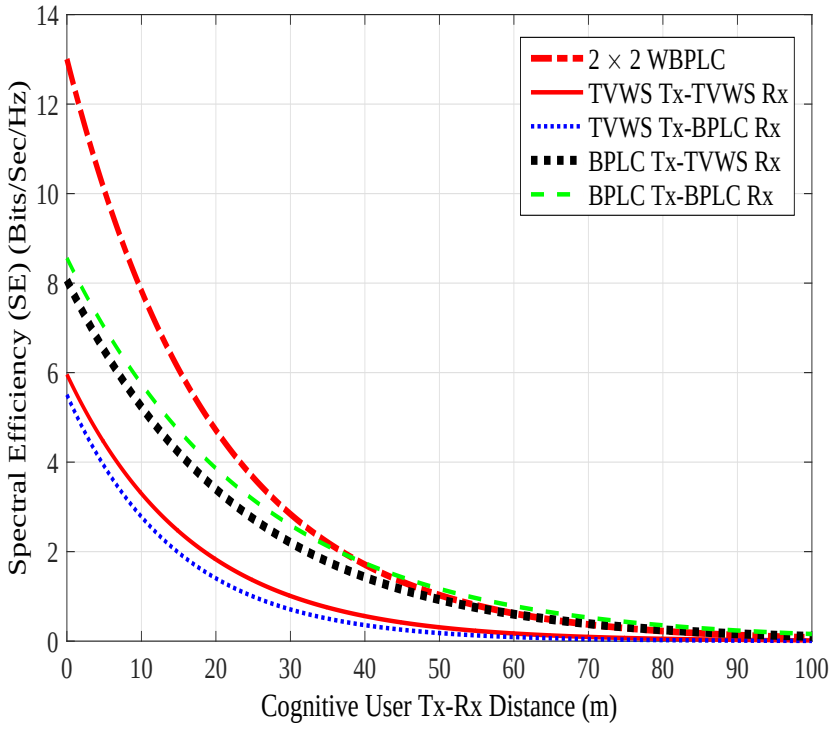

FIGURE 5.5: Average cognitive user SE vs. Tx-Rx distance for BPLC channel, TVWS channel and crosstalk channels

can be addressed: First, the proposed system significantly improves the SE compared to the MIMO BPLC and the BPLC WiFi. this is due to compliance with the TVWS standard, which allows a transmission power of 100 mW per 6 MHz channel and yet a PSD of -47 dBm/Hz. This yields a 38 dB increase in the PSD in the VHF band compared to the IEEE 1901 standard used in the MIMO BPLC. Also, the VHF band has better channel gain than the 2.45 GHz band used in the BPLC WiFi. Second, a slight degradation in the performance in the WBPLC for the non opportunistic case compared to the opportunistic case. This is due to the PU user interference in the opportunistic case that decreases the achievable capacity in the presence of the PU.

In Fig. 5.7, the proposed WBPLC SE shows a rapid saturation to the maximum as the distance ratio increases. This proves that the proposed system including

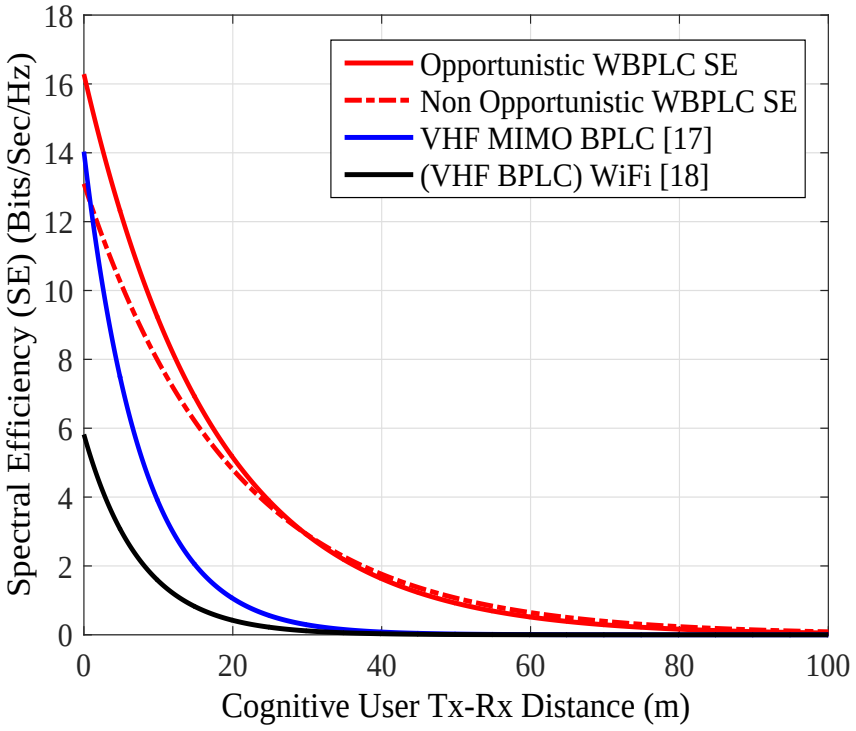

FIGURE 5.6: Average cognitive user SE vs. Tx-Rx distance

the two modes of operation are less interfering to the PU Rx even if they are located at very close distance to the PU Rx. This is due to the use of the proposed iterative precoding algorithm that has the ability to mitigate the interference with the nearby TV PU Rx.

Coupling loss vs. sensing time

The coupling loss represents the power loss due to coupling between the BPLC channel and the VHF wireless channel. As the coupling increases the coupling loss decreases and vice versa. In Fig. 5.8, the effect of increasing the coupling loss on increasing the sensing time can be shown for the conventional cognitive BPLC. However, for the proposed system since MIMO sensing scheme is used with the

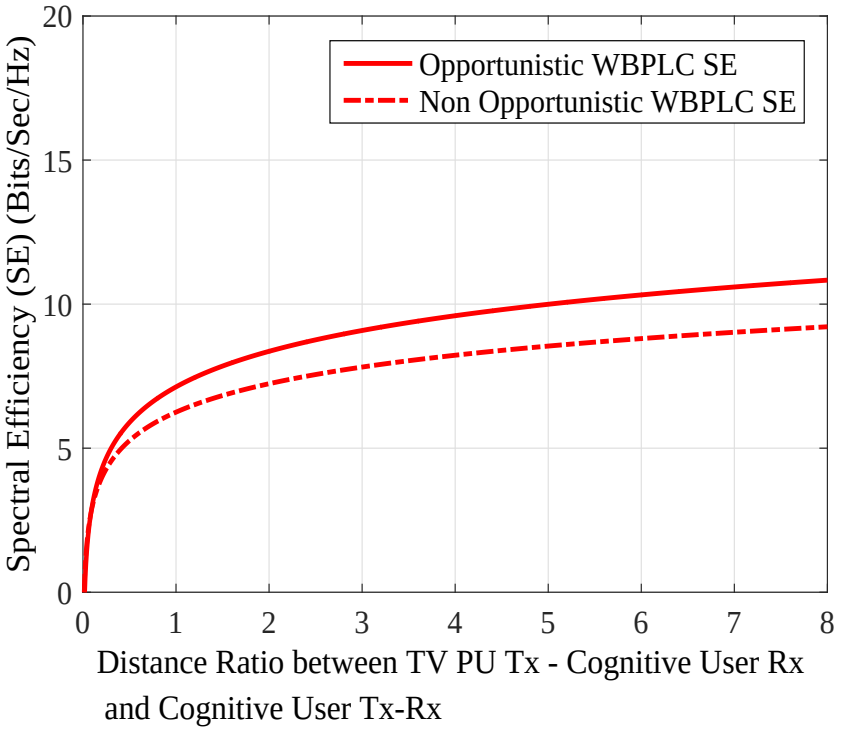

FIGURE 5.7: Average cognitive user SE vs. the ratio between the TV PU Rx cognitive user Tx distance and the cognitive user Tx-Rx distance

aid of the TVWS antenna, the increase in the coupling loss is not affecting the overall sensing time.

Spectral Efficiency vs. Channel Estimation Error

In Fig. 5.9, the effect of the channel estimation error is shown. The simulated values of σ_E^2 represent the measured values of channel estimation error variance for the indoor environment in the VHF band [80]. The ergodic capacity of both the WBPLC and the cognitive BPLC is degraded to 0.6 of its value, on increasing the σ_E^2 from 0 to 10^{-6}. However, the WBPLC still outperforms the conventional cognitive BPLC even at high channel estimation error.

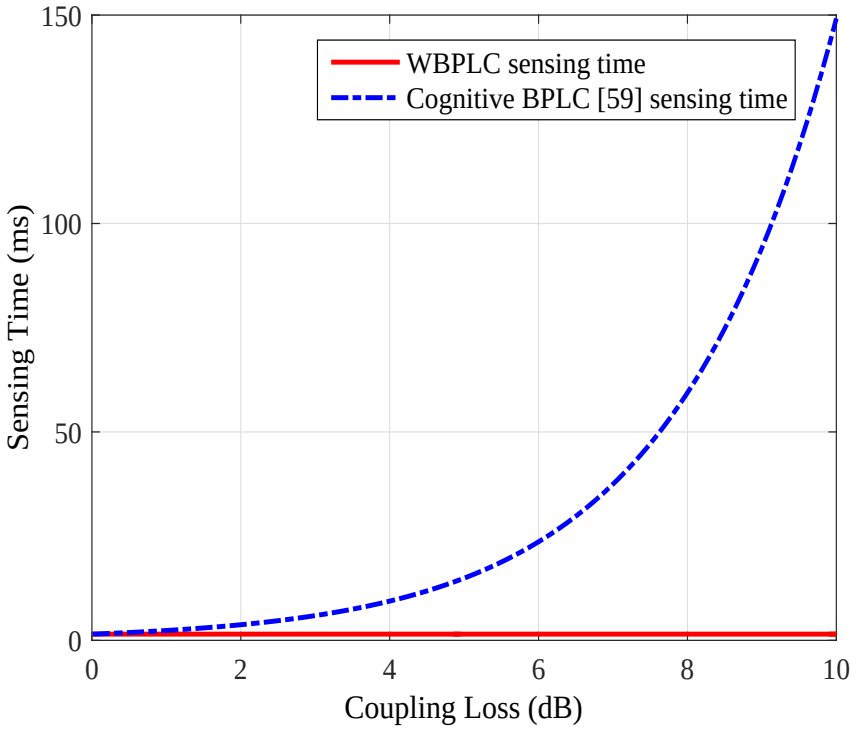

FIGURE 5.8: Spectrum sensing time vs. coupling loss

Ergodic capacity of the VHF band

In this part, the ergodic capacity is computed for the VHF band between 54 MHz and 88 MHz.

In Fig. 5.10, the complementary cumulative distribution function (CCDF) is presented versus the capacity. It can be observed that for the conventional cognitive BPLC system less than 0.2 % of the users can achieve 200 Mbps, for the BPLC WiFi 10% can achieve the 200 Mbps and for the MIMO BPLC 30% can achieve the same capacity. However, for the proposed system more than 95 % of the users can achieve 200 Mbps and more than 50 % can achieve 400 Mbps.

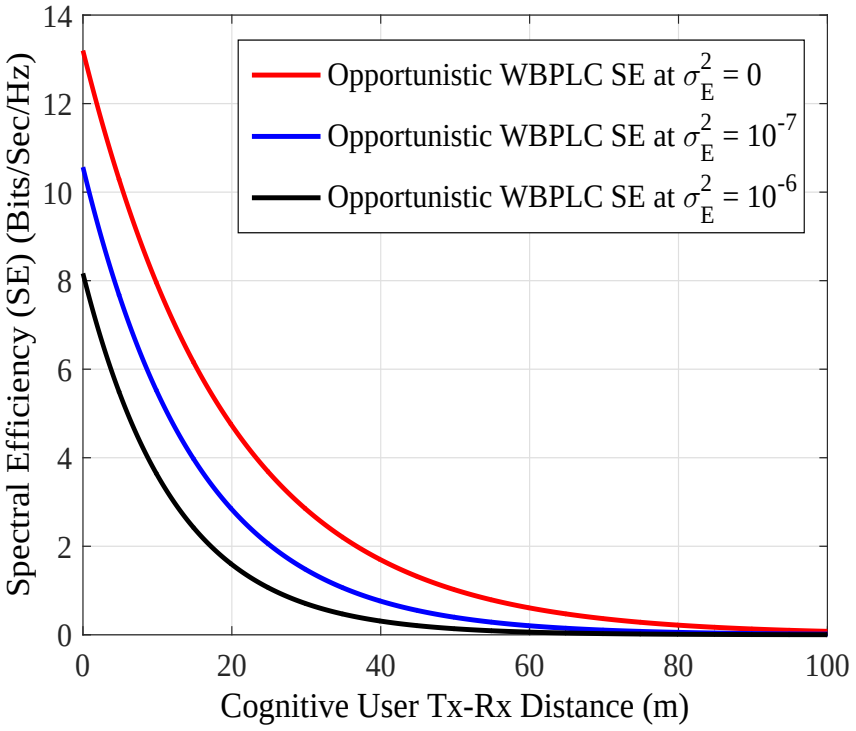

FIGURE 5.9: Average cognitive user SE vs. Tx-Rx distance at different CSI error values

5.5.3 Discussion on practical implementation and measurement results

The enhancement in the ergodic capacity achieved by the WBPLC transceiver is for two main reasons: 1) The compliance of the system with the TVWS standard [9], which allows higher Tx PSD compared to IEEE 1901 [16] or HomePlug AV2 [17]; 2) The enhancement in the sensing capability by using a wireless antenna rather than using the BPLC coupling circuit. Hence, the coupling loss introduced by both power line cables and BPLC coupling circuit can be avoided. However, in certain cases, some TV frequency channels are not allowed to be accessed in a cognitive mode under the TVWS standard [9], *e.g.*, fixed cognitive devices are not allowed to access the TVWS channels in the VHF that is adjacent to TV channels

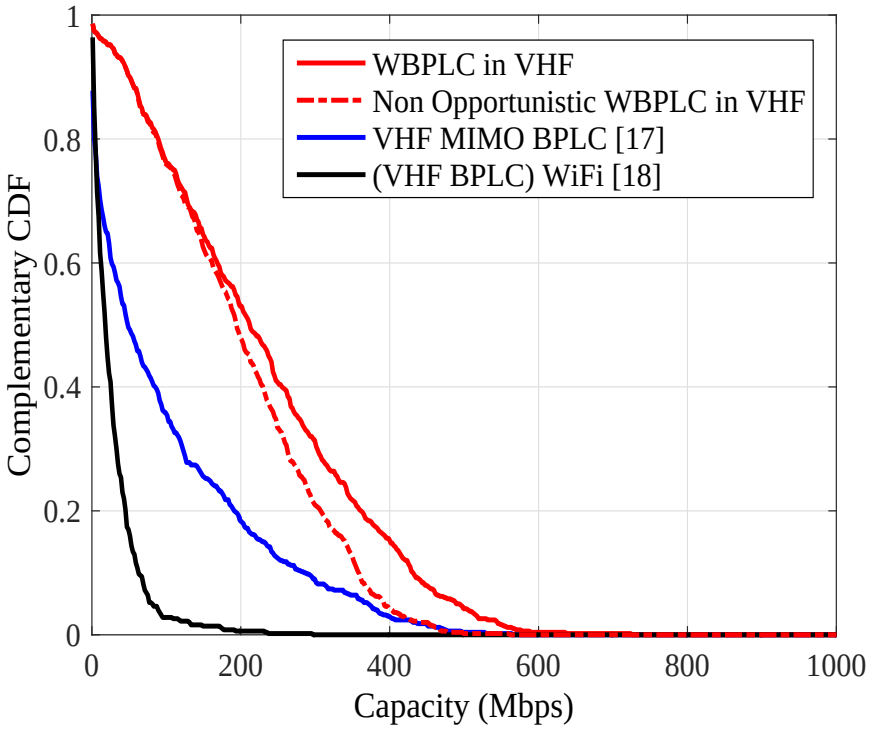

FIGURE 5.10: Complementary CDF vs. ergodic capacity in the VHF band

in operation [9]. In such cases, the WBPLC Tx can send data using the IEEE 1901 standard with a Tx PSD of -85 dBm/Hz, which can sufficiently protect the TV PU Rx. Since OFDM is adopted in the WBPLC transceiver, the PSD of the Tx can be controlled according to the allowed TV frequency channels that can be accessed under a cognitive regime.

5.6 Summary

In this Chapter, a novel hybrid WBPLC point-to-point system has been proposed for the indoor communication network. The proposed system offers a cost-effective solution for enhancing the BPLC capacity in the VHF band. Also, an iterative precoding algorithm has been proposed to mitigate the interference with

the TV PU Rxs in the VHF band. Moreover, an MIMO power allocation algorithm has been developed for the cognitive radio system. Through simulations it has been shown that the proposed system improves the BPLC capacity significantly. In the simulations, a single BPLC subchannel has been considered to form a 2×2 WBPLC system. The capacity of the proposed system can be further enhanced by using MIMO BPLC together with the TVWS wireless channel. The capacity enhancement has been preserved under small separation distances from the TV PU Rx. Moreover, the proposed system demonstrates robust performance against the variation in the BPLC coupling loss which affects the cognitive BPLC sensing time and capacity in the VHF band. In Chapter 6, this system will be developed to include other parameters such as: point-to-multipoint and throughput maximisation for given bit error rate.

Chapter 6

MIMO White BPLC Point-to-Multi-Point System

6.1 Introduction

In the previous Chapter, the hybrid WBPLC MIMO system was proposed. The case of point-to-point communication was studied for the new hybrid system, showing the achievable enhancement compared to MIMO BPLC and BPLC WiFi systems. In this Chapter, a point-to-multi-point WBPLC communication system is proposed. The proposed WBPLC exploits both the TVWS and the BPLC in the VHF band following the cognitive channel access regulation, and the BPLC only in the HF band. The problem of maximising the achievable downlink capacity is studied under the constraints of total average power and different PSDs defined in the FCC and the IEEE 1901 standards. An algorithm is proposed which acquires the optimal power and frequency allocation for each user to achieve the maximum total capacity for a given bit error rate (BER) performance.

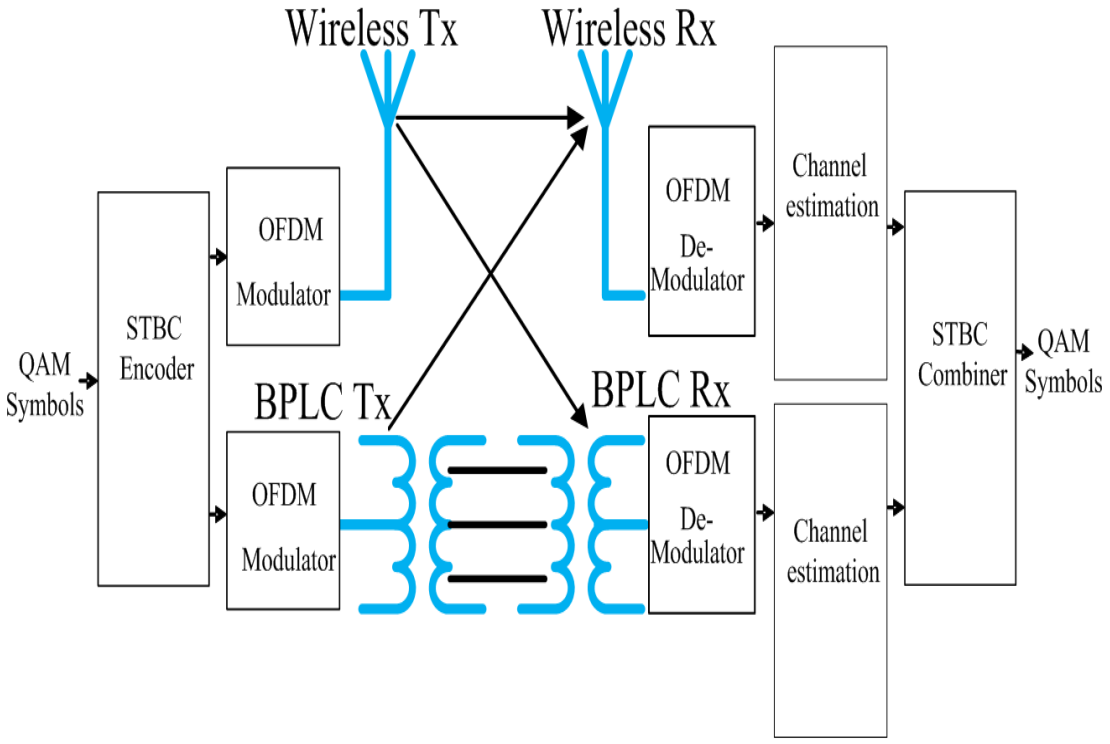

FIGURE 6.1: WBPLC system model in office environment

The rest of the Chapter is organised as follows. In Section 6.2, the proposed WBPLC system model is presented. In Section 6.3, the frequency and power allocation problem for different users are investigated and the optimal solution is proposed. In Section 6.4, the performance of the proposed WBPLC system is evaluated through simulations and compared against the TVWS and the MIMO BPLC systems. In Section 6.5, the Chapter is summarised.

6.2 System Model

The proposed WBPLC transmit cooperatively in both the TVWS and BPLC channels. Hence, it incorporates both the ECMA-392 and the HomeplugAV2 standards. In this Chapter, the downlink is investigated for a point-to-multi-point WBPLC indoor system, which adopts the space time block coding (STBC) to

maximise the diversity gain of the MIMO TVWS BPLC channel. The M-ary quadrature amplitude modulation (M-QAM) with gray bit mapping is used as a sub-modulation for the subcarriers in the OFDM symbol. Also, the noise is assumed to be additive white Gaussian noise (AWGN) with zero mean and variance N_0. The system model for the WBPLC point-to-multi-point communication system is shown in Fig. 6.1. The sink is connected to a geolocation database to obtain the PU temporal and geographical map of access to the TV channels. In the downlink, the sink allocates the TV channels and the corresponding transmission power to each user in order to achieve maximum overall capacity. The WBPLC has three modes of operation according to the frequency band and the PU activity.

Mode A

This mode spans the frequency band 1.8 MHz - 30 MHz. Hence, HomplugAV2 standard is adopted for the PHY and MAC layers in communication. According to IEEE 1901 and HomeplugAV2 the PSD of the transmitted signal below 30 MHz is -55 dBm/Hz. Also, 1156 subcarriers are used in this band with frequency spacing of 24.414 kHz. Hence, the overall transmit power for each channel can reach up to 0.244 mW. The band below 30 MHz has the advantage that it is a completely free band, which can provide a backup channel when all the TVWS channels are occupied. In the WBPLC, SISO BPLC is used for communication, while in the high throughput WBPLC (HT-WBPLC), the MIMO BPLC can be used, which exploits the HF band in the BPLC channel through STBC coding. The maximum number of the used spatial channels are 2 Tx channels and 2 Rx channels.

Mode B

This mode deals with the case of the PU absence in the VHF band. Hence, the spanned frequency spectrum is 54 MHz - 200 MHz. According to FCC regulations, 9 TV channels are allowed for cognitive access in this band which are: 54 MHz - 60 MHz, 60 MHz - 66 MHz, 66 MHz - 72 MHz, 76 MHz - 82 MHz ,82 MHz - 88 MHz, 174 MHz - 180 MHz, 180 MHz - 186 MHz, 186 MHz - 192 MHz and 192 MHz - 198 MHz. ECMA-392 standard is adopted in the PHY and MAC layers' design. Each 6 MHz channel is spanned by 128 subcarriers, with subcarrier frequency spacing of 46 kHz. Consequently, the maximum allowed PSD for each 6 MHz channel is -47.7 dBm/Hz given that the maximum transmission power is 100 mw. However, for the adjacent channel to an occupied TV channel, the PSD is -51.7 dBm/Hz, which corresponds to a transmission power of 40 mW. As a result, the WBPLC system offers the BPLC at least 34 dB increase in the PSD in the VHF band, hence can significantly improve the achievable capacity. In the WBPLC, SISO BPLC channel is used cooperatively with the wireless TVWS channel. Hence, the maximum spatial channels are 2 at the Tx and 2 at the Rx. For the HT-WBPLC, MIMO BPLC channel is used, and hence 3 channels are available at the Tx and 3 channels at the Rx. Since, orthogonal STBC codes are adopted in HT-WBPLC, the maximum number of spatial channels at the Tx is limited to 2.

Mode C

This mode deals with the case of the PU presence in the VHF band. The spanned frequency band is 30 MHz - 200 MHz. HomeplugAV2 standard is adopted for the PHY and MAC layers of communications. Hence, the PSD is restricted to

Table 6.1: WBPLC Modes of Operation

	Mode A	Mode B	Mode C
Frequency Band	1.8 MHz - 30 MHz	54 MHz - 200 MHz	30 MHz - 200 MHz
Communication Standard	HomeplugAV2	ECMA-392	HomeplugAV2
PSD	-55 dBm/Hz	-47.7 dBm/Hz (free channel), -51.7 dBm/Hz (adjacent channel)	-80 dBm/Hz
Tx/Rx Ports maximum number	2 Tx & 2 Rx	2 Tx & 3 Rx	2 Tx & 3 Rx
Number of Subcarriers	1156	1152	1260
Subcarrier frequency spacing	24.414 kHz	46 kHz	46 kHz

-80 dBm/Hz. The frequency band from 30 MHz - 200 MHz is spanned by 1260 subcarrier with frequency spacing of 46 kHz. The maximum number of the allowed spatial channels is 2 Tx channels and 3 Rx channels in the HT-WBPLC.

The main features of the three modes of operation for the WBPLC are summarised in Tables 6.1.

6.3 Capacity Maximisation based Power and Subcarrier Allocation

6.3.1 Problem Formulation

In the WBPLC, there are N_1 subcarriers in the HF band 1.8 MHz - 30 MHz. In this band, the WBPLC Tx uses the N_1 subcarriers of the BPLC channel only under the PSD constraint of the HomeplugAV2 [17]. In the VHF band 30 MHz -

200 MHz, there are N_2 subcarriers that are used by the WBPLC Tx under one of the following two conditions:

1. PU absence: In this case, the WBPLC Tx uses both the TVWS wireless channel and the BPLC channel in the transmission of the data across the N_2 subcarriers. STBC is adopted in the transmission across the two channels in order to enhance the diversity gain. The transmission power is also constrained according to the ECMA-392 standard in [11].

2. PU presence: In this case, the WBPLC Tx uses the BPLC channel only in the transmission under the PSD constraint of HomeplugAV2.

Since the case of the downlink between the sink and the users is considered, the target of the power and subcarrier allocation is to achieve maximum capacity and also satisfy the different power constraints by the different standards at different frequency bands. Let $P_{e_{nj}}$, $2^{k_{nj}}$, P_{nj} be the BER, the constellation size and the allocated power for the nth subcarrier of the jth user, respectively, and N_t, N_r, ζ be the numbers of the Tx and the Rx ports and the STBC code rate, respectively. The effective MIMO channel gain C_{nj} after the STBC decoder can be calculated as $\sum_{n_t=1}^{N_t} \alpha_{n_t} \sum_{n_r=1}^{N_r} |h_{n_t n_r}|^2$, where α_{n_t} is the ratio of the power allocated at the Tx for each spatial path, $h_{n_t n_r}$ is the channel gain of spatial path $n_t n_r$ for a given subcarrier and user. Following [88], α_{n_t} is calculated as

$$\alpha_{n_t} = \sqrt{\frac{\beta_{n_t}}{\sum_{n_t=1}^{N_t} \beta_{n_t}}} \tag{6.1}$$

where $\beta_{n_t} = \sum_{n_r=1}^{N_r} |h_{n_t n_r}|^2$. In the case of SISO channel, C_{nj} is simply the channel gain $|h_{n_t n_r}|^2$ and α_{n_t} is taken as 1. Hence, a simple approximated BER expression can be adopted as in [89]

$$P_{e_{nj}} = \frac{0.2}{\left[1 + \frac{1.6}{2^{k_{nj}}-1}\frac{P_{nj}C_{nj}}{N_t \zeta N_0}\right]^{N_t N_r}} \tag{6.2}$$

Let the $P_{e_{nj}}$ be the same for all subcarriers and users and equal to the target BER P_e. Hence, the number of bits k_{nj} assigned for subcarrier n and user j is expressed as

$$k_{nj} = \log_2 \frac{1 + 1.6 P_{nj} C_{nj}}{N_t \zeta N_0 \left[(0.2/P_e)^{\frac{1}{N_t N_r}} - 1\right]} \tag{6.3}$$

The WBPLC has three different modes of operation as mentioned in Section 6.2. Correspondingly k_{nj} has three different expressions.

Mode A

In this mode, the BPLC channel is the only channel available and hence, N_{t_A}, N_{r_A} and ζ are assumed to be equal to 1. However, in HT-WBPLC, N_{t_A} and N_{r_A} are equal to 2. Also, the $P_{n_A j}$ allocated for each subcarrier should be lower than a maximum power P_A, which is the maximum power that can be allocated for the subcarrier to satisfy the PSD constraint of the HomeplugAV2 in the HF band. The number of the bits $k_{n_A j}$ assigned to mode A subcarrier n_A of the jth user can be expressed using (6.3) as:

$$k_{n_A j} = \log_2 \frac{1 + 1.6 P_{n_A j} C_{n_A j}}{N_{t_A} N_0 \left[(0.2/P_e)^{\frac{1}{N_{t_A} N_{r_A}}} - 1\right]} \tag{6.4}$$

Mode B (30 MHz - 84 MHz & PU absence)

In this case both the BPLC and the TVWS channels are used. Let PH_0 represent the probability of the PU absence. Since the frequency band from 30 MHz to 54 MHz is not allowed for TVWS communication, PH_0 is equal to zero in this band. The number of bits $k_{n_{Bj}}^{(0)}$ assigned to mode B subcarrier n_B of the jth user can be expressed as

$$k_{n_{Bj}}^{(0)} = PH_0 \log_2 \frac{1 + 1.6 P_{n_{Bj}}^{(0)} C_{n_{Bj}}^{(0)}}{N_{t_B}^{(0)} N_0 \left[(0.2/P_e)^{\frac{1}{N_{t_B}^{(0)} N_{r_B}^{(0)}}} - 1 \right]} \tag{6.5}$$

The allocated power $P_{n_{Bj}}^{(0)}$ for each subcarrier should be below a maximum power $P_B^{(0)}$ to satisfy the transmitter Tx power constraint of the ECMA-392 standard. $N_{t_B}^{(0)}$ and $N_{r_B}^{(0)}$ take the value of 2 in the case of WBPLC and the values of 2 and 3, respectively in the case of HT-WBPLC. ζ is taken as 1 for full rate STBC coding, where the superscript (0) indicates the absence of the PU.

Mode C (30 MHz - 84 MHz & PU presence)

In this case the BPLC channel is the only channel used and hence, the $k_{n_{Bj}}^{(1)}$ can be expressed as

$$k_{n_{Bj}}^{(1)} = PH_1 \log_2 \frac{1 + 1.6 P_{n_{Bj}}^{(1)} C_{n_{Bj}}^{(1)}}{N_{t_B}^{(1)} (N_0 + N_p) \left[(0.2/P_e)^{\frac{1}{N_{t_B}^{(1)} N_{r_B}^{(1)}}} - 1 \right]} \tag{6.6}$$

where PH_1 and N_p represent the PU presence probability and PU interference power, respectively. Also, the $P_{n_{Bj}}^{(1)}$ should be below a certain power $P_B^{(1)}$ to satisfy the PSD of HomeplugAV2 in the VHF band. Hence, the problem of maximising

the overall capacity T can be expressed as

$$\max_{P_{n_Aj},P^{(0)}_{n_Bj},P^{(1)}_{n_Bj}} T \tag{6.7}$$

where

$$T = (1-P_e)\sum_{j=1}^{K}\Big[\sum_{n_1=1}^{N_1}\frac{k_{n_Aj}}{t_1} + \frac{\sum_{n_B,n_B=1}^{N_2}(k^{(0)}_{n_Bj}+k^{(1)}_{n_Bj})}{t_2}\Big] \tag{6.8}$$

s.t.

(C1) $P_{n_Aj}, P^{(0)}_{n_Bj}, P^{(1)}_{n_Bj} \geq 0$,

(C2) $\sum_{j=1}^{K} P_{n_Aj} \leq P_A$,

(C3) $\sum_{j=1}^{K} P^{(0)}_{n_Bj} \leq P^{(0)}_B$,

(C4) $\sum_{j=1}^{K} P^{(1)}_{n_Bj} \leq P^{(1)}_B$,

(C5) $\sum_{j=1}^{K}\big[\sum_{n_A=1}^{N_1} P_{n_Aj} + \sum_{n_B=1}^{N_2} PH_0 P^{(0)}_{n_Bj} + PH_1 P^{(1)}_{n_Bj}\big] \leq P_{in}$,

(C6) $\frac{\sum_{n_A=1}^{N_1} k_{n_Aj}}{t_1} + \frac{\sum_{n_B=1}^{N_2}(k^{(0)}_{n_Bj}+k^{(1)}_{n_Bj})}{t_2} \geq R_j$. where N_1 and N_2 are the number of subcarriers in the HF and VHF bands, respectively. Also, t_1 and t_2 are the OFDM symbol durations in the HomeplugAV2 and ECMA-392 standards, respectively. R_j is the capacity requested for each user. P_{in} is the total input power to the sink.

The Lagrangian of the problem can be expressed as

$$
\begin{aligned}
L =&(1-P_e)\\
&\sum_{j=1}^{K}\Bigg[\sum_{n_A=1}^{N_1}\frac{1}{t_1}\log_2\{1+\frac{1.6P_{n_Aj}C_{n_Aj}}{N_0\big[(\frac{0.2}{P_e})^{\frac{1}{(N_{t_A}N_{r_A})}}-1\big]}\}+\\
&\sum_{n_B}^{N_2}\frac{PH_0}{t_2}\log_2\{1+\frac{1.6P^{(0)}_{n_Bj}C^{(0)}_{n_Bj}}{(2N_0\big[(\frac{0.2}{P_e})^{\frac{1}{(N^{(0)}_{t_B}N^{(0)}_{r_B})}}-1\big])}\}+\\
&\frac{PH_1}{t_2}\log_2\{1+\frac{1.6P^{(1)}_{n_Bj}C^{(1)}_{n_Bj}}{2(N_0+N_p)\big[(\frac{0.2}{P_e})^{\frac{1}{(N^{(1)}_{t_B}N^{(1)}_{r_B})}}-1\big]}\}\Bigg]-\\
&\lambda\sum_{j=1}^{K}\Bigg[\sum_{n_A=1}^{N_1}P_{n_Aj}+\sum_{n_B=1}^{N_2}PH_0P^{(0)}_{n_Bj}+PH_1P^{(1)}_{n_Bj}\Bigg]+\\
&\lambda P_{in}-\sum_{n_A=1}^{N_1}\mu_{n_A}\Bigg[\sum_{j=1}^{K}P_{n_Aj}-P_A\Bigg]-\\
&\sum_{n_B=1}^{N_2}\mu^{(0)}_{n_B}\Bigg[\sum_{j=1}^{K}P^{(0)}_{n_Bj}-P^{(0)}_B\Bigg]-\\
&\sum_{n_B=1}^{N_2}\mu^{(1)}_{n_B}\Bigg[\sum_{j=1}^{K}P^{(1)}_{n_Bj}-P^{(1)}_B\Bigg]+\\
&\sum_{j=1}^{K}\beta_j\Bigg[\sum_{n_A=1}^{N_1}\frac{1}{t_1}\log_2\{1+\frac{1.6P_{n_Aj}C_{n_Aj}}{N_0\big[(\frac{0.2}{P_e})^{\frac{1}{(N_{t_A}N_{r_A})}}-1\big]}\}+\\
&\sum_{n_B=1}^{N_2}\frac{PH_0}{t_2}\log_2\{1+\frac{1.6P^{(0)}_{n_Bj}C^{(0)}_{n_Bj}}{(2N_0\big[(\frac{0.2}{P_e})^{\frac{1}{(N^{(0)}_{t_B}N^{(0)}_{r_B})}}-1\big])}\}+\\
&\frac{PH_1}{t_2}\log_2\{1+\frac{1.6P^{(1)}_{n_Bj}C^{(1)}_{n_Bj}}{2(N_0+N_p)\big[(\frac{0.2}{P_e})^{\frac{1}{(N^{(1)}_{t_B}N^{(1)}_{r_B})}}-1\big]}\}\Bigg]-\\
&\sum_{j=1}^{K}\beta_jR_j
\end{aligned}
\tag{6.9}
$$

where, λ, μ_{n_A}, $\mu^{(0)}_{n_B}$, $\mu^{(1)}_{n_B}$ and β_j are Lagrangian multipliers. The Lagrangian problem solution is explained in Appendix H.

6.3.2 Problem Solution

The power allocated for each mode of operation to subcarrier n and user j is expressed as

$$P_{n_Aj} = \left[\frac{1+\beta_j}{(t_1(\lambda+\mu_{n_A}))} - \frac{N_0\left[(\frac{0.2}{P_e})^{\frac{1}{(N_{t_A}N_{r_A})}}-1\right]}{1.6C_{n_Aj}}\right] \tag{6.10}$$

$$P^{(0)}_{n_Bj} = \left[\frac{PH_0(1+\beta_j)}{(t_2(PH_0\lambda+\mu^{(0)}_{n_B}))} - \frac{2N_0\left[(\frac{0.2}{P_e})(\frac{1}{(N^{(0)}_{t_B}N^{(0)}_{r_B})})-1\right]}{1.6C^{(0)}_{n_Bj}}\right] \tag{6.11}$$

$$P^{(1)}_{n_Bj} = \left[\frac{PH_1(1+\beta_j)}{(t_2(PH_1\lambda+\mu^{(1)}_{n_B}))} - \frac{2(N_0+N_p)\left[(\frac{0.2}{P_e})(\frac{1}{N^{(1)}_{t_B}N^{(1)}_{r_B}})-1\right]}{1.6C^{(1)}_{n_Bj}}\right] \tag{6.12}$$

Algorithm for subcarrier and user allocation

- Initialisation: Set $\Phi = \{1 \dots K\}$ as the set of users, $\Omega_T = \{1 \dots N_1\} \cup \{1 \dots N_2\}$ as the set of all available subcarriers for all users. Ω_j is the set of the subcarriers allocated to user $j \in \Phi$, $\Omega_j = \{\phi\}$. $\beta_j, \mu_{n_A}, \mu_{n_B}^{(0)}, \mu_{n_B}^{(1)} = 0$.

- Allocate the maximum permissible power for each subcarrier $P_{n_Aj} = P_A$, $P_{n_Bj}^{(0)} = P_B^{(0)}, P_{n_Bj}^{(1)} = P_B^{(1)}$.

- Start a For loop across the subcarriers of Ω_T. The user j in Φ with maximum k_{n_Aj}/t_1 or $(k_{n_Bj}^{(0)} + k_{n_Bj}^{(1)})/t_2$ will be allocated to subcarrier n_A or n_B, respectively. Update $\Omega_j = \Omega_j \cup n_A$ or n_B and $\Omega_T = \Omega_T - n_A$ or n_B. When the rate R_j is achieved $\Phi = \Phi - j$.

- Calculate the optimum power using the obtained user-frequency map in step 3 with the aid of equations (6.10) - (6.12), and find the appropriate λ using the bisection method.

- The subcarriers which are allocated a transmission power that exceeds the maximum power limit are forced below the limit by setting the appropriate value of μ_{n_A}, $\mu_{n_B}^{(0)}$, $\mu_{n_B}^{(1)}$.

- Repeat steps (4) and (5) using the new values of μ_{n_A}, $\mu_{n_B}^{(0)}$, $\mu_{n_B}^{(1)}$ untilthe sum of all transmission power is equal to P_{in}.

6.4 Simulation Results

6.4.1 Simulation Setup

In this part, the WBPLC downlink model in Fig. 6.1 is simulated. The PU presence activity is represented using two state discrete time Markov chain model (DTMC), where the PU presence steady state probability for each 6 MHz TV channel is taken as 0.2. Also, the impulsive noise is represented in the simulations by a two-state DTMC model, where the steady state probability of the non impulsive state is 0.9. The power line class topology generator in Chapter 2 is used in the simulations to model the power line cable, terminal loads and outlet connection and hence, the power line channel. The class topology generator in Chapter 2 is used to generate 100 topologies for each case of simulation. The VHF radio propagation channel is modelled as Rayleigh fading channel with average path loss as in [22]. In the simulations, the HT-WBPLC is compared to the MIMO BPLC [17] and the TVWS systems. The TVWS is implemented using the ECMA-392 standard [11] and the FCC regulations [9].

6.4.2 Simulation Results

In Fig. 6.2, the CCDF of the achievable capacity by the proposed HT-WBPLC system is shown at different input power levels. The input power levels simulated are 50 mW, 100 mW and 1W, which are allocated in the downlink for different users and different subcarriers using the proposed algorithm in Section 6.3. The enhancement is observed in the achievable capacity with the increase in the power

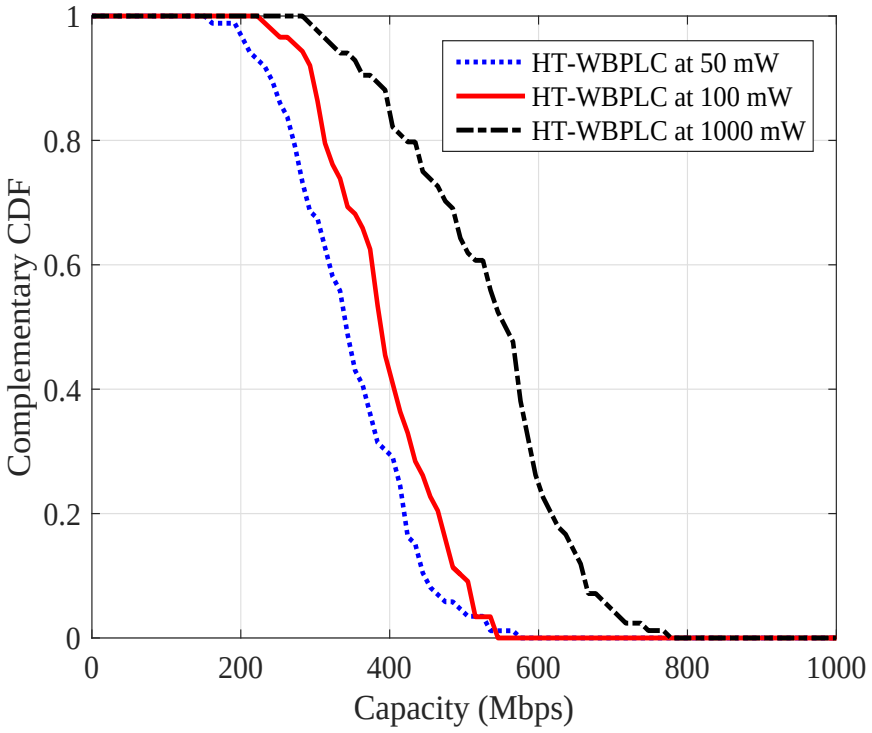

FIGURE 6.2: Complementary CDF of the achievable capacity by the proposed HT-WBPLC using different input power levels

level. Compared to the MIMO BPLC [17], the proposed HT-WBPLC can support higher input power level as it complies with the requirements of the FCC regulations, which allow a 34 dB increase in the PSD than that allowed by the HomeplugAV2 for the BPLC.

The proposed HT-WBPLC is compared to the MIMO BPLC in the frequency band 1.8 MHz - 200 MHz at an input transmission power of 100 mW. In Fig. 6.3, the simulation results show the capacity enhancement of the HT-WBPLC compared to MIMO BPLC [17]. The simulation results show a 30 % enhancement in the CCDF of 200 Mbps capacity and a 40 % increase in the CCDF for 400 Mbps. The enhancement is due to two main reasons: 1) the increase in the permissible PSD in the VHF band yields the allocation of more power to this band. It is worth mentioning that according to the HomeplugAV2 standard, the maximum

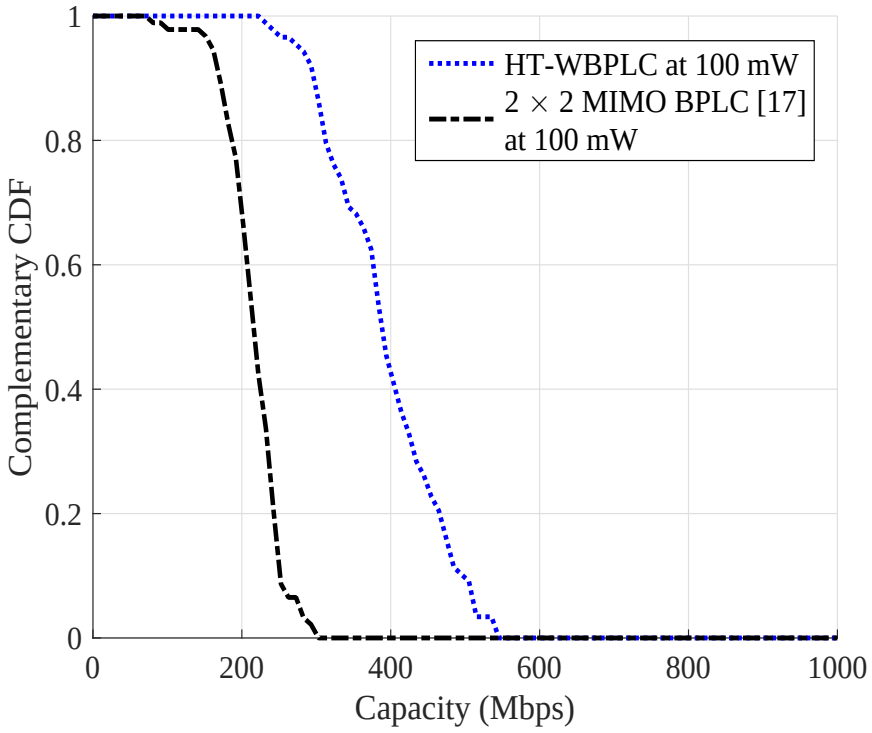

FIGURE 6.3: Complementary CDF of the capacity using the proposed HT-WBPLC and the conventional MIMO BPLC

input power for the BPLC Tx is 282 mW. However, this power is concentrated in the HF band only for the MIMO BPLC; 2) the increase in the allowed spectrum of communication in the VHF band up to 200 MHz.

In Fig. 6.4 the HT-WBPLC capacity CCDF is compared against the MIMO BPLC [17] and the TVWS in the VHF band only. Significant capacity enhancement has been shown in the VHF band by the HT-WBPLC over the other two systems. This proves that the main reason behind the enhancement in the achievable capacity in Fig. 6.3 is due to the exploitation of the VHF band. Also, the results show that both the MIMO BPLC and the TVWS collectively cannot achieve a higher capacity in the VHF band than the HT-WBPLC. This is due to the input PSD limitations for the MIMO BPLC and the MIMO design limitations for the wireless TVWS. The aforementioned problems are solved in the

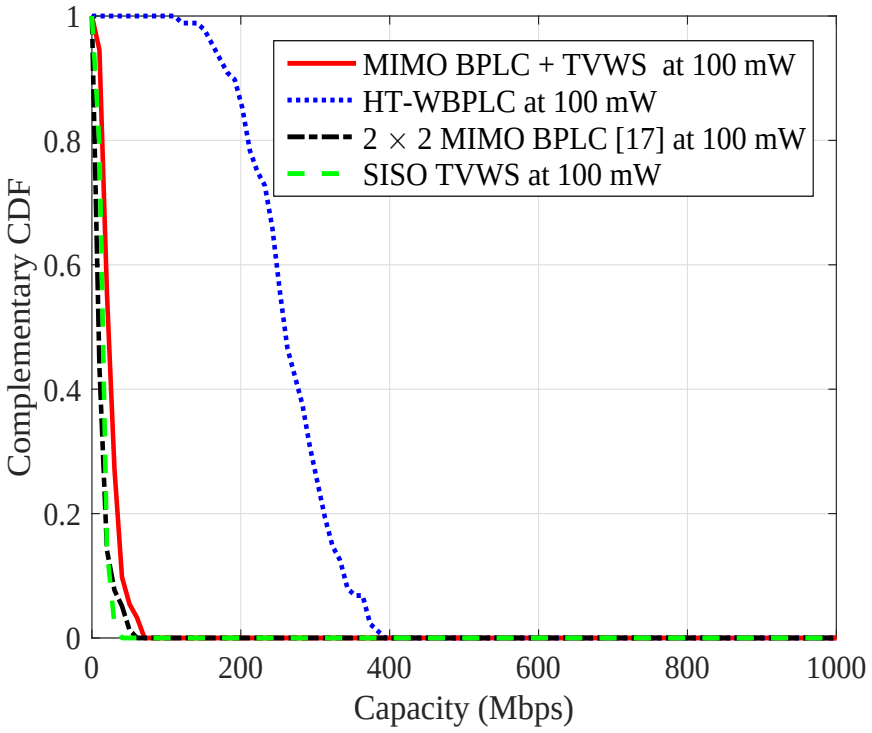

FIGURE 6.4: Complementary CDF of the achievable capacity in the VHF band using the proposed HT-WBPLC and the conventional MIMO BPLC, TVWS and the MIMO BPLC + TVWS

HT-WBPLC, which results in enhancing the achievable capacity in the VHF band.

6.5 Summary

In this Chapter, a WBPLC point-to-multipoint communication system has been proposed, which makes use of the TVWS and BPLC channels in the VHF bands cooperatively, based on the cognitive radio principle. Two folds of benefits have been introduced. The proposed WBPLC overcomes the design challenge in realising an MIMO TVWS in a small footprint design for indoor communications, by offering an MIMO solution over the TVWS-BPLC channels. The WBPLC also overcomes the PSD constraints in BPLC by offering an increase in the permissible PSD and enabling transmission in additional frequency band. Simulation results

have proved the significant enhancement in the achievable capacity of the WBPLC compared to the BPLC and the TVWS. The proposed system is able to increase the achievable capacity by 40 % for the same input power compared to the MIMO BPLC [17] and the TVWS implemented using the ECMA-392 standard [11] and the FCC regulations [9]. The WBPLC can play an important role in satisfying the growing needs of the future indoor networks.

Chapter 7

Conclusions and Future Work

7.1 Conclusions

In this thesis, a new hybrid TVWS BPLC solution referred to as WBPLC is proposed for exploiting the VHF band in the indoor communications. The new solution offers a cost-effective and high throughput solution compared to other hybrid solutions. The cooperation between the TVWS and the BPLC offers a novel solution to the EMC problem of the BPLC in the VHF band by developing a TVWS standard compliant solution. On the same time, it offers the TVWS an MIMO solution in the VHF band at a practical footprint design.

In Chapter 2, an overview of the main standards, challenges and channel characteristics has been presented for both the TVWS and BPLC communication systems. The overview focused on the common features between both technologies in the PHY and MAC layers, which can be exploited to develop a cost-effective hybrid system between both technologies.

In Chapter 3, the channel characteristics of both the BPLC and the TVWS

have been deeply investigated. A GSBPLM approach for representing the path loss of the BPLC channel is proposed. The statistical mapping is general and applicable to the nine classes of the BPLC channel. Also, a GRB method for computing the channel transfer function between two nodes in the BPLC network has been proposed. The new method has less computation complexity compared to previous methods. Also, a comparison between the path loss of the BPLC channel and the wireless channel in the VHF band has been conducted. The comparison has shown that the path loss of both channels is comparable, which provides a preliminary result of the cooperation feasibility between both technologies.

In Chapter 4, the interference of the wireless VHF signal to the BPLC channel has been investigated. Since the interference occurs as a result of the mode conversion between the antenna mode and the differential mode currents, two solutions are proposed for representing the characteristic impedance of the antenna mode current referred to as: ATN and ETLA solutions. The ATN numerical solution has shown the dependence of the characteristic impedance on both the exciting frequency and incidence angle. Also, the ATN solution results have been compared to its counterparts of the FWTL solution. The results of both methods are comparable, while the ATN solution advantage that it does not require the current computation as in the FWTL. The ETLA solution has shown a negligible difference from both ATN and FWTL solutions, while requiring less computation complexity.

In Chapter 5, a new hybrid TVWS BPLC point-to-point communication has been proposed. The ergodic capacity of the hybrid system has been studied in comparison with previous MIMO BPLC and hybrid BPLC WiFi systems. Also,

two modes of operation have been proposed for the new hybrid system, which take into consideration the presence of the TV PU Rx and the availability of its CSI. The new hybrid system has shown a great enhancement in the ergodic capacity compared to other communication systems. Also, the iterative precoding algorithm proposed enhanced the mitigation of the interference with the TV PU Rx. Also, the proposed system offers a lower sensing time for the presence of the TV PU due to the addition of a wireless antenna to the BPLC Rx. The latter addition overcomes the previous coupling loss problem, which exists in the BPLC Rx when receiving wireless signal.

In Chapter 6, the point-to-multipoint case has been investigated using the proposed hybrid TVWS BPLC communication system. The PHY and MAC layer have been developed for the proposed system referred to as WBPLC. The throughput of the proposed system has been studied compared to the throughput of the MIMO BPLC and TVWS communication systems. The simulation results have shown that WBPLC can offer 40% enhancement in the achievable throughput compared to MIMO BPLC and TVWS. The WBPLC has twofold benefit to both the TVWS and the BPLC. WBPLC offers an MIMO solution to the TVWS in the VHF band and offers a higher PSD to the BPLC, while avoiding the interference with the wireless services.

7.2 Future Work

The WBPLC system proposed in this thesis is based on simulations and channel measurements. The study focused on proving the feasibility of the proposed system

from the simulation and channel measurement perspective. However, the practical measurements for the new proposed system was beyond the scope of the study. Hence, the future research topics are summarized as follows.

1. The interference model of the wireless signal to the BPLC signal, which is presented in Chapter 3 through modeling the antenna mode current characteristic impedance will be extended to include other parameters like: transmission lines buried inside the ground, transmission lines terminated with impedance and lossy transmission lines. Also, the interference model should include the UHF band.

2. The channel measurements presented in Chapter 2 are held using the BPLC coupling circuit and the wireless antenna separately inside the labs of the University of Liverpool. The measurements will be extended by developing a new PCB board which has the two transceivers of the BPLC and the wireless channels. Also, the measurements will include different floors, buildings and the three phases of the power line cables to accommodate more practical cases. The result of these measurements will be a complete model for the MIMO BPLC TVWS channel. Also, the measurements will include the whole VHF and UHF bands.

3. The WBPLC system proposed in Chapter 6 can be extended using the channel measurements held in (1) and (2) to exploit the UHF band. Exploiting the UHF band will make the WBPLC a practical case in the UK, since the UHF band is the only band allowed for TVWS communications.

4. The practical implementation of the WBPLC communication system on a software defined radio kit and using the implemented transceiver in (2) for practical throughput measurements. The measurements should include a real case for the primary user interference and find out the corresponding throughput of the WBPLC system. Also, a measurement based comparison will be held between the WBPLC, MIMO BPLC and BPLC WiFi, which will more prove the practical feasibility of the proposed system.

Appendix A

Derivation of A General Expression for Obstructed Path Gain (OBS)

For calculating the OBS, there are two cases. First, the branch is connecting a branching node to a terminal load. Second, the branch is connecting two branching nodes. For the first case the OBS is represented by geometric series $\frac{a}{1-r}$ where $a = \Gamma_{CB} T_{BC} e^{-2\gamma l_{BC}}$ and $r = \Gamma_{CB} \Gamma_{BC} e^{-2\gamma l_{BC}}$ for the branch **BC** in Fig. 3.1. For the second case, the formula equation that represents the OBS gain of the branch connecting two branching nodes is derived. Starting from the formula representing the adjacent nodes gain A_L [29]:

$$A_L = \sum_{l=1}^{k} a_l \tag{A.1}$$

Where k is the total number of the branching nodes on the left hand side of the Tx, a_l is the effect of the multipath signal propagation resulting from branching node C_l in the l-th section and it can be obtained by [29]:

$$a_l = [\prod_{p=1}^{l-1} M_p \prod_{q=1}^{l-1} \prod_{s=1}^{n} (OBS_{q,s} + 1)] b_l \tag{A.2}$$

$$M_p = T_{C_p C_{p-1}} T_{C_{p-1} C_p} e^{-2\gamma l_{C_p C_{p-1}}} \tag{A.3}$$

$$b_l = N_l + M_l [\prod_{s=1}^{n} (OBS_{l,s} + 1) - 1] \tag{A.4}$$

$$N_l = \Gamma_{C_l C_{l-1}} T_{C_{l-1} C_l} e^{-2\gamma l_{C_l C_{l-1}}} \tag{A.5}$$

Using A.2, the summation of the two terms a_{k-1} and a_k is given by:

$$\begin{aligned} a_{k-1} + a_k = &[\prod_{p=1}^{k-2} M_p \prod_{q=1}^{k-2} \prod_{s=1}^{n} (OBS_{q,s} + 1)] b_{k-1} \\ &+ [\prod_{p=1}^{k-1} M_p \prod_{q=1}^{k-1} \prod_{s=1}^{n} (OBS_{q,s} + 1)] b_k \end{aligned} \tag{A.6}$$

Substituting in (A.6) using (A.4)

$$\begin{aligned} a_{k-1} + a_k = &[\prod_{p=1}^{k-2} M_p \prod_{q=1}^{k-2} \prod_{s=1}^{n} (OBS_{q,s} + 1)] b_{k-1} \\ \times &[N_{k-1} + M_{k-1} (\prod_{s=1}^{n} (OBS_{k-1,s} + 1)(b_k + 1) - 1)] \end{aligned} \tag{A.7}$$

This leads us to the conclusion that the b_k is the OBS value for the branch which connects both the $(k-1)$-th and the k-th branching nodes, hence the number of the branches coming out of the $(k-1)$-th node changes from n to $n+1$ and (A.7)

can be rewritten as:

$$\begin{aligned} a_{k-1} + a_k = [\prod_{p=1}^{k-2} M_p \prod_{q=1}^{k-2} \prod_{s=1}^{n} (OBS_{q,s} + 1)] b_{k-1} \\ \times [N_{k-1} + M_{k-1} (\prod_{s=1}^{n+1} (OBS_{k-1,s} + 1) - 1)] \end{aligned} \tag{A.8}$$

From (A.8), it can be deduced that $OBS_{k-1,s}$ of the s-th branch connecting $(k-1)$-th node to the k-th node is equal to b_k. However, if the k-th node is a terminal node, then the $OBS_{k-1,s}$ is equal to $\frac{a_s}{1-r_s}$ as showed in (3.3).

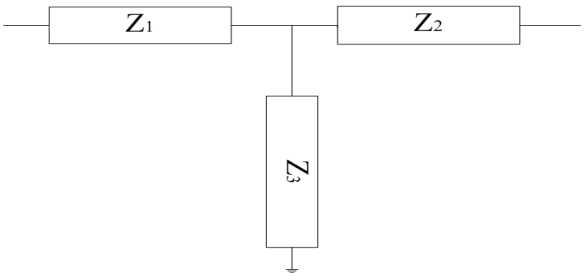

FIGURE B.1: T-network terminal impedance

Appendix B

Modelling the Antenna Mode Current Conversion to Differential Mode

The antenna mode current is converted to differential mode due to the asymmetry of the terminal loads as in [55][74][75]. As shown in Fig. B.1, a T-network is adopted to represent the impedance asymmetry at the TL terminals. Let ϕ_{a_t} and ϕ_{d_t} be the generated antenna and differential mode potentials at the terminal loads. Also, let J_{a_t} and J_{d_t} be the values of the antenna and differential mode currents transmitted to the terminal loads. The conversion between the different

modes of current propagating along the TL can be written as

$$\begin{bmatrix} \phi_{a_t} \\ \\ \phi_{d_t} \end{bmatrix} = \begin{bmatrix} Z_{a_t} & \triangle Z_t \\ \\ \triangle Z_t & Z_{d_t} \end{bmatrix} \begin{bmatrix} J_{a_t} \\ \\ J_{d_t} \end{bmatrix} \tag{B.1}$$

where Z_{a_t} and Z_{d_t} are the equivalent antenna mode and differential mode impedance at the terminal loads, respectively. The relationship between Z_{a_t}, Z_{d_t} and Z_1, Z_2, Z_3 is defined as in [74][75]. $\triangle Z_t$ is the difference between the values of the impedance seen by each transmission line to the ground. The relationship between the terminal load currents J_{a_t}, J_{d_t} and the TL currents J_a, J_d can be expressed as

$$\begin{bmatrix} J_{a_t} \\ \\ J_{d_t} \end{bmatrix} = \begin{bmatrix} T_{a_t} & 0 \\ \\ 0 & T_{d_t} \end{bmatrix} \begin{bmatrix} J_a \\ \\ J_d \end{bmatrix} \tag{B.2}$$

where T_{a_t} and T_{d_t} are the transmission coefficients of the both the antenna mode and differential mode current at the terminal loads.

Hence, the differential interference potential $\phi_{d_{t_i}}$ induced due to the antenna mode current is expressed as

$$\phi_{d_{t_i}} = \triangle Z_t T_{a_t} J_a \tag{B.3}$$

The interference power P_{t_i} can be calculated as

$$P_{t_i} = \phi_{d_{t_i}} J_{a_t} \tag{B.4}$$

Appendix C

Green's Function of Antenna Potential, Magnetic Vector Potential and Antenna current for Differential and Antenna Modes of Excitation

The current induced by an electric field incident over a wire is related to the exciting field by the electric field integral equation (EFIE) [90]. Let $\mathbf{E}_t^{ex}$ be the tangential component of the exciting electric field and let $\mathbf{J}$ be the induced current along the length of the wire, then the following can be concluded

$$\mathbf{E}_t^{ex}(\mathbf{r}) = -j\omega\mu_0 \int_l [\bar{\mathbf{I}} + \frac{1}{k_0^2} \bigtriangledown \bigtriangledown .] \frac{e^{-jk_0|\mathbf{r}-\mathbf{r}'|}}{4\pi|\mathbf{r}-\mathbf{r}'|} . \mathbf{J}(\mathbf{r}')d\mathbf{r}' \tag{C.1}$$

where $\mathbf{r}'$ and $\mathbf{r}$ are the position vectors of the source and observation points, respectively, l is the length of the wire, $\bar{\mathbf{I}}$ indicates a unit vector, k_0 is the free space wave number where $k_0 = \omega\sqrt{\epsilon_0\mu_0}$. Here, ω is the angular frequency of the exciting electric field, ϵ_0 is the free space electric permittivity and μ_0 is the free space magnetic permeability. The wire is assumed to be a perfect conductor. Hence, the total tangential electric field should be equal to zero. Also, a thin wire approximation is assumed such that the radius of the wire is too much shorter than the wavelength of the exciting electric field. Here, the electric field can be considered to be related to the induced current by the dyadic free space Green's function as

$$\mathbf{E}_t^{ex}(\mathbf{r}) = \int_l G_{EGF}(\mathbf{r}-\mathbf{r}')\mathbf{J}(\mathbf{r}')d\mathbf{r}' \tag{C.2}$$

where the electric field Green's function $G_{EGF}(\mathbf{r},\mathbf{r}')$ is expressed as

$$G_{EGF}(\mathbf{r},\mathbf{r}') = -j\omega\mu_0[\bar{\mathbf{I}} + \frac{1}{k_0^2}\bigtriangledown\bigtriangledown.]\frac{e^{-jk_0|\mathbf{r}-\mathbf{r}'|}}{4\pi|\mathbf{r}-\mathbf{r}'|} \tag{C.3}$$

The relation between the exciting electric field and the induced current can be expressed using the operator $\mathcal{L}$ as in [90]

$$\mathbf{E}_t^{ex}(\mathbf{r}) = \mathcal{L}\mathbf{J}(\mathbf{r}') \tag{C.4}$$

where $\mathcal{L}$ can be expressed as

$$\mathcal{L} = \frac{-j\omega\mu_0}{4\pi}\int_l [\bar{\mathbf{I}} + \frac{1}{k_0^2}\bigtriangledown\bigtriangledown.]G_{\mathrm{fs}}(\mathbf{r},\mathbf{r}')d\mathbf{r}' \tag{C.5}$$

Hence, the current can be expressed in the terms of the exciting field as

$$\mathbf{J}(\mathbf{r}) = \mathcal{L}^{-1}\mathbf{E}_t^{ex}(\mathbf{r}') \tag{C.6}$$

This means that the excited current can be obtained using the integration of a Green's function with the exciting electric field. The antenna current Green's function was derived in [90] using the distribution theory. It was expressed as the distribution of a series of dyadic antenna current Green's functions $\bar{\mathbf{F}}_n(\mathbf{r}, \mathbf{r}')$ over the electric field as a test function. $\bar{\mathbf{F}}_n(\mathbf{r}, \mathbf{r}')$ can be derived using the operator $\mathcal{L}_{\mathbf{r}}^{-1}$, where the subscript $\mathbf{r}$ in the operator $\mathcal{L}_{\mathbf{r}}^{-1}$ indicates that the operator $\mathcal{L}^{-1}$ is applied to vector $\mathbf{r}$. Hence, $\bar{\mathbf{F}}_n(\mathbf{r}, \mathbf{r}')$ can be expressed as

$$\bar{\mathbf{F}}_n(\mathbf{r}, \mathbf{r}') = \mathcal{L}_{\mathbf{r}}^{-1} f_n^S(\mathbf{r}, \mathbf{r}') \tag{C.7}$$

where $f_n^S(\mathbf{r}, \mathbf{r}')$ is a series of non-negative locally integrable functions along the wire. S is the two-dimensional manifold space, where $f_n^S(\mathbf{r}, \mathbf{r}')$ functions are defined. Those functions should satisfy the conditions as defined in Theorem A.1 of Appendix B in [90]. Also, if the operator $\mathcal{L}^{-1}$ is applied to vector $\mathbf{r}'$ or $\mathbf{r}''$ function the operator should be $\mathcal{L}_{\mathbf{r}'}^{-1}$ or $\mathcal{L}_{\mathbf{r}''}^{-1}$, respectively. For thin wire approximation, the series of functions $f_n^S(\mathbf{r}, \mathbf{r}')$ converges to $\delta(\mathbf{r} - \mathbf{r}')$ as $n \to \infty$. Hence, it can be shown

$$\mathcal{L}_{\mathbf{r}}^{-1}\delta(\mathbf{r} - \mathbf{r}') = \lim_{n\to\infty} \mathcal{L}_{\mathbf{r}}^{-1} f_n^S(\mathbf{r}, \mathbf{r}') \tag{C.8}$$

Hence, the current can be expressed as

$$\mathbf{J}(\mathbf{r}) = \lim_{n\to\infty} \langle \bar{\mathbf{F}}_n(\mathbf{r}, \mathbf{r}') \mathbf{E}_t^{ex}(\mathbf{r}') \rangle \tag{C.9}$$

This can be interpreted for the case of a thin wire in the integral form as

$$\mathbf{J}(\mathbf{r}) = \lim_{n\to\infty} \int_l \bar{\mathbf{F}}_n(\mathbf{r}, \mathbf{r}') \mathbf{E}_t^{ex}(\mathbf{r}') d\mathbf{r}' \tag{C.10}$$

This means that according to the distribution theory, the distribution of $\bar{\mathbf{F}}_n(\mathbf{r}, \mathbf{r}')$ over electric field can converge to

$$\mathbf{J}(\mathbf{r}) = \int_l \mathcal{L}_{\mathbf{r}}^{-1} \delta(\mathbf{r} - \mathbf{r}') \mathbf{E}_t^{ex}(\mathbf{r}') d\mathbf{r}' \tag{C.11}$$

Hence, the final expression for the antenna current Green's function G_{AC} is

$$G_{\mathrm{AC}}(\mathbf{r}, \mathbf{r}') = \mathcal{L}_{\mathbf{r}}^{-1} \delta(\mathbf{r} - \mathbf{r}') \tag{C.12}$$

There are two modes of excitation in the case of two parallel wires in free space: 1) Differential mode; 2) Antenna mode. In the differential mode, the two excited currents propagate in opposite directions, while in the antenna mode the two excited currents propagate in the same direction. For each mode there will be different Green's functions for the antenna potential, the magnetic vector potential and the antenna current. Consider the case of two perfect conducting parallel wires. Let $\mathbf{r_1}$ and $\mathbf{r_2}$ be the position vectors for the observation points located on wires, 1 and 2, respectively. Let $\mathbf{r_1'}$ and $\mathbf{r_2'}$ are the position vectors for the source

points located on wire 1 and 2, respectively. Free space Green's function $G_{\rm fs}(\mathbf{r},\mathbf{r}')$ for the differential/antenna (d/a) mode can be defined as

$$G_{\rm fs-d/a}(\mathbf{r},\mathbf{r}') = \frac{e^{-jk_0|\mathbf{r}-\mathbf{r}'_\mathbf{1}|}}{|\mathbf{r}-\mathbf{r}'_\mathbf{1}|}(\overset{-}{+})\frac{e^{-jk_0|\mathbf{r}-\mathbf{r}'_\mathbf{2}|}}{|\mathbf{r}-\mathbf{r}'_\mathbf{2}|} \tag{C.13}$$

Hence the $\mathcal{L}$ operator for the differential mode can be defined as

$$\mathcal{L}_{\rm d/a} = \frac{-j\omega\mu_0}{4\pi}\int_l [\bar{\mathbf{I}} + \frac{1}{k_0^2}\bigtriangledown\bigtriangledown.]G_{\rm fs-d/a}(\mathbf{r},\mathbf{r}')d\mathbf{r}' \tag{C.14}$$

Hence, the Green's functions can be defined for the antenna current, the antenna potential, the magnetic vector potential and the charge density for the differential or antenna mode of excitation as

$$G_{\rm AC-d/a}(\mathbf{r},\mathbf{r}') = {\mathcal{L}_{\rm d/a}}_r^{-1}\delta(\mathbf{r}-\mathbf{r}') \tag{C.15}$$

$$\begin{aligned} &G_{\rm AV-d/a}(\mathbf{r},\mathbf{r}'') = \\ &\frac{-1}{4\pi\epsilon_0 j\omega}\int_l G_{\rm fs-d/a}(\mathbf{r},\mathbf{r}')\frac{\partial}{\partial\mathbf{r}'}\mathcal{L}^{-1}_{r'-{\rm d/a}}\delta(\mathbf{r}'-\mathbf{r}'')d\mathbf{r}' \end{aligned} \tag{C.16}$$

$$\begin{aligned} &G_{\rm MV-d/a}(\mathbf{r},\mathbf{r}'') = \\ &\qquad\frac{\mu_0}{4\pi}\int_l G_{\rm fs-d/a}(\mathbf{r},\mathbf{r}')\mathcal{L}^{-1}_{r'-{\rm d/a}}\delta(\mathbf{r}'-\mathbf{r}'')d\mathbf{r}' \end{aligned} \tag{C.17}$$

$$G_{\rm CD-d/a}(\mathbf{r},\mathbf{r}') = \frac{-1}{j\omega}\frac{\partial}{\partial\mathbf{r}}\mathcal{L}^{-1}_{r-{\rm d/a}}\delta(\mathbf{r}-\mathbf{r}') \tag{C.18}$$

Appendix D

Boundary Condition Matrix Elimination

Let **Q** be a diagonal matrix which forces the boundary conditions on the excited current at the terminals of the transmission line as presented in [91]. Using the MOM numerical method to solve the integral in equation (4.8) as in [91], equation (4.8) is rewritten in the numerical form as

$$\mathbf{A}(\mathbf{r}) = \frac{\mu_0}{4\pi}\mathbf{UQJ}(\mathbf{r}) \tag{D.1}$$

where **U** represents the matrix of integrations of the free space Green's function $G_{\text{fs}}(\mathbf{r}, \mathbf{r}')$ with current basis function for different source and observation points. $\mathbf{J}(\mathbf{r})$ is a vector which represents the excited current value at different source points. $\mathbf{J}(\mathbf{r})$ represents the current component which is independent of the boundary conditions, while the effect of the forward and reflected current components are represented in the **Q** diagonal matrix. It is worth mentioning that both **U** and

$\mathbf{Q}$ are symmetric matrices such that $\mathbf{U^T} = \mathbf{U}$ and $\mathbf{Q^T} = \mathbf{Q}$. Equation (4.13) can be rewritten in the numerical form as

$$L_{\mathrm{d/a}}(\mathbf{r}) = \frac{\frac{\mu_0}{4\pi}\mathbf{UQJ}(\mathbf{r})}{\mathbf{QJ}(\mathbf{r})} \tag{D.2}$$

Using the symmetry property of $\mathbf{U}$ and $\mathbf{Q}$, equation (D.2) can be rewritten as

$$L_{\mathrm{d/a}}(\mathbf{r}) = \frac{\frac{\mu_0}{4\pi}\mathbf{QUJ}(\mathbf{r})}{\mathbf{QJ}(\mathbf{r})} \tag{D.3}$$

The boundary condition matrix can be removed from both numerator and denominator, since $\mathbf{Q}$ matrix is a diagonal matrix. Hence, the above equation is written as

$$L_{\mathrm{d/a}}(\mathbf{r}) = \frac{\frac{\mu_0}{4\pi}\mathbf{UJ}(\mathbf{r})}{\mathbf{J}(\mathbf{r})} \tag{D.4}$$

Following the same principle, the boundary condition matrix can be removed from the numerical form of equation (4.11) for the capacity p.u.l..

Appendix E

Derivation of the ETLA Solution of the Antenna Mode Characteristic Impedance Mean Value

The exciting electric field $\mathbf{E}_t^{ex}(\mathbf{r})$ can be expressed in the terms of the potential $\phi(\mathbf{r})$ and the magnetic vector potential $\mathbf{A}(\mathbf{r})$ as

$$\mathbf{E}_t^{ex}(\mathbf{r}) = -j\omega\mathbf{A}(\mathbf{r}) - \nabla\phi(\mathbf{r}) \tag{E.1}$$

Using both (4.4) and (E.1) the general Telegrapher equations for the current induced along two parallel wires in free space by the effect of incident electric field

are expressed as

$$\frac{\partial \phi_a(\mathbf{r})}{\partial \mathbf{r}} + \frac{j\omega\mu_0}{4\pi}\int_l G_{\text{fs}-a}(\mathbf{r},\mathbf{r}')\mathbf{J}_a(\mathbf{r}')d\mathbf{r}' = \mathbf{E}^{ex}_{t-a}(\mathbf{r}) \tag{E.2}$$

$$\phi_a(\mathbf{r}) = -\frac{1}{j\omega 4\pi\epsilon_0}\frac{\partial}{\partial \mathbf{r}}\int_l G_{\text{fs}-a}(\mathbf{r},\mathbf{r}')\mathbf{J}_a(\mathbf{r}')d\mathbf{r}' \tag{E.3}$$

where $\phi_a(\mathbf{r})$ and $\mathbf{J}_a(\mathbf{r})$ are the excited antenna mode potential and current, respectively.

In case $l < \lambda$ (where λ represents the wavelength), the current can be considered as constant along the integral and apply the approximation used in [45]. However, if $l > \lambda$, the approximation made in [45] becomes invalid and a better approximation should be found. Here the current can be assumed to have two separate components $\mathbf{J}_o(\mathbf{r})$ and $e^{-jk_1\mathbf{r}}$

$$\mathbf{J}_a(\mathbf{r}) = \mathbf{J}_o(\mathbf{r})e^{-jk_1\mathbf{r}} \tag{E.4}$$

where the rate of change of $\mathbf{J}_o(\mathbf{r})$ with the position vector $\mathbf{r}$ is much less than the decay rate of the free space Green's function $G_{\text{fs}-a}(\mathbf{r},\mathbf{r}')$, so it can be considered as constant over the integral. Also $k_1 = k_o cos(\theta)$ where k_o is the wave number in free space and θ is the incident angle. The integral in equations (E.2) and (E.3) can be rewritten as

$$\begin{aligned}&\int_l G_{\text{fs}-a}(\mathbf{r},\mathbf{r}')\mathbf{J}_a(\mathbf{r}')d\mathbf{r}' = \\ &\mathbf{J}_o(\mathbf{r})\int_l \frac{e^{-jk_0|\mathbf{r}-\mathbf{r}'_\mathbf{1}|}}{|\mathbf{r}-\mathbf{r}'_\mathbf{1}|} + \frac{e^{-jk_0|\mathbf{r}-\mathbf{r}'_\mathbf{2}|}}{|\mathbf{r}-\mathbf{r}'_\mathbf{2}|}e^{-jk_1\mathbf{r}'}d\mathbf{r}'\end{aligned} \tag{E.5}$$

Assume that the two wires are along the z-axis. Thus (E.5) reduces to

$$\begin{aligned}&\int_l G_{\text{fs}-a}(\mathbf{z},\mathbf{z}')\mathbf{J}(\mathbf{z}')d\mathbf{z}' = \\ &\mathbf{J}_o(\mathbf{z})\int_l \left[\frac{e^{-jk_0\sqrt{(\mathbf{z}-\mathbf{z}')^2+a^2}}}{\sqrt{(\mathbf{z}-\mathbf{z}')^2+a^2}} + \frac{e^{-jk_0\sqrt{(\mathbf{z}-\mathbf{z}')^2+d^2}}}{\sqrt{(\mathbf{z}-\mathbf{z}')^2+d^2}}\right] e^{-jk_1\mathbf{z}'}d\mathbf{z}'\end{aligned} \tag{E.6}$$

where a is the wire radius and d is the distance between the two wires. Substitute $\mathbf{u} = \mathbf{z}' - \mathbf{z}$ into (E.6)

$$\begin{aligned}&\int_l G_{\text{fs}-a}(\mathbf{z},\mathbf{z}')\mathbf{J}(\mathbf{z}')d\mathbf{z}' = \\ &\mathbf{J}_o(\mathbf{z})e^{-jk_1\mathbf{z}}\int_{-z}^{l-z} \left[\frac{e^{-jk_0\sqrt{\mathbf{u}^2+a^2}}}{\sqrt{\mathbf{u}^2+a^2}} + \frac{e^{-jk_0\sqrt{\mathbf{u}^2+d^2}}}{\sqrt{\mathbf{u}^2+d^2}}\right] e^{-jk_1\mathbf{u}}d\mathbf{u}\end{aligned} \tag{E.7}$$

the following two known integrals can be used

$$\int_{-\infty}^{\infty} \frac{e^{-jk_0\sqrt{u^2+a^2}}}{\sqrt{u^2+a^2}} e^{-jk_1 u} = -j\pi H_0^{(2)}(a\sqrt{k_0^2-k_1^2}) \tag{E.8}$$

and

$$E_1(z) = \int_z^{\infty} \frac{e^{-t}}{t}dt \tag{E.9}$$

Using (E.8) and (E.9) to solve the integral in (E.7), it can be concluded

$$\int_l G_{\text{fs}-a}(\mathbf{r},\mathbf{r}')\mathbf{J}(\mathbf{r}')d\mathbf{r}' = \mathbf{J}(\mathbf{r})\Psi(\mathbf{r}) \tag{E.10}$$

where $\Psi(\mathbf{r})$ is given by (4.16).

a 0.9 fitting factor is added to the approximated analytical solution in (4.16), since a difference is observed between the approximated solution and the numerical

solution of the integral in (E.7). This difference comes from the adopted approximation that the area covered by the integral in (E.7) is equal to the difference between the areas covered by integrals in (E.8) and (E.9). Substituting (4.16) into (E.2) and (E.3), the inductance and capacitance p.u.l. can be obtained in (4.17) and (4.18), respectively, and the characteristic impedance in (4.19).

Appendix F

Proof of Lemma 1 in Chapter 5

Let $\alpha_{i,k}^{(n)}$ be the i-th component of the interference vector α_k. In order to satisfy the interference power limit at the TV PU Rx, while maintaining good SNR at the Rx

$$\Sigma_{i=1}^{n_r} \alpha_{i,k}^{(n)} P_{i,k}^{(n)} \leq \Gamma, \quad \mathbf{\Lambda}^{(n)} \mathbf{P}_1^{(n)} \succeq \sigma_n^2 + \sigma_p^2 \tag{F.1}$$

Let $\Gamma \leq \sigma_n^2$ to avoid harmful interference. Also let $\sigma_n^2 + \sigma_p^2 = \rho\Gamma$. Hence, the following equation can be concluded

$$\mathbf{\Lambda}^{(n)} \mathbf{P}_1^{(n)} \succeq \rho \alpha_k^{(n)} \mathbf{P}_1^{(n)} \tag{F.2}$$

This can be translated in the following matrix form

$$\begin{bmatrix} \frac{\lambda_1^{(n)}}{\rho} - \alpha_{1,k}^{(n)} & \dots & -\alpha_{n_r,k}^{(n)} \\ \vdots & & \vdots \\ -\alpha_{1,k}^{(n)} & \dots & \frac{\lambda_{n_r}^{(n)}}{\rho} - \alpha_{n_r,k}^{(n)} \end{bmatrix} \begin{bmatrix} P_1^{(n)} \\ \vdots \\ P_{n_r}^{(n)} \end{bmatrix} \succeq 0 \tag{F.3}$$

Directly, the condition in (5.7) can be concluded.

Appendix G

Proof of Lemma 2 in Chapter 5

Using the OR decision rule for MIMO channel, it can be deduced

$$\hat{\mathcal{P}}_d = 1 - \Pi_{i=1}^{n_r}(1 - \mathcal{P}_{d_i}) \tag{G.1}$$

where $\mathcal{P}_{d_i}$ can be expressed as follows for the energy detection method [85]

$$\mathcal{P}_{d_i} = Q\Big((\frac{\epsilon}{\sigma_n^2} - \gamma_i - 1)\Big(\sqrt{\frac{\tau_i f_s}{2\gamma_i + 1}}\Big)\Big) \tag{G.2}$$

where ϵ is the detection threshold. N_{min} is assumed to be equal for all the MIMO sub-channels. Hence, relationship between the detection probabilities of two MIMO sub-channels i and m can be expressed as follows using (5.9)

$$\mathcal{P}_{d_i} = Q\Big(\frac{\gamma_m - \gamma_i}{\gamma_m\sqrt{2\gamma_i + 1}}Q^{-1}(\hat{\mathcal{P}}_{fa}) + Q^{-1}(\mathcal{P}_{d_m})\sqrt{\frac{2\gamma_m + 1}{2\gamma_i + 1}}\Big) \tag{G.3}$$

Substituting (G.3) into (G.1), Lemma 2 can directly be concluded.

Appendix H

Lagrangian Problem Solution in Chapter 6

Using the primal decomposition method, the problem in (6.9) can be subdivided into 3 convex optimization sub-problems as

Sub-Problem 1

$$
\begin{aligned}
L_1 =&(1-P_e) \\
&\sum_{j=1}^{K}\sum_{n_A=1}^{N_1}\frac{1+\beta_j}{t_1}\log_2\left\{1+\frac{1.6P_{n_Aj}C_{n_Aj}}{N_0\left[(0.2/P_e)^{\frac{1}{N_{t_A}N_{r_A}}}-1\right]}\right\}- \\
&\lambda\sum_{j=1}^{K}\sum_{n_A=1}^{N_1}P_{n_Aj}-\sum_{n_A=1}^{N_1}\mu_{n_A}\left[\sum_{j=1}^{K}P_{n_Aj}-P_A\right]
\end{aligned}
\tag{H.1}
$$

Sub-Problem 2

$$L_2 = (1-P_e) \sum_{j=1}^{K}\sum_{n_B=1}^{N_2} \frac{PH_0(1+\beta_j)}{t_2}\log_2\left\{1+\frac{1.6P_{n_Bj}^{(0)}C_{n_Bj}^{(0)}}{(2N_0\big[(\frac{0.2}{P_e})^{\frac{1}{N_{t_B}^{(0)}N_{r_B}^{(0)}}}-1\big])}\right\}- \lambda\sum_{j=1}^{K}\sum_{n_B=1}^{N_2} PH_0P_{n_Bj}^{(0)} - \sum_{n_B=1}^{N_2}\mu_{n_B}^{(0)}\big[\sum_{j=1}^{K}P_{n_Bj}^{(0)} - P_B^{(0)}\big] \tag{H.2}$$

Sub-Problem 3

$$L_3 = (1-P_e) \sum_{j=1}^{K}\sum_{n_B=1}^{N_2} \frac{PH_1(1+\beta_j)}{t_2}\log_2\left\{1+\frac{1.6P_{n_Bj}^{(1)}C_{n_Bj}^{(1)}}{(2N_0\big[(\frac{0.2}{P_e})^{\frac{1}{(N_{t_B}^{(1)}N_{r_B}^{(1)})}}-1\big])}\right\}- \lambda\sum_{j=1}^{K}\sum_{n_B=1}^{N_2} PH_1P_{n_Bj}^{(1)} - \sum_{n_B=1}^{N_2}\mu_{n_B}^{(1)}\big[\sum_{j=1}^{K}P_{n_Bj}^{(1)} - P_B^{(1)}\big] \tag{H.3}$$

After forming the Lagrangian functions and applying the KKT conditions, the optimal powers can be given by 5.5-F.1.

Bibliography

[1] H. Wang, Y. Qian, and H. Sharif, "Multimedia communications over cognitive radio networks for smart grid applications," *IEEE Wireless Communications*, vol. 20, no. 4, pp. 125–132, August 2013.

[2] K. Patil, R. Prasad, and K. Skouby, "A survey of worldwide spectrum occupancy measurement campaigns for cognitive radio," in *Proc. International Conference on Devices and Communications (ICDeCom)*, pp. 1–5, February 2011, Mesra, India.

[3] S. Contreras, G. Villardi, R. Funada, and H. Harada, "An investigation into the spectrum occupancy in Japan in the context of TV White Space systems," in *6th International ICST Conference on Cognitive Radio Oriented Wireless Networks and Communications (CROWNCOM)*, pp. 341–345, June 2011, Osaka, Japan.

[4] A. Marţian, C. Vlădeanu, I. Marcu, and I. Marghescu, "Evaluation of Spectrum Occupancy in an Urban Environment in a Cognitive Radio Context," *International Journal on Advances in Telecommunications*, vol. 3, no. 3, pp. 172–181, 2010.

[5] M. Hoyhtya, A. Mammela, M. Eskola, M. Matinmikko, J. Kalliovaara, J. Ojaniemi, J. Suutala, R. Ekman, R. Bacchus, and D. Roberson, "Spectrum occupancy measurements: A survey and use of interference maps," *IEEE Communications Surveys and Tutorials*, vol. PP, no. 99, pp. 1–30, April 2016.

[6] M. H. Islam, C. L. Koh, S. W. Oh, X. Qing, Y. Y. Lai, C. Wang, Y.-C. Liang, B. E. Toh, F. Chin, G. L. Tan *et al.*, "Spectrum survey in Singapore: Occupancy measurements and analyses," in *3rd International Conference on Cognitive Radio Oriented Wireless Networks and Communications (CrownCom 2008)*, pp. 1–7, May 2008, Singapore.

[7] M. Fadda, M. Murroni, and V. Popescu, "A cognitive radio indoor hdtv multi-vision system in the tv white spaces," *IEEE Transactions on Consumer Electronics*, vol. 58, no. 2, pp. 302–310, May 2012.

[8] "Notice of proposed rule making," *Federal Communications Commision, Document 04–113*, May 2004.

[9] "Second Report and Order and Memorandum Opinion and Order In the Matter of Unlicensed Operation in the TV Broadcast Bands, Additional Spectrum for Unlicensed Devices Below 900 MHz and in the 3 GHz Band," *Federal Communication Commision, Document 08-260*, November 2008.

[10] "IEEE 802.11 af Draft 5.0, Amendment 5: TV White Spaces Operation," Retrieved April 2013.

[11] "MAC and PHY for Operation in TV White Space," *ECMA-392*, December 2009.

[12] M. U. Rehman, S. Wang, Y. Liu, S. Chen, X. Chen, and C. G. Parini, "Achieving high data rate in multiband-OFDM UWB over power-line communication system," *IEEE Transactions on Power Delivery*, vol. 27, no. 3, pp. 1172–1177, July 2012.

[13] L. B. Wang, P. L. So, K. Y. See, M. Oswal, and T. S. Pang, "Investigation of radiated emissions in power line communication networks," in *Proc. IEEE International Power Engineering Conference (IPEC 2007)*, pp. 455–460, December 2007, Singapore.

[14] S. Khedimallah, B. Nekhoul, K. Kerroum, and K. El Khamlichi Drissi, "Analysis of power line communications electromagnetic field in electrical networks taking into account the power transformers," in *Proc. IEEE International Symposium on Electromagnetic Compatibility*, pp. 1–6, Sep. 2012, Rome, Italy.

[15] V. Doric, D. Poljak, I. Hadjina, and K. El Khamlichi Drissi, "EMC analysis of the narrowband PLC system based on the antenna theory," in *Proc. IEEE 21st Int. Conf. Soft., Telecomm. Comput. Networks (SoftCOM)*, pp. 1–5, September 2013, Primosten, Croatia.

[16] I. S. Association *et al.*, "IEEE Standard for Broadband over Power Line Networks: Medium Access Control and Physical Layer Specifications," *IEEE Std 1901*, vol. 2010, pp. 1–1586, 2010.

[17] L. T. Berger, A. Schwager, P. Pagani, and D. Schneider, *MIMO Power Line Communications: Narrow and Broadband Standards, EMC, and Advanced Processing*. CRC Press, 2014.

[18] S. W. Lai, N. Shabehpour, G. G. Messier, and L. Lampe, "Performance of wireless/power line media diversity in the office environment," in *Proc. IEEE Global Communications Conference (GLOBECOM)*, pp. 2972–2976, December 2014, Texas, USA.

[19] E. Tsakalaki, O. Alrabadi, E. De Carvalho, and G. F. Pedersen, "Antenna design considerations for mimo tv white-space handsets," in *7th European Conference on Antennas and Propagation (EuCAP)*, pp. 2597–2600, April 2013, Gothenburg, Sweden.

[20] M. Nekovee, "Cognitive radio access to tv white spaces: Spectrum opportunities, commercial applications and remaining technology challenges," in *IEEE Symposium on New Frontiers in Dynamic Spectrum*, pp. 1–10, April 2010, Singapore.

[21] J. Oh, S. Kim, and B. Jeong, "Mimo/multi-channel rf transceiver for cognitive radio system," in *Proc. IEEE MTT-S International Microwave Workshop Series on Intelligent Radio for Future Personal Terminals (IMWS-IRFPT)*, pp. 1–4, September 2011, Daejeon, South Korea.

[22] J. Andrusenko, R. L. Miller, J. A. Abrahamson, N. M. Merheb Emanuelli, R. S. Pattay, and R. M. Shuford, "VHF general urban path loss model for

short range ground-to-ground communications," *IEEE Transactions on Antennas and Propagation*, vol. 56, no. 10, pp. 3302–3310, October 2008.

[23] Z. Lin, M. Ghosh, and A. Demir, "A comparison of mac aggregation vs. phy bonding for wlans in tv white spaces," in *IEEE 24th International Symposium on Personal Indoor and Mobile Radio Communications (PIMRC)*, 1829–1834, September 2013, London, UK.

[24] J. Andrusenko, R. L. Miller, J. A. Abrahamson, N. M. Merheb Emanuelli, R. S. Pattay, and R. M. Shuford, "Vhf general urban path loss model for short range ground-to-ground communications," *IEEE Transactions on Antennas and Propagation*, vol. 56, no. 10, pp. 3302–3310, October 2008.

[25] T. Zheng, X. Yang, and B. Zhang, "Broadband transmission characteristics for power-line channels," *IEEE Transactions on Power Delivery*, vol. 21, no. 4, pp. 1905–1911, October 2006.

[26] M. Tlich, A. Zeddam, F. Moulin, and F. Gauthier, "Indoor power-line communications channel characterization up to 100 MHz part I: one-parameter deterministic model," *IEEE Transactions on Power Delivery*, vol. 23, no. 3, pp. 1392–1401, July 2008.

[27] ——, "Indoor power-line communications channel characterization up to 100 MHz part II: time-frequency analysis," *IEEE Transactions on Power Delivery*, vol. 23, no. 3, pp. 1402–1409, July 2008.

[28] A. M. Tonello and F. Versolatto, "Bottom-up statistical plc channel modeling part i: Random topology model and efficient transfer function computation," *IEEE Transactions on Power Delivery*, vol. 26, no. 2, pp. 891–898, April 2011.

[29] J. Shin, J. Lee, and J. Jeong, "Channel modeling for indoor broadband power-line communications networks with arbitrary topologies by taking adjacent nodes into account," *IEEE Transactions on Power Delivery*, vol. 26, no. 3, pp. 1432–1439, July 2011.

[30] M. Zimmermann and K. Dostert, "A multipath model for the powerline channel," *IEEE Transactions on Communications*, vol. 50, no. 4, pp. 553–559, April 2002.

[31] F. Versolatto and A. M. Tonello, "On the relation between geometrical distance and channel statistics in in-home plc networks," in *Proc. 16th IEEE International Symposium on Power Line Communications and Its Applications (ISPLC)*, pp. 280-285, March 2012, Beijing China.

[32] H. Mustafa, S. Ashutosh, S. Karamchandani, S. Merchant, and U. Desai, "Non-invasive, reflection coefficient based channel estimation on plc systems," in *Proc. 8th International Conference on Information Communications and Signal Processing (ICICS)*, pp. 1-5, December 2011, Singapore.

[33] M. Karduri, M. D. Cox, and N. J. Champagne, "Near-field coupling between broadband over power line (BPL) and high-frequency communication systems," *IEEE Transactions on Power Delivery*, vol. 21, no. 4, pp. 1885–1891, October 2006.

[34] S. V. Tkachenko, R. Rambousky, and J. B. Nitsch, "Electromagnetic field coupling to a thin wire located symmetrically inside a rectangular enclosure," *IEEE Transactions on Electromagnetic Compatibility*, vol. 55, no. 2, pp. 334–341, April 2013.

[35] F. Rachidi, "A review of field-to-transmission line coupling models with special emphasis to lightning-induced voltages on overhead lines," *IEEE Transactions on Electromagnetic Compatibility*, vol. 54, no. 4, pp. 898–911, August 2012.

[36] C. A. Nucci, F. Rachidi, and M. Rubinstein, "Interaction of lightning-generated electromagnetic fields with overhead and underground cables," *The Lightning Electromagnetics*, pp. 687–718, January 2012.

[37] A. Piantini and J. M. Janiszewski, "Lightning-induced voltages on overhead linesApplication of the extended rusck model," *IEEE Transactions on Electromagnetic Compatibility*, vol. 51, no. 3, pp. 548–558, August 2009.

[38] F. M. Tesche and T. Karlsson, *EMC Analysis Methods and Computational Models*, New York, USA:John Wiley & Sons, 1997.

[39] M. Ianoz, "Review of new developments in the modeling of lightning electromagnetic effects on overhead lines and buried cables," *IEEE Transactions on Electromagnetic Compatibility*, vol. 49, no. 2, pp. 224–236, May 2007.

[40] G. E. Bridges, "Transient plane wave coupling to bare and insulated cables buried in a lossy half-space," *IEEE Transactions on Electromagnetic Compatibility*, vol. 37, no. 1, pp. 62–70, February 1995.

[41] E. Petrache, F. Rachidi, M. Paolone, C. A. Nucci, V. A. Rakov, and M. A. Uman, "Lightning induced disturbances in buried cables-part I: theory," *IEEE Transactions on Electromagnetic Compatibility*, vol. 47, no. 3, pp. 498–508, August 2005.

[42] M. Paolone, E. Petrache, F. Rachidi, C. Nucci, V. Rakov, M. Uman, D. Jordan, K. Rambo, J. Jerauld, M. Nyffeler *et al.*, "Lightning induced disturbances in buried cables-part II: experiment and model validation," *IEEE Transactions on Electromagnetic Compatibility*, vol. 47, no. 3, pp. 509–520, August 2005.

[43] C. R. Paul, "A comparison of the contributions of common-mode and differential-mode currents in radiated emissions," *IEEE Transactions on Electromagnetic Compatibility*, vol. 31, no. 2, pp. 189–193, May 1989.

[44] D. Poljak, A. Shoory, F. Rachidi, S. Antonijevic, and S. V. Tkachenko, "Time-Domain generalized telegrapher's equations for the electromagnetic field coupling to finite length wires above a lossy ground," *IEEE Transactions on Electromagnetic Compatibility*, vol. 54, no. 1, pp. 218–224, Feb. 2012.

[45] A. Vukicevic, F. Rachidi, M. Rubinstein, and S. V. Tkachenko, "On the evaluation of antenna-mode currents along transmission lines," *IEEE Transactions on Electromagnetic Compatibility*, vol. 48, no. 4, pp. 693–700, November 2006.

[46] A. Maffucci, G. Miano, and F. Villone, "An enhanced transmission line model for conducting wires," *IEEE Transactions on Electromagnetic Compatibility*, vol. 46, no. 4, pp. 512–528, November 2004.

[47] S. Chabane, P. Besnier, and M. Klingler, "Enhanced transmission line theory: Frequency-dependent line parameters and their insertion in a classical transmission line equation solver," in *Proc. IEEE International Symposium on Electromagnetic Compatibility*, pp. 326–331, Auust. 2013, Denver, USA.

[48] F. Rachidi and S. Tkachenko, *Electromagnetic Field Interaction with Transmission Lines: From Classical Theory to HF Radiation Effects.* Southampton UK: WIT Press, 2008, vol. 5.

[49] D. Poljak, F. Rachidi, and S. V. Tkachenko, "Generalized form of telegrapher's equations for the electromagnetic field coupling to finite-length lines above a lossy ground," *IEEE Transactions on Electromagnetic Compatibility*, vol. 49, no. 3, pp. 689–697, August 2007.

[50] W. A. Finamore, M. V. Ribeiro, and L. Lampe, "Advancing power line communication: cognitive, cooperative, and mimo communication," in *Proc. Brazilian Telecommunications Symposium*, pp. 13–16, September 2012, Brasilia Brazil.

[51] P. Degauque, P. Laly, V. Degardin, M. Lienard, and L. Diquelou, "Compromising Electromagnetic Field Radiated by In-House PLC Lines," in *Proc. IEEE Global Telecommunications Conference (GLOBECOM).* pp. 1–5: IEEE, December 2010, Florida USA.

[52] V. Degardin, P. Laly, M. Lienard, and P. Degauque, "Compromising Radiated Emission from a Power Line Communication Cable," *Journal of Communications Software & Systems*, vol. 7, no. 1, pp. 16–21, March 2011.

[53] P. Degauque, P. Laly, V. Degardin, and M. Lienard, "Power line communication and compromising radiated emission," in *Proc. IEEE International Conference on Software, Telecommunications and Computer Networks (SoftCOM)*. 88–91: IEEE, September 2010, Split - Bol Croatia.

[54] T. R. Oliveira, C. A. Marques, M. S. Pereira, S. L. Netto, and M. V. Ribeiro, "The characterization of hybrid PLC-wireless channels: A preliminary analysis," in *Proc. 17th IEEE International Symposium on Power Line Communications and Its Applications (ISPLC)*. pp. 98–102: IEEE, March 2013, Johannesburg South Africa.

[55] K. L. Kaiser, *Electromagnetic Compatibility Handbook*, CRC press, 2005.

[56] J. Nitsch and S. Tkachenko, "High-frequency multiconductor transmission-line theory," *Foundations of Physics*, vol. 40, no. 9-10, pp. 1231–1252, 2010.

[57] N. Weling, "Snr-based detection of broadcast radio stations on powerlines as mitigation method toward a cognitive plc solution," in *Proc. 16th IEEE International Symposium on Power Line Communications and Its Applications (ISPLC)*. pp. 52–59: IEEE, March 2012, Beijing China.

[58] R. Vuohtoniemi, J.-P. Makela, J. Vartiainen, and J. Iinatti, "Detection of broadcast signals in cognitive radio based PLC using the FCME algorithm," in *Proc. IEEE International Symposium on Power Line Communications and its Applications (ISPLC)*, pp. 70–74, March 2014, Glasgow Scotland.

[59] B. Praho, M. Tlich, P. Pagani, A. Zeddam, and F. Nouvel, "Cognitive detection method of radio frequencies on power line networks," in *Proc. IEEE*

International Symposium on Power Line Communications and Its Applications (ISPLC), pp. 225–230, March 2010, Rio de Janeiro Brazil.

[60] K. M. Ali, G. G. Messier, and S. W. Lai, "DSL and PLC co-existence: An interference cancellation approach," *IEEE Transactions on Communications*, vol. 62, no. 9, pp. 3336–3350, September 2014.

[61] S. W. Oh, Y. L. Chiu, K. N. Ng, R. Mo, Y. Ma, Y. Zeng, and A. Syed Naveen, "Cognitive power line communication system for multiple channel access," in *Proc. IEEE International Symposium on Power Line Communications and Its Applications*, pp. 47–52, March 2009, Dresden Germany.

[62] J. Maes, M. Timmers, and M. Guenach, "Spectral compatibility of in-home and access technologies," in *Proc. IEEE International Symposium on Power Line Communications and Its Applications (ISPLC)*, pp. 7–11, April 2011, Udine Italy.

[63] B. O'hara and A. Petrick, *IEEE 802.11 handbook: a designer's companion.* IEEE Standards Association, 2005.

[64] A. H. Ali, M. A. Razak, M. Hidayab, S. A. Azman, M. Z. M. Jasmin, and M. A. Zainol, "Investigation of indoor WIFI radio signal propagation," in *Proc. IEEE Symposium on Industrial Electronics & Applications (ISIEA) 2010*, pp. 117–119, October 2010, Penang Malaysia.

[65] G. Marrocco, D. Statovci, and S. Trautmann, "A plc broadband channel simulator for indoor communications," in *Proc. 17th IEEE International Symposium on Power Line Communications and Its Applications (ISPLC)*, pp. 321-326, March 2013, Johannesburg, South Africa.

[66] S. Chen, *Ultra wideband gigabit powerline communication*, Ph.D. Dissertation, 2009.

[67] M. Heggo, X. Zhu, Y. Huang, and S. Sun, "A novel statistical approach of path loss mapping for indoor broadband power line communications," in *Proc. IEEE International Conference on Smart Grid Communications (SmartGridComm) 2014*, pp. 499–504, November 2014, Venice Italy.

[68] Z. Tao, Y. Xiaoxian, and Z. Baohui, "Broadband transmission characteristics for power-line channels," *IEEE Transactions on Power Delivery*, vol. 21, no. 4, pp. 1905–1911, October 2006.

[69] N. Benvenuto and L. Tomba, "Performance comparison of space diversity and equalization techniques for indoor radio systems," *IEEE Transactions on Vehicular Technology*, vol. 46, no. 2, pp. 358–368, May 1997.

[70] J. Yin, X. Zhu, and Y. Huang, "Modeling of amplitude-correlated and occurrence-dependent impulsive noise for power line communication," in *Proc. IEEE International Conference on Communications (ICC)*, pp. 4565–4570, June 2014, Sydney Australia.

[71] S. Wang and F. C. Lee, "Investigation of the transformation between differential-mode and common-mode noises in an EMI filter due to unbalance," *IEEE Transactions on Electromagnetic Compatibility*, vol. 52, no. 3, pp. 578–587, 2010.

[72] C. R. Paul, *Analysis of Multiconductor Transmission Lines.* John Wiley & Sons, 2008.

[73] R. Rambousky, J. Nitsch, and H. Garbe, "Matching the termination of radiating non-uniform transmission-lines," *Advances in Radio Science*, vol. 11, no. 16, pp. 259–264, July 2013.

[74] Y. Oguri, K. Murano, F. Xiao, and Y. Kami, "LCL characteristics of parallel transmission line with load circuit," in *Proc. International Symposium on Electromagnetic Compatibility*, pp. 126–129, October 2007, Qingdao, China.

[75] F. Grassi, X. Wu, Y. Yang, G. Spadacini, and S. A. Pignari, "Modeling of imbalance in differential lines targeted to spice simulation," *Progress In Electromagnetics Research B*, vol. 62, pp. 225–239, March 2015.

[76] A. Jovicic and P. Viswanath, "Cognitive radio: An information-theoretic perspective," *IEEE Transactions on Information Theory*, vol. 55, no. 9, pp. 3945–3958, September 2009.

[77] T. Yoo and A. Goldsmith, "Capacity and power allocation for fading mimo channels with channel estimation error," *IEEE Transactions on Information Theory*, vol. 52, no. 5, pp. 2203–2214, May 2006.

[78] S. J. Grant and J. K. Cavers, "Performance enhancement through joint detection of cochannel signals using diversity arrays," *IEEE Transactions on Communications*, vol. 46, no. 8, pp. 1038–1049, August 1998.

[79] X. Zhu and R. D. Murch, "Performance analysis of maximum likelihood detection in a mimo antenna system," *IEEE Transactions on Communications*, vol. 50, no. 2, pp. 187–191, February 2002.

[80] R. H. Etkin and D. N. Tse, "Degrees of freedom in some underspread mimo fading channels," *IEEE Transactions on Information Theory*, vol. 52, no. 4, pp. 1576–1608, April 2006.

[81] J. Davies, *Newnes Radio Engineer's Pocket Book*. Elsevier, 2014.

[82] P. Wongsakulphasatch, C. Phongcharoenpanich, and S. Kawdungta, "Compact flat monopole antenna for small aircraft of vhf communication system," in *Proc. IEEE Asia-Pacific Conference on Antennas and Propagation (APCAP)*, pp. 27–28, August 2012, Kaohsiung, Taiwan.

[83] H.-K. Ryu, G. Jung, and J.-M. Woo, "A small quarter wavelength microstrip antenna for hf and vhf band applications," in *Proc. 10th Mediterranean Microwave Symposium*, pp. 48–51, August 2010, Guzelyurt, Turkey.

[84] R. Zhang and Y.-C. Liang, "Exploiting multi-antennas for opportunistic spectrum sharing in cognitive radio networks," *IEEE Journal of Selected Topics in Signal Processing*, vol. 2, no. 1, pp. 88–102, February 2008.

[85] Y.-C. Liang, Y. Zeng, E. C. Peh, and A. T. Hoang, "Sensing-throughput tradeoff for cognitive radio networks," *IEEE Transactions on Wireless Communications*, vol. 7, no. 4, pp. 1326–1337, April 2008.

[86] S. Stotas and A. Nallanathan, "Enhancing the capacity of spectrum sharing cognitive radio networks," *IEEE Transactions on Vehicular Technology*, vol. 60, no. 8, pp. 3768–3779, October 2011.

[87] H. C. Ferreira, L. Lampe, J. Newbury, T. Swart, and Editors, *Power Line Communications: Theory and Applications for Narrowband and Broadband Communications over Power Lines*. John Wiley & Sons, Inc., 2010.

[88] L. Xian and H. Liu, "An adaptive power allocation scheme for space-time block coded MIMO systems," in *Proc. IEEE Wireless Communications and Networking Conference*, 504–508, March 2005, New Orleans, USA.

[89] D. Wang, H. Minn, and N. Al-Dhahir, "A robust asynchronous multiuser STBC-OFDM transmission scheme for frequency-selective channels," *IEEE Transactions on Wireless Communications*, vol. 7, no. 10, pp. 3725–3731, October 2008.

[90] S. Mikki and Y. Antar, "The antenna current greens function formalism: part I," *IEEE Transactions on Antenna Propagation*, vol. 61, no. 9, pp. 4493–4504, Sep. 2013.

[91] S. J. Orfanidis, *Electromagnetic Waves and Antennas*. Rutgers University New Brunswick, NJ, 2002.